

# Signatures of SUSY Dark Matter at the LHC and in the Spectra of Cosmic Rays

Von der Fakultät für Mathematik, Informatik und Naturwissenschaften  
der Rheinisch-Westfälischen Technischen Hochschule Aachen  
zur Erlangung des akademischen Grades eines Doktors der Naturwissenschaften  
genehmigte Dissertation

vorgelegt von

Diplom-Physiker  
Jan Olzem

aus Krefeld

Berichter: Universitätsprofessor Dr. St. Schael  
Universitätsprofessorin Dr. L. Baudis

Tag der mündlichen Prüfung: 27. Februar 2007

Diese Dissertation ist auf den Internetseiten der Hochschulbibliothek online verfügbar.



# Abstract

Over the past decades it has become evident that luminous matter amounts only to a small fraction of the energy density in the universe. More than 75 % is accounted for by what is called the dark energy, and about 20 % must exist in the form of some kind of non-relativistic dark matter. Among the candidates for the constituents of dark matter, the supersymmetric (SUSY) neutralino is one of the most promising. This thesis discusses the search for supersymmetry at the future Large Hadron Collider (LHC) and the ongoing construction of one of the four large LHC experiments, the Compact Muon Solenoid (CMS), and focuses on the detection of signals from the annihilation of supersymmetric dark matter in the spectra of cosmic rays.

CMS relies on the excellent performance of its components and thus requires strict quality control before their assembly. The final steps of assembly of 1061 silicon microstrip detector modules for the CMS tracker endcaps are performed at the 1. Physikalisches Institut B at the RWTH Aachen. A laser test facility for these modules was developed and is described in this thesis. In contrast to test procedures based only on the evaluation of pedestal and noise data, the test facility relies on the generation of signals in the silicon sensors by infrared laser illumination. Subsequent analysis of the signals allows reliable detection of module defects. The fully automatic test facility provides high throughput and easy operation for the series production of the modules. Its performance is validated by investigating a reference module with artificially prepared defects of three types: open wirebonds, short-circuited strips and pinholes. It is shown that all defects are clearly detected. In addition to defect detection, an indication for the type of defect is provided. In a further validation step, nine modules from a prototype series are investigated with the laser test facility. Confirming the earlier results on the reference module, defective strips are reliably identified. The results are in agreement with those from other test facilities using different techniques.

Measurements of cosmic ray antiparticles, such as positrons, can impose strong constraints on the nature of new physics beyond the Standard Model. However, cosmic ray positron measurements are experimentally very challenging due to the vast proton background. This thesis describes a novel approach of positron identification with the space-borne AMS-01 experiment, namely through the detection of bremsstrahlung conversion in a silicon microstrip detector. In contrast to earlier single-track analyses, this approach involves the selection and reconstruction of multi-track events. Subsequent to an introduction to cosmic ray physics and a description of the AMS-01 experiment, the discussion of the signal process shows that bremsstrahlung from protons is suppressed by a factor of more than  $3 \cdot 10^6$  with respect to positrons. The background to the positron sample can largely be suppressed using the topological and geometrical properties of the events.

In order to obtain the highest positron selection efficiency possible, novel combinatorial track finding algorithms were developed, particularly optimized for the signature of converted bremsstrahlung. By applying restrictions on the invariant mass of particles the background to the positron sample is largely eliminated. The remaining background contamination is determined from large samples of Monte Carlo data taking into account the effects of the geomagnetic field. It amounts to 26 % of the positron counts and is

corrected for. In order to remove atmospheric secondaries from the positron and electron samples, a precise method involving trajectory backtracing in the magnetic field of the Earth was developed and is applied individually to all positron and electron candidates.

The results of the positron measurement show that the bremsstrahlung approach extends the sensitivity range of AMS-01 to positron momenta up to 50 GeV/c, which is far beyond the original scope of the experiment. The precision of the positron measurement is statistically limited by the small number of particle counts. The positron fraction  $e^+/(e^+ + e^-)$  is calculated for particle momenta in the range from 1 to 50 GeV/c. For momenta up to 8 GeV it is found to be in good agreement with model predictions for background from purely secondary positron production, while at higher momenta there is indication for a positron overabundance. Therefore, the AMS-01 data lend further weight to the hints of a positron overabundance seen in the data from earlier experiments.

In addition to the positron fraction, the absolute fluxes of positrons and electrons are calculated from the event samples of the present analysis. For this purpose, a method was developed which allows the determination of the geomagnetic transmission as a function of momentum and direction of incidence with high accuracy. The results of the flux calculation are found to be in very good agreement with earlier data, confirming the good performance of electron and positron selection with the bremsstrahlung approach.

Finally, the positron fraction results from this analysis have been combined with results from earlier experiments. In the combined results, the significance of the positron overabundance with respect to the background expectation for purely secondary positron production increases to 5.3 standard deviations, which would be reduced to 4.2 standard deviations without the results of the present analysis. Therefore, a statistical fluctuation causing the positron overabundance in the data with respect to the background-only expectation can now be excluded.

# Zusammenfassung

Es ist eine der weitreichendsten Entdeckungen der letzten Jahrzehnte, daß die sichtbare Materie im Universum lediglich einen sehr kleinen Teil zu dessen Gesamtenergiedichte beiträgt. Zu mehr als 75 % ist es von einer vollkommen unbekannten Form von Energie dominiert, für die der Name *Dunkle Energie* geprägt worden ist, während etwa 20 % als gravitierende nichtrelativistische *Dunkle Materie* existieren muß. Unter den zahlreichen Kandidaten für die Konstituenten der Dunklen Materie ist das supersymmetrische (SUSY) Neutralino das vielversprechendste. Die vorliegende Arbeit befaßt sich mit der Suche nach supersymmetrischen Teilchen am zukünftigen Large Hadron Collider (LHC) und dem Bau eines der vier großen LHC-Experimente, dem Compact Muon Solenoid (CMS), und konzentriert sich auf den Nachweis von Signalen aus der Annihilation supersymmetrischer Dunkler Materie in den Spektren der Kosmischen Strahlung.

Die einwandfreie Funktion seiner Komponenten ist eine wesentliche Voraussetzung für den Erfolg eines technisch so anspruchsvollen Großexperimentes wie CMS und macht eine strenge Qualitätskontrolle während ihrer Fertigung erforderlich. Die Endmontage von 1061 Siliziumstreifendetektormodulen für den Spurdetektor von CMS wird im 1. Physikalischen Institut B der RWTH Aachen durchgeführt. Die vorliegende Arbeit beschreibt die Entwicklung eines vollständig automatisierten Testverfahrens zur Qualitätskontrolle dieser Module. Es basiert auf mittels eines Infrarotlasers in den Siliziumsensoren angeregten Signalen, deren Auswertung eine zuverlässige Erkennung von Defekten erlaubt. Um die Anwendbarkeit des Testverfahrens zu bestätigen, wurde ein Referenzmodul mit künstlich präparierten Defekten untersucht. Wie gezeigt wird, können alle Defekte einwandfrei detektiert werden, und es ergibt sich aus der Messung ein Hinweis auf den jeweiligen Defekttyp. Darüberhinaus wurde das Testverfahren zur Untersuchung von neun Modulen einer Prototypserie verwendet. In Übereinstimmung mit den Ergebnissen aus der Untersuchung des Referenzmoduls konnten Moduldefekte zuverlässig identifiziert werden. Die Ergebnisse werden von denjenigen anderer Testverfahren, die auf abweichenden Nachweistechniken beruhen, bestätigt.

Die Energiespektren von Antiteilchen in der Kosmischen Strahlung, wie etwa von Positronen, können wichtige Hinweise auf die Natur der Dunklen Materie liefern. Die Identifizierung von Positronen in der Kosmischen Strahlung stellt experimentell eine erhebliche Herausforderung dar aufgrund des großen von Protonen verursachten Untergrundes. Die vorliegende Arbeit beschäftigt sich mit einem neuen Ansatz zur Identifikation von Positronen auf der Grundlage des Nachweises konvertierter Bremsstrahlungsphotonen in einem Siliziumstreifendetektor. Die Wahrscheinlichkeit der Emission von Bremsstrahlung von Protonen ist gegenüber Positronen um einen Faktor von mehr als  $3 \cdot 10^6$  unterdrückt und erlaubt somit eine Unterscheidung beider Teilchensorten. Dieses Verfahren wurde anhand der Daten des weltraumgestützten AMS-01-Experimentes realisiert. Im Gegensatz zu früheren auf Einzelspurmessungen basierenden Analysen erfordert es die Rekonstruktion von Mehrspureignissen.

Um eine bestmögliche Selektionseffizienz für Positronen zu erreichen, wurden speziell für die Signatur konvertierter Bremsstrahlungsphotonen optimierte Spurfindungsalgorithmen entwickelt. Schnitte auf die invariante Masse der gemessenen Teilchen eliminieren weitgehend den Untergrund zu den Positronkandidaten. Der verbleibende irreduzible

Untergrund wurde mit Hilfe einer großen Anzahl simulierter Ereignisse unter Berücksichtigung des Einflusses des Erdmagnetfeldes bestimmt. Die Zahl der Positronen wurde um diesen Untergrund, der 26 % der Signalereignisse entspricht, korrigiert. Zur Unterdrückung atmosphärischer Sekundärteilchen unter den Positron- und Elektronkandidaten wurde eine Methode entwickelt, die auf der Rückverfolgung von Teilchenspuren im Erdmagnetfeld basiert.

Die Ergebnisse dieser Positronmessung zeigen, daß der Bremsstrahlungsansatz den Meßbereich von AMS-01 bis hin zu Positronimpulsen von 50 GeV/c erweitert, was weit jenseits der ursprünglich angestrebten Reichweite des Experimentes von 3,5 GeV/c liegt. Die Genauigkeit der Positronmessung ist hierbei statistisch limitiert durch die Anzahl der gemessenen Positronen. Weiterhin wurde der Positronenanteil  $e^+/(e^+ + e^-)$  in der Kosmischen Strahlung für Teilchenimpulse im Bereich von 1 bis 50 GeV/c berechnet. Für Impulse bis hin zu 8 GeV/c ist dieser in guter Übereinstimmung mit den Ergebnissen von Modellrechnungen für den Untergrund von ausschließlich sekundär produzierten Positronen. Bei höheren Impulsen hingegen zeichnet sich ein Überschuß von Positronen ab. Somit liefern auch die Daten des AMS-01-Experimentes Hinweise auf einen Positronenüberschuß, wie er bei früheren Experimenten bereits beobachtet wurde.

Zusätzlich zum Positronenanteil wurden auch die absoluten Flüsse von Elektronen und Positronen aus der Anzahl der Kandidaten dieser Analyse errechnet. Hierzu wurde ein Verfahren entwickelt, das es erlaubt, die Durchlässigkeit des Erdmagnetfeldes für Elektronen und Positronen als Funktion des Impulses und der Flugrichtung der Teilchen mit hoher Genauigkeit zu ermitteln. Die Ergebnisse der Flußberechnung zeigen eine sehr gute Übereinstimmung mit denjenigen früherer Messungen.

Abschließend wurde der im Rahmen dieser Arbeit ermittelte Positronenanteil mit den Ergebnissen anderer Experimente statistisch kombiniert. Aufgrund der Ergebnisse der vorliegenden Arbeit steigt die Signifikanz des Positronenüberschusses gegenüber dem erwarteten Untergrund von 4,2 auf 5,3 Standardabweichungen. Somit kann nun eine statistische Fluktuation als Ursache für den Überschuß von Positronen gegenüber dem erwarteten Untergrund weitgehend ausgeschlossen werden.

# Contents

<b>1</b>	<b>Introduction</b>	<b>1</b>
<b>2</b>	<b>Dark Matter in the Universe</b>	<b>5</b>
2.1	The History of the Universe . . . . .	5
2.2	Evidence for Dark Matter . . . . .	7
2.3	The Standard Model of Particle Physics . . . . .	10
2.4	Supersymmetric Dark Matter . . . . .	12
2.5	Approaches to Understanding Dark Matter . . . . .	15
<b>3</b>	<b>SUSY Detection at the LHC</b>	<b>17</b>
3.1	The LHC and its Experiments . . . . .	17
3.2	Discovery Potential of the LHC Experiments for Supersymmetry . . . . .	18
3.3	Silicon Microstrip Detectors for CMS . . . . .	21
3.3.1	The CMS Experiment . . . . .	21
3.3.2	Silicon Microstrip Detectors . . . . .	24
3.4	A Laser Test Facility for Silicon Microstrip Detectors . . . . .	28
3.4.1	Possible Module Defects . . . . .	28
3.4.2	The Setup of the Module Test Facility . . . . .	29
3.4.3	The Test Procedure . . . . .	30
3.4.4	Investigation of Artificially Bonded Defects . . . . .	33
3.4.5	Results from the TEC W6 Prototype Series . . . . .	36
<b>4</b>	<b>Cosmic Rays as Tracers of Dark Matter</b>	<b>41</b>
4.1	Cosmic Ray Composition and Spectra . . . . .	42
4.2	Origin and Propagation of Cosmic Rays . . . . .	43
4.3	Cosmic Rays in the Earth's Vicinity . . . . .	45
4.4	Signatures of SUSY Dark Matter in the Cosmic Ray Spectra . . . . .	48
<b>5</b>	<b>The AMS-01 Experiment</b>	<b>53</b>
5.1	AMS-01 Detector Construction . . . . .	53
5.1.1	The Magnet . . . . .	54
5.1.2	The Time of Flight Hodoscopes . . . . .	55
5.1.3	The Silicon Strip Tracker . . . . .	56
5.1.4	The Aerogel Threshold Čerenkov Detector . . . . .	59
5.1.5	The Veto Counters . . . . .	60
5.1.6	Material Budget . . . . .	60
5.2	Trigger and DAQ Livetime . . . . .	61
5.3	AMS-01 on the Space Shuttle . . . . .	62

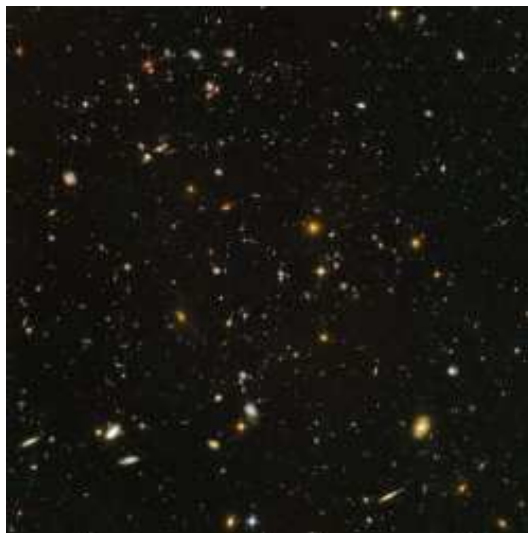
<b>6</b>	<b>Positron Identification through Bremsstrahlung Conversion</b>	<b>65</b>
6.1	The Challenge of Positron Measurements . . . . .	65
6.2	Conversion of Bremsstrahlung Photons . . . . .	65
6.2.1	Event signature . . . . .	66
6.2.2	Background . . . . .	67
6.3	Event Reconstruction . . . . .	69
6.3.1	Preselection . . . . .	69
6.3.2	Track Finding . . . . .	70
6.3.3	Vertex Reconstruction . . . . .	72
6.3.4	Reconstruction Quality and Monte Carlo . . . . .	73
6.4	Analysis . . . . .	75
6.4.1	Basic Cuts . . . . .	76
6.4.2	Suppression of Background . . . . .	79
6.4.3	Effect of the Mir Space Station . . . . .	81
6.4.4	Geomagnetic Cutoff . . . . .	82
6.5	Correction for Irreducible Background . . . . .	83
<b>7</b>	<b>Results of the Positron Measurement</b>	<b>87</b>
7.1	Positron Fraction . . . . .	87
7.1.1	Statistical Errors . . . . .	87
7.1.2	Systematic Errors . . . . .	90
7.1.3	Variation of the Positron Fraction with the Value of the Cut . . . . .	91
7.2	Flux Calculation . . . . .	92
7.2.1	Detector Acceptance . . . . .	93
7.2.2	Calculation of Livetime . . . . .	94
7.2.3	Positron and Electron Fluxes . . . . .	95
<b>8</b>	<b>Conclusions</b>	<b>97</b>
	<b>Acknowledgment</b>	<b>103</b>
	<b>Bibliography</b>	<b>105</b>



# 1 Introduction

The picture shown here is known as the *Hubble Ultra Deep Field* and was taken by the Hubble Space Telescope in 2004 [1]. It is the result of an ultra-long exposure – more than 11 days effectively – to the light coming from a tiny area of the sky, as small as 3 by 3 arc-minutes. In other words, the image represents far less than one millionth of the sphere that surrounds the Earth. An area of this size could easily be obscured by a grain of sand at the distance of an arm.

Apart from a few faint stars which happened to be in the field of view, about 10,000 galaxies appear in the image. With the coarse but reasonable assumption that a typical galaxy contains about one hundred billion stars and that galaxies are uniformly distributed over large scales, one concludes that the total number of stars in the universe must be roughly of the order of  $10^{22}$ , or 10,000,000,000,000,000,000,000. What an unimaginable amount of mass and energy fills the universe!



Nevertheless, in the last few decades it became apparent that luminous matter and all the invisible dust and gas inbetween, whose elementary composition is in principle similar to that of matter in our familiar surroundings, amounts only to a surprisingly small fraction of the energy density in the universe. In reality, the universe must be regarded as essentially dominated by exotic and novel forms of matter, and an even bigger reservoir of strange non-material energy, whose nature yet remains a complete mystery. Consequently, the assertion of basically knowing what fills space must be abandoned and the terms *dark matter* and *dark energy* have been coined for the unknown bulk ingredients of the universe.

At the same time the Standard Model of particle physics, which structures the knowledge about the elementary constituents and interactions of matter, has matured. It has been and still is extraordinarily successful in explaining practically all experimental observations in particle physics and has received continuous confirmation with highest precision for more than two decades. Despite its success, it is widely assumed that the Standard Model must merely be a part of a superior and more comprehensive concept, i.e. it must be a low-energy effective theory truly valid only in the energy regime open to current experiments. Thus a large diversity of hypotheses has emerged to anticipate whatever may appear when the present experimental limits are exceeded. Among such hypotheses, the idea of supersymmetry is one of the most cogent and intriguing.

It is becoming apparent that cosmology, astrophysics and particle physics are simultaneously approaching the same problem from different points of view and that their synergy

may finally lead to a fundamentally new understanding of basic physics. In a manner of speaking, the universe acts as a huge autonomous reactor for all its constituents, even the possibly unknown, and offers by far the most powerful particle accelerators. Therefore, the study of cosmic ray particles can deliver strong constraints on those new phenomena which are as yet beyond the reach of any laboratory experiment and can point the way towards better theoretical and experimental approaches. With the upcoming collider facilities, such as the LHC, it will thus be possible to target new discoveries with greater precision.

This thesis discusses the search for supersymmetry at the future LHC collider and the ongoing construction of one of the four large LHC experiments, the Compact Muon Solenoid (CMS), and focuses on the detection of signals from supersymmetric dark matter candidates in the spectra of cosmic rays. The *second chapter* introduces the question of the nature of dark matter together with an overview of the history and current state of the universe, as well as the evidence for the existence of as yet invisible new forms of matter. The supersymmetric extension of the Standard Model of particle physics leads to the presently most promising dark matter candidate, namely the hypothetical neutralino.

The possible discovery of supersymmetry at the LHC is the subject of *chapter three*. It starts with an overview of the LHC facility and of the four large collider ring experiments. Subsequently, the discovery potential for supersymmetry of the LHC experiments is discussed, including the production mechanisms and the decay channels of supersymmetric particles, as well as the experimental signatures which would allow their detection and the determination of supersymmetry parameters. The CMS experiment at the LHC is currently under construction and will feature the largest silicon microstrip tracker ever built. Such a complex detector relies on the excellent performance of its components and thus requires strict quality control before their assembly. Following an overview of the experiment and in particular of the tracker and its components, a laser test facility for silicon microstrip detector modules is described. The investigation of artificially created module defects establishes the applicability of the test facility and the results of tests of a prototype series of detector modules are presented.

The *fourth chapter* addresses cosmic rays as possible messengers for signals from reactions of supersymmetric dark matter particles. Subsequent to a description of the composition and characteristics of cosmic rays, their origin and propagation in the interstellar medium, as well as the modulation of cosmic ray spectra in the vicinity of the Earth are discussed. As it turns out, the annihilation of neutralinos from dark matter may leave its traces in cosmic rays in the form of an overabundance of particles, particularly of positrons, antiprotons, and gamma rays. The processes involved are therefore described and a characterization of the expected signatures in the corresponding particle spectra is given. The chapter ends with an overview of the evidence for neutralino annihilation which has so far been found in cosmic ray data.

Such evidence still inconclusive and more experimental results are necessary to further investigate the hypothesis of supersymmetric dark matter. While new cosmic ray experiments are under construction or have recently started taking data, existing data from past experiments can be re-examined using new analysis techniques. The second part of this thesis reanalyzes the data taken by the space-borne AMS-01 detector in 1998 with the aim of determining the spectrum of cosmic ray positrons up to energies of 50 GeV, far beyond

the original scope of the experiment. After a detailed description of AMS-01 and its Space Shuttle flight in *chapter five*, *chapter sixth* introduces the challenge of cosmic ray positron measurements and the novel approach of positron identification through the detection of converted bremsstrahlung photons in silicon microstrip detectors. An in-depth description of the analysis includes discussion of the signal and background processes, methods of particle track and vertex reconstruction, background suppression and correction for the background remaining among the signal candidates, as well as the complications which arise due to the circumstances under which AMS-01 was operated, namely the influence on particle detection of the spacecraft and of the magnetic field of the Earth.

The results of the positron measurement are the subject of *chapter seven*, where the positron fraction – the ratio of positron to electron counts  $e^+/(e^+ + e^-)$  in which several systematic uncertainties cancel – is presented as a function of particle momentum. It is shown that by using the conversion of bremsstrahlung photons to tag positrons and electrons in cosmic rays the AMS-01 data substantially improve the knowledge of the cosmic ray positron fraction up to the highest momenta so far accessible to experiments. To validate the tagging method, the chapter ends with the calculation of the absolute fluxes of positrons and electrons based on the results of this analysis and the comparison of these fluxes to the existing data [2, 3].

The *concluding chapter* summarizes the results of this thesis. Finally, the positron fraction measurements from the most recent experiments [4, 5, 6, 7] are combined with the results of this analysis, giving the most precise positron fraction data yet available. The positron fraction measured in this analysis lends further weight to the hints seen in the data of [7] of a positron overabundance for momenta above 6 GeV.



## 2 Dark Matter in the Universe

Over the past decades, numerous pioneering ideas and seminal discoveries have significantly broadened the understanding of the structure and evolution of the universe. The theoretical fundamentals of space-time in an homogeneous and isotropic world based on General Relativity were already known in 1922 to contradict a static universe [8]. Seven years later it was indeed discovered that the recessional velocity of distant galaxies is proportional to their distance, a fact which is nowadays referred to as *Hubble's law* [9]. Hence, the universe was found to be continuously expanding. The manifest idea of the *Hot Big Bang* – postulating that the universe primordially emerged from a tremendously dense and hot state – became increasingly popular, especially when it was shown that it could explain the observed abundances of the lightest nuclei [10, 11]. However, the strongest confirmation for the theory came with the discovery of the cosmic microwave background (CMB) in 1965 [12], an omnipresent electromagnetic radiation field with an almost perfect thermal 2.7 K black-body spectrum, which had been predicted before as a Hot Big Bang relic [13]. Recently, accurate measurements of the fluctuations in the CMB led to a precise determination of the cosmological parameters [14].

The first sky surveys and galaxy mappings surprisingly revealed that there is structure in the distribution of matter at very large scales in the order of 100 Mpc [15]. Using the Big Bang model and assumptions about the types of matter that make up the universe, it is possible to predict the matter distribution. Furthermore, the survey of Type Ia supernovae yields a relation between the host galaxies' redshift and their distance, so that supernovae of this species are regarded as standard candles, allowing to investigate the expansion history of the universe [16]. The large-scale structure and supernova data as well as the CMB results clearly favor a class of models for which the term  $\Lambda$ CDM was coined<sup>1</sup>. The basic statement of the latter is that ordinary matter (also referred to as *baryonic* matter) constitutes only a small fraction of the energy density of the universe [17]. More than 75 % is accounted for by what is called the *dark energy*, and about 20 % must exist in form of some kind of non-relativistic *dark matter*. The nature of these two most dominant forms of energy in the universe is one of the cardinal unsolved questions in modern cosmology, and the answer will doubtlessly give rise to fundamentally new physical concepts. While cosmology is presently far from a distinct approach to solving the dark energy problem, the nature of dark matter is possibly now close to being resolved.

### 2.1 The History of the Universe

The standard model of the universe is the Hot Big Bang model. According to this theory, the universe came into existence 13.7 billion years ago [17], starting in an enormously compressed and very hot state. Very little is known about the first  $10^{-43}$  s, the so called

---

<sup>1</sup>CDM – cold dark matter;  $\Lambda$  denotes the cosmological constant.

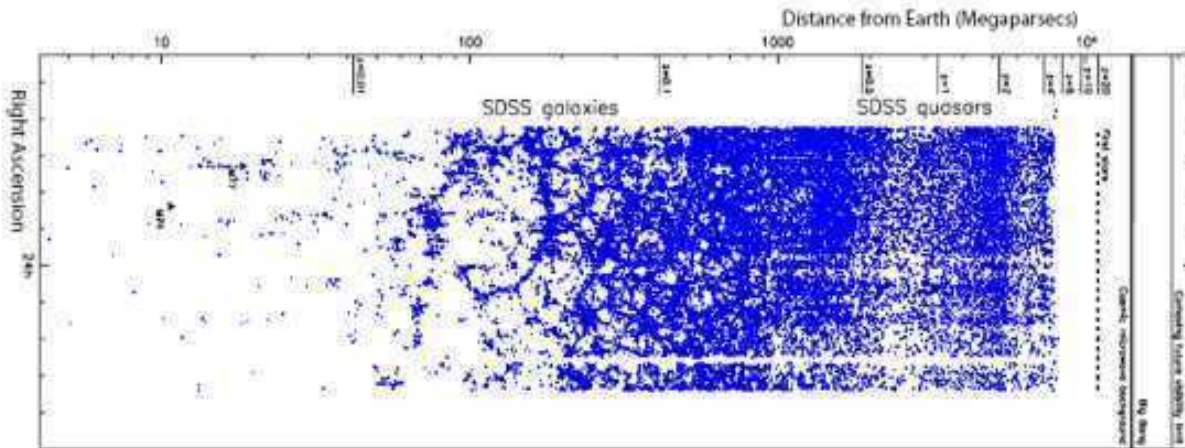


**Fig. 2.1:** A map of the universe: the distribution of distant galaxies exhibits structure on large scales [18].

*Planck Epoch*, in which the three forces we know today (see § 2.3) were presumably unified. After the end of this period, the universe entered an approximately  $10^{-35}$  s long phase of exponentially quick expansion (*inflation*), during which its size increased by about 25 orders of magnitude [19]. The driving force of this process is believed to be a yet unknown scalar field, called the *inflaton*, whose initial quantum fluctuations from the Planck Epoch were blown up to macroscopic scales. These are nowadays represented by the large-scale structure (Figure 2.1). Simultaneously, a possible curvature of space-time in the early universe was stretched out by inflation, giving the universe its Euclidean geometry which is observed today [17].

After the end of inflation, the energy in the universe was dominated by radiation and a sea of relativistic particle-antiparticle pairs near thermal equilibrium [20]. As the universe further expanded and cooled, particle species dropped out of equilibrium once the thermal energy  $k_B T$  fell below their mass, and vanished through annihilation. According to *Sakharov's conditions* [21], the existence of CP-violating (see § 2.3) and baryon number violating processes out of thermal equilibrium may have lead to a tiny surplus of particles with respect to antiparticles which remained. At  $k_B T \approx 200$  MeV,  $10^{-6}$  s after the inflation, a phase transition occurred from a quark-gluon plasma to protons, neutrons, and pions, along with the leptons, antileptons, and photons (*baryogenesis*). When the universe was about 100 s old and  $k_B T \approx 1$  MeV, the temperature was low enough to allow for the creation of light nuclei such as D,  $^3\text{He}$ ,  $^4\text{He}$ , and  $^7\text{Li}$  (*nucleosynthesis*). During this period, the last particle-antiparticle pairs, the electrons and positrons, annihilated.

It took 370,000 years [14] until the temperature was low enough ( $k_B T \approx 0.3$  eV) for stable hydrogen atoms to be formed from the remaining protons and electrons (*recombination*). At that time, the universe became transparent for radiation, which since then propagates almost freely. Today, it has cooled down to 2.7 K and is observable as the remarkably isotropic CMB. With the recombination and until the emergence of the first stars several hundred million years later, the *Dark Age* of the universe had begun.



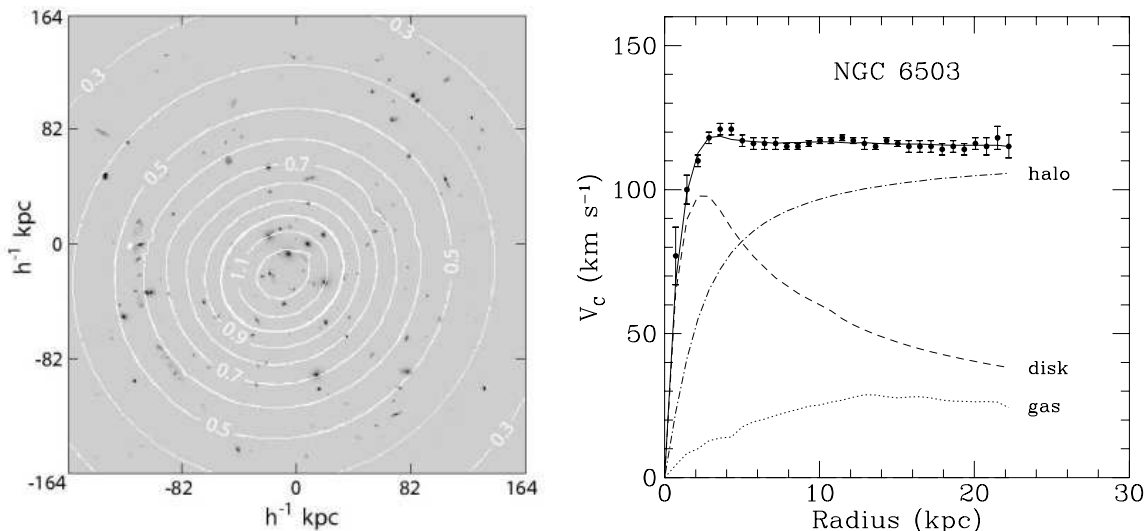


**Fig. 2.2:** The reconstructed surface mass density not associated with visible galaxies in the galaxy cluster CL0024 (white contours, in units of  $2.1 \cdot 10^3 \text{ M}_\odot \text{ pc}^{-2}$ ) superposed on an image by the Hubble Space Telescope [22] (left); rotation curve of the galaxy NGC6503 [23] with contributions from stars (disk), interstellar gas and the dark matter halo (right).

The present universe can be characterized as spatially flat – Euclidean – and homogeneous and isotropic on the largest scales. It is expanding so that objects move away from each other with a speed of 73 km/s per Mpc distance [17]. There is strong evidence that the expansion is presently accelerated [16], which can be explained by the presence of non-material dark energy with particular properties. More than 75 % of the energy density of the universe exists as dark energy, another 20 % as an unknown form of gravitating matter which otherwise does not observably participate in electromagnetic interactions. Energy densities are usually stated as fractions  $\Omega = \rho/\rho_c$  of the *critical density*  $\rho_c$  which leads to a spatially flat universe. The value of  $\rho_c$  corresponds to about six hydrogen atoms per cubic meter. In these terms,  $\Omega_\Lambda = 0.76$  for dark energy,  $\Omega_m = 0.24$  for the total matter density, and  $\Omega_b = 0.04$  for baryonic matter only [17]. The total energy density of the universe is  $\Omega = 1.003 \pm 0.015$  [14]. Matter is concentrated in galaxies, whose spatial distribution exhibits structure on scales of 1-100 Mpc in form of clusters, walls and voids. Since the hot and highly pressurized baryonic matter would have quickly washed out such structure, its formation can best be explained by the presence of dark matter.

## 2.2 Evidence for Dark Matter

Evidence for the presence of significant amounts of invisible matter is numerous and apparent from small to the largest scales. First indication was found as early as 1933 in the Coma galaxy cluster [24], which revealed a mass-to-light ratio two orders of magnitude larger than in the solar neighborhood. The mass of a cluster can be determined via several methods, including application of the virial theorem to the observed distribution of radial

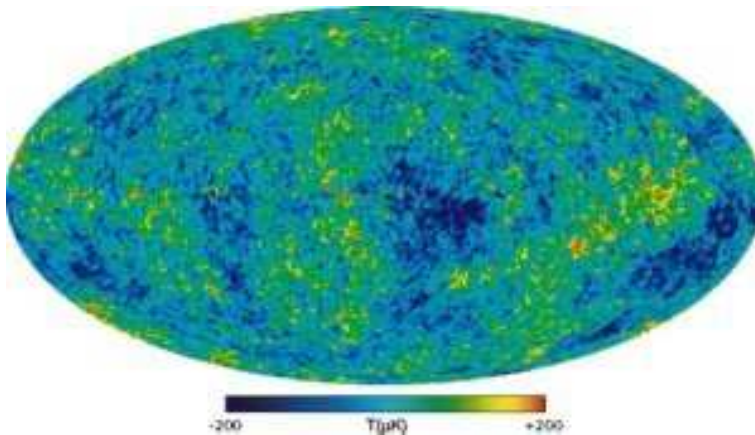


**Fig. 2.3:** Map of CMB temperature fluctuations by WMAP [28].

velocities, by weak gravitational lensing<sup>2</sup> and by studying the profile of X-ray emission that traces the distribution of hot emitting gas [25]. Figure 2.2 (*left*) shows the reconstructed distribution of non-luminous – dark – excess matter in the galaxy cluster CL0024 [22], which apparently concentrates toward the cluster’s center. Recent observations in this field are consistent with a contribution of 20–30 % from matter to the total energy density (see e.g. [26]). This is way above what can be expected from the amount of visible matter alone.

The most direct evidence for dark matter on galactic scales comes from observations on the rotation curves of galaxies. The radial velocity of a star at distance  $r$  from the center of the galaxy is (classically) given by:

$$v(r) = \sqrt{\frac{G \cdot M(r)}{r}}, \quad (2.1)$$

with  $G$  being the gravitational constant, and  $M(r) = \int \rho(r)r^2 dr$  the integrated matter density. Thus, the velocity should be falling  $\propto 1/\sqrt{r}$  outside the luminous galactic disk, as indicated by the dashed rotation curve in Figure 2.2 (*right*) for the galaxy NGC6503 [23]. However, the data show that the actual radial velocity is largely a constant function of the distance from the center. This could be explained with the assumption that the galactic disk is embedded in a *galactic halo* of non-luminous dark matter, represented by the dash-dotted line in Figure 2.2 (*right*). Basically all galaxies studied up to now share this behavior [27].

The spectacular recent CMB measurements from the Wilkinson Microwave Anisotropy Probe (WMAP) [14] and other experiments allow the determination of the cosmological parameters with unprecedented accuracy. The observed temperature anisotropies in the

---

<sup>2</sup>A gravitational lens distorts the image of a background light source. In contrast to strong lensing, where there are easily visible distortions such as multiple images of the light source, weak lensing only leads to faint distortions on the percent level.



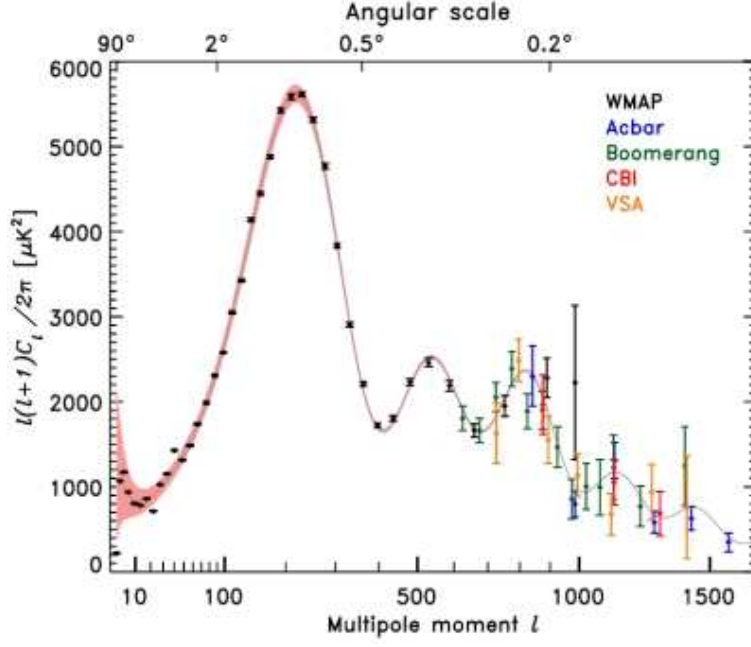


*Fig. 2.4*: A compilation of CMB power spectrum data and the best  $\Lambda$ CDM fit [28].

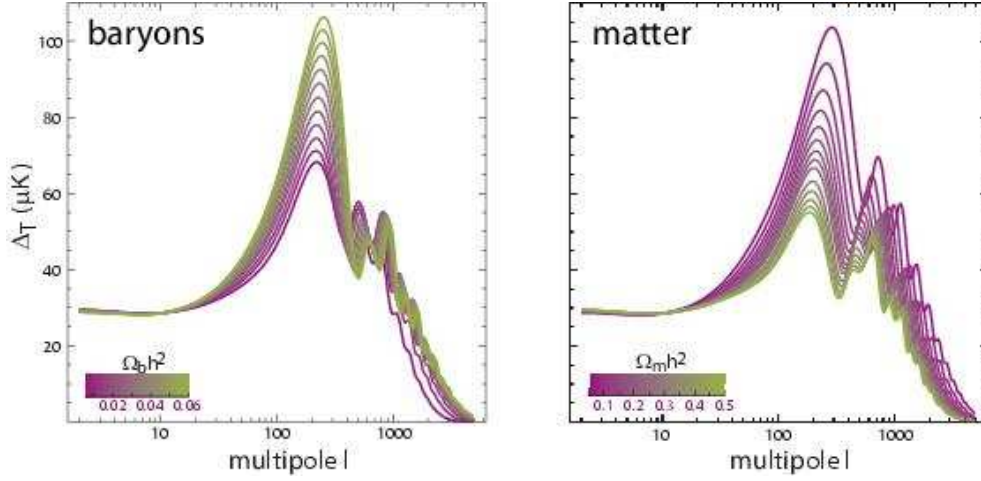


*Fig. 2.5*: Sensitivity of the CMB power spectrum to the baryonic and all-matter energy density contributions  $\Omega_b$  (left) and  $\Omega_m$  (right) [29]. The parameter  $h$  equals about 0.74 [17].

sky (see Figure 2.3) are usually expanded in spherical harmonics  $Y_{\ell m}(\theta, \phi)$  as

$$\frac{\delta T}{T}(\theta, \phi) = \sum_{\ell=2}^{+\infty} \sum_{m=-\ell}^{\ell} a_{\ell m} Y_{\ell m}(\theta, \phi) \quad (2.2)$$

with the variance  $C_\ell \equiv \langle |a_{\ell m}|^2 \rangle$  [25]. Plotted as a function of  $\ell$  in a power spectrum (see Figure 2.4), the variance reveals a noticeable structure with a series of distinct peaks. They

roughly correspond to resonances of acoustic oscillations in the photon-baryon plasma at the time of recombination. The oscillations occurred around the equilibrium of radiation pressure and gravity. Since dark matter gravitates but does not interact with photons, it had a significant impact on the resonances. As a consequence, besides a large set of additional cosmological parameters, the CMB power spectrum is sensitive to the dark matter content of the universe. Figure 2.5 illustrates the effect of varying values of  $\Omega_b$  and  $\Omega_m$  on the power spectrum. The analysis of the data in the framework of the  $\Lambda$ CDM model [17] gives  $\Omega_b h^2 = 0.0223 \pm 0.0008$  and  $\Omega_m h^2 = 0.126 \pm 0.009$  with  $h = 0.74 \pm 0.03$ , which confirms that only about one fifth of the matter content of the universe is comprised of ordinary matter.

As already stated, dark matter has left traces in the large-scale distribution of matter in the universe. Data from recent galaxy surveys [30, 31] yield the spatial density distribution of large numbers of galaxies. The squared Fourier transform of this distribution – the power spectrum  $P(k)$  – constrains large-scale structure formation and cosmological parameters, such as the ratio  $\Omega_b/\Omega_m = 0.185 \pm 0.016$  [30], which is in excellent agreement with the CMB results. Furthermore, it can be inferred from the data that most of the dark matter particles must be nonrelativistic (“cold”) and thus quite heavy, since relativistic particles would have washed out structure on medium scales due to their large free-streaming length.

Altogether, there is clear evidence for the existence of an unknown non-baryonic contribution to the matter content of the universe with an average density corresponding to roughly one hydrogen atom per cubic meter. Hence, the question for the nature of this dark matter arises. Is the current understanding of particle physics sufficient to explain its presence, or will new theoretical approaches be necessary?

## 2.3 The Standard Model of Particle Physics

The Standard Model of Particle Physics (SM) has, for many years, accounted for all observed particles and interactions (see e.g. [32] for reviews). In the SM, the fundamental constituents of matter are particles with half-integer spin (fermions): quarks and leptons. Their interactions are mediated by integer spin particles called gauge bosons. Strong interactions are mediated by gluons  $g$ , electroweak interactions by  $W^\pm$ ,  $Z^0$  and  $\gamma$ . The masses of the fermions and the  $W^\pm$  and  $Z^0$  are generated through the Higgs mechanism [33] via couplings to the Higgs boson  $H^0$ . Gravitation is presently not covered by the SM, since General Relativity and the SM alone cannot be combined in one quantum theory. The left-handed leptons and quarks are arranged into three generations of  $SU(2)_L$  doublets:

$$\begin{pmatrix} \nu_e \\ e^- \end{pmatrix}_L \quad \begin{pmatrix} \nu_\mu \\ \mu^- \end{pmatrix}_L \quad \begin{pmatrix} \nu_\tau \\ \tau^- \end{pmatrix}_L$$

$$\begin{pmatrix} u \\ d' \end{pmatrix}_L \quad \begin{pmatrix} c \\ s' \end{pmatrix}_L \quad \begin{pmatrix} t \\ b' \end{pmatrix}_L \quad (2.3)$$

with the corresponding right-handed fields transforming as singlets under  $SU(2)_L$ . Each generation contains two flavors of quarks with baryon number  $B = 1/3$  and lepton number  $L = 0$  and two leptons with  $B = 0$  and  $L = 1$ . Each particle also has a corresponding antiparticle with the same mass and opposite quantum numbers. The primed quarks are weak eigenstates related to mass eigenstates by the unitary Cabibbo-Kobayashi-Maskawa (CKM) matrix  $V_{\text{CKM}}$  [34, 35] through

$$\begin{pmatrix} d' \\ s' \\ b' \end{pmatrix} = \begin{pmatrix} V_{ud} & V_{us} & V_{ub} \\ V_{cd} & V_{cs} & V_{cb} \\ V_{td} & V_{ts} & V_{tb} \end{pmatrix} \begin{pmatrix} d \\ s \\ b \end{pmatrix} = V_{\text{CKM}} \begin{pmatrix} d \\ s \\ b \end{pmatrix} \quad (2.4)$$

with complex parameters  $V_{ij}$ . Under the assumption that exactly three quark generations exist and that the CKM matrix is unitary, the parameters can be constrained and partially absorbed into arbitrary phases. Four independent parameters remain, one of which can be interpreted as an imaginary phase. In the SM, this phase is responsible for the violation of the CP symmetry, which transforms particles into antiparticles with regard to their handedness.

Local gauge symmetries play a fundamental role in particle physics. It is in fact in terms of symmetries and using the formalism of gauge theories that electroweak and strong interactions are described. The SM is based on the  $SU(3)_C \otimes SU(2)_L \otimes U(1)_Y$  gauge theory, which undergoes the spontaneous breakdown

$$SU(3)_C \otimes SU(2)_L \otimes U(1)_Y \rightarrow SU(3)_C \otimes U(1)_Q, \quad (2.5)$$

where  $Y$  and  $Q$  denote the weak hypercharge and the electric charge generators, respectively, and  $SU(3)_C$  describes the strong (color) interaction, known as Quantum Chromodynamics (QCD). This spontaneous symmetry breaking results in the generation of the massive  $W^\pm$  and  $Z$  gauge bosons as well as a massive scalar Higgs field.

The only viable dark matter candidate from the SM particle table is the neutrino  $\nu$ . The neutrino number density is known to be about 3/11 of the CMB photon density [36], thus yielding  $\Omega_\nu = \sum m_\nu c^2 / (h^2 \cdot 93.8 \text{ eV})$  with the sum running over the three generations. With an upper limit on the sum of the neutrino masses of  $0.72 \text{ eV}/c^2$  (95 % C.L.) from large-scale structure and CMB data [17], the energy density contribution from neutrinos can be constrained to  $\Omega_\nu < 0.014$ . Hence, neutrinos seem unlikely to constitute a relevant fraction of the dark matter in the universe. Further candidates from conventional physics include primordial black holes (see e.g. [36]) or massive objects<sup>3</sup> such as cold dwarf stars [37]. Up to now there has been no evidence that one of these is a good candidate, and in particular baryonic matter cannot constitute more than a small fraction of the total dark matter, thus it is likely that new physics needs to be introduced in order to approach the nature of dark matter. There is a wide range of candidates from non-Standard Model theories, including, amongst many others, axions and Kaluza-Klein states (see e.g. [25, 36] for reviews). However, the best motivated are provided by *supersymmetric extensions* to the SM.

---

<sup>3</sup>referred to as MACHOS – massive compact halo objects

Standard Model particles and fields		Supersymmetric partners			
Symbol	Name	Interaction eigenstates Symbol	Mass eigenstates Name	Symbol	Name
$q = d, c, b, u, s, t$	quark	$\tilde{q}_L, \tilde{q}_R$	squark	$\tilde{q}_1, \tilde{q}_2$	squark
$l = e, \mu, \tau$	lepton	$\tilde{l}_L, \tilde{l}_R$	slepton	$\tilde{l}_1, \tilde{l}_2$	slepton
$\nu = \nu_e, \nu_\mu, \nu_\tau$	neutrino	$\tilde{\nu}$	sneutrino	$\tilde{\nu}$	sneutrino
$g$	gluon	$\tilde{g}$	gluino	$\tilde{g}$	gluino
$W^\pm$	$W$ -boson	$\tilde{W}^\pm$	wino	$\tilde{\chi}_{1,2}^\pm$	chargino
$H^-$	Higgs boson	$\tilde{H}_1^-$	higgsino		
$H^+$	Higgs boson	$\tilde{H}_2^+$	higgsino		
$B$	$B$ -field	$\tilde{B}$	bino	$\tilde{\chi}_{1,2,3,4}^0$	neutralino
$W^3$	$W^3$ -field	$\tilde{W}^3$	wino		
$H_1^0$	Higgs boson	$\tilde{H}_1^0$	higgsino		
$H_2^0$	Higgs boson	$\tilde{H}_2^0$	higgsino		
$H_3^0$	Higgs boson				

**Tab. 2.1:** Standard Model particles and their superpartners in the MSSM [25].

## 2.4 Supersymmetric Dark Matter

Supersymmetry (SUSY) [38] is a generalization of the space-time symmetries of quantum field theory that transforms fermions into bosons and vice versa. In other words, the generators  $Q$  of supersymmetry act on particle fields as

$$Q|\text{fermion}\rangle = |\text{boson}\rangle, \quad Q|\text{boson}\rangle = |\text{fermion}\rangle, \quad (2.6)$$

such that there exist superpartners of the SM fields which mix or directly form supersymmetric particles (*"sparticles"*). Supersymmetry was originally postulated as a solution for the problem of quadratically divergent renormalization corrections to the Higgs boson mass, as such divergences cancel out with the introduction of equally heavy superpartners of the SM fields. Additionally, supersymmetry at TeV energies could modify the running coupling constants of electroweak and strong interactions in a way that they naturally converge to a common value at some very high energy scale  $\sim 2 \cdot 10^{16}$  GeV (GUT<sup>4</sup> scale) [39]. This physically attractive feature of SUSY is not present in the SM framework alone. Moreover, in contrast to the SM, the local extension of supersymmetry (*supergravity*) may provide a framework for the unification of the known forces with gravity.

The *Minimal Supersymmetric Standard Model* (MSSM) has the smallest possible field content necessary to give rise to all the particles of the SM (see Table 2.1). In the MSSM, unlike the SM, two Higgs doublets, corresponding to five physical Higgs bosons, are needed to give masses to all the fermions. The four *neutralinos*  $\tilde{\chi}_{1,2,3,4}^0$  are linear combinations of the superpartners of the gauge bosons  $B$  and  $W^3$  and the neutral components of the

---

<sup>4</sup>GUT – grand unified theories

Higgs doublets (higgsinos), as

$$\tilde{\chi}_i^0 = c_{1i}\tilde{B} + c_{2i}\tilde{W}^3 + c_{3i}\tilde{H}_1^0 + c_{4i}\tilde{H}_2^0, \quad (2.7)$$

while the two *charginos*  $\tilde{\chi}_{1,2}^\pm$  represent superpositions of the charged components  $\tilde{H}^\pm$  and  $\tilde{W}^\pm$  of the wino and the higgsinos. One additional ingredient usually used to constrain the MSSM is the conservation of *R-parity*. *R* is a multiplicative quantum number defined as  $R \equiv (-1)^{3B+L+2S}$  for a particle with spin *S*, baryon number *B* and lepton number *L*. All SM particles have  $R = 1$  and all their superpartners have  $R = -1$ . As a consequence of *R*-parity conservation, SUSY particles can only decay into an odd number of SUSY particles, plus SM particles. Therefore, the *lightest supersymmetric particle* (LSP) is stable.

If SUSY were an exact symmetry of nature, then particles and their superpartners would have identical mass. Since sparticles have not yet been observed, SUSY must be a broken symmetry. The simplest symmetry breaking mechanism, spontaneous symmetry breaking, is experimentally ruled out at a mass scale below 1 TeV [40]. Thus SUSY is thought to be broken spontaneously in a *hidden sector*, which consists of sparticles which do not directly interact with the *visible* SM particles or their superpartners. Symmetry breaking is then communicated to the visible sector via superheavy messenger particles. The cancellation of quadratic divergences mentioned above cannot be maintained in a broken SUSY, however the remaining divergences are only logarithmic and also proportional to the mass difference of particles and their superpartners. As a consequence, the sparticle masses are constrained and at least several of them should not significantly exceed 1 TeV/ $c^2$  [38]. Thus sparticles are in principle accessible to high energy colliders such as the LHC, which will be the subject of the next chapter.

The MSSM has 124 free parameters, compared to 19 of the SM<sup>5</sup> [40]. In the so called *minimal supergravity* (mSUGRA) models, gravitation is additionally taken into account, so that the spin-2 graviton has a spin-3/2 fermion superpartner called *gravitino*. Gravitational interactions then communicate the symmetry breaking from the hidden to the visible sector. In the mSUGRA case the number of parameters can be significantly reduced by assuming that the model obeys a set of well motivated boundary conditions at the highest energies, thus eliminating all but 5 parameters:

- $\tan\beta$ , the ratio of the vacuum expectation values of the two Higgs doublets,
- $m_{1/2}$ , the common gaugino mass at the GUT scale,
- $m_0$ , the common scalar mass at the GUT scale,
- $A_0$  denoting the trilinear couplings of Higgs bosons to the sfermions, and
- $\text{sign}(\mu)$ , the sign of the Higgs boson mass parameter.

This small number of parameters makes mSUGRA a fruitful field for supersymmetry phenomenology. Figure 2.6 (*left*) shows the plane spanned by the parameters  $m_0$  and  $m_{1/2}$  for fixed values of  $\tan\beta$ ,  $A_0$  and  $\text{sign}(\mu)$ . Large regions can already be excluded on a theoretical basis, for example the region  $m_0 \gg m_{1/2}$ , where the model does not

---

<sup>5</sup>Here, the neutrinos are considered to be massless.



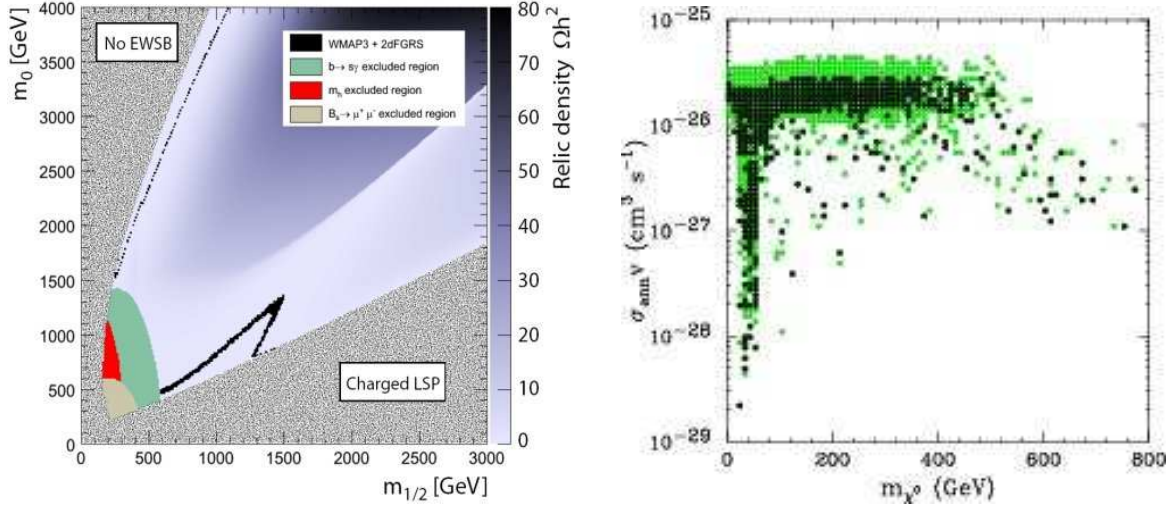


**Fig. 2.6:** Constraints on the mSUGRA parameters  $m_0$  and  $m_{1/2}$  and the neutralino relic density in the allowed regions for  $\tan \beta = 52$ ,  $A_0 = 0$ ,  $\mu > 0$ . The grey dotted and solid colored regions are excluded. The black contour denotes the cosmologically allowed region [41] (left); neutralino annihilation cross sections for parameters in the MSSM which are compatible with  $\Omega_{\text{CDM}} h^2 = 0.095 - 0.129$  (dark points) or  $\Omega_{\text{CDM}} h^2 = 0.06 - 0.16$  (light green points) for  $\tan \beta = 50$  [42] (right).

feature electroweak symmetry breaking (see previous section), or at low  $m_0$ , where the LSP would be a charged sparticle. Further constraints are imposed by a wide range of data from e.g. WMAP, collider and cosmic ray experiments [41]. For the allowed regions, the corresponding neutralino relic density  $\Omega_\chi h^2$  is given. The black contour denotes the region consistent with results from WMAP and galaxy surveys. The allowed regions are typically located close to the borders of the excluded areas.

In mSUGRA and in a multitude of other SUSY models, the LSP is the lightest of the four neutralinos  $\tilde{\chi}_1^0$ . The mass of the  $\tilde{\chi}_1^0$  is currently constrained by collider experiments to be larger than 46 GeV/c<sup>2</sup> (95 % C.L.) [32]. Neutralinos are Majorana particles, thus they can annihilate pairwise into SM particle states (see § 4.4). The product of the annihilation cross section times the particle velocity  $\sigma_{\text{ann}} v$  as a function of the  $\tilde{\chi}_1^0$  mass is displayed in Figure 2.6 (right) for those sets of MSSM parameters which are consistent with the WMAP observations with  $\tan \beta = 50$ . Apparently, the data prefer neutralino masses of few hundred GeV and  $\sigma_{\text{ann}} v \approx 10^{-26} \text{cm}^3 \text{s}^{-1}$ . Given these numbers, it can be calculated that neutralinos must have left the primordial equilibrium at non-relativistic energies and that the cross section is indeed close to the rough expectation of  $\sigma_{\text{ann}} v \approx 10^{-25} \text{cm}^3 \text{s}^{-1}$  for particles in this mass range annihilating through weak interactions [43]. Taking all this into account, the neutralino appears as one of the most favorable candidates for particles which constitute large parts of cold dark matter in the universe: it has a high mass but does not carry charge, interacts only weakly with ordinary matter, has the correct abundance and propagates at non-relativistic speeds. Particles with these properties are generally referred to as *weakly interacting massive particles* (WIMPs). The fact that the neutralino does interact at all and, moreover, is embedded in a framework of other

sparticles, in principle opens the possibility to identify it as the constituent of dark matter by experiment.

## 2.5 Approaches to Understanding Dark Matter

It has been pointed out in this chapter that evidence for the existence of dark matter is widespread in astrophysics and cosmology. The fact that particle physics can provide reliable models for dark matter candidates has established a new creative interplay of these domains in the recent past. A number of collider and non-accelerator experiments are currently operating or will soon be deployed that will shed light on dark matter. In addition, there exist both direct and indirect non-accelerator dark matter search experiments that are ongoing or proposed [44]. Prospects for detecting dark matter and determining its properties are particularly bright in the case of the supersymmetric neutralino.

From the view of particle physics, the dark matter question is strongly connected to those new physical phenomena which inevitably wait at energies beyond the reach of present experiments. Therefore, the particle physics program includes searching for supersymmetric particles at new collider facilities, particularly the LHC, to possibly identify the LSP and determine its properties. The LHC and its experiments are currently under construction, so that their completion is naturally among the primary tasks regarding the search for dark matter. Since the field of supersymmetry contains an enormous variety of ideas, models and parameters, input from the domain of astronomy essentially helps to put constraints on supersymmetry and to focus the theoretical as well as the experimental work on realistic scenarios.

From the view of astrophysics and cosmology, particle physics offers checkable predictions about the behavior of dark matter and its relation to fundamental concepts of cosmology and the evolution of the universe. However, evidence for the existence of dark matter and insight in its properties come from various domains in astrophysics and cosmology, and these can deliver data at energies which are currently unreachable for collider experiments. The so called *direct detection* of WIMPs is based on the measurement of nuclear recoils in elastic WIMP scattering processes [45], while the *indirect search* for dark matter is concerned with the detection of WIMPs through the analysis of their annihilation products in cosmic rays. At present, the experimental data show that the cosmic ray fluxes of positrons [7], antiprotons [46], and gamma rays [47] are not quite in agreement with expectations, and that these discrepancies may well be interpreted as a signal of WIMP annihilation (see chapter 4). However, the data are still too sparse to make convincing statements. Hence, while waiting for new experiments to be deployed in the near future, putting more effort into the analysis of existing data can yield results with increased significance.





## 3 SUSY Detection at the LHC

### 3.1 The LHC and its Experiments

The *Large Hadron Collider* (LHC) [48, 49, 50] is currently under construction at the CERN particle physics laboratory in the same underground tunnel where the LEP collider [51, 52] was previously housed. It will provide proton-proton collisions at a center-of-mass energy of 14 TeV, as well as heavy ion collisions (lead-lead) up to 1.15 PeV. Two separated beam pipes will be used to circulate the protons or ions. The particles are forced on their trajectories by an 8.3 T magnetic field produced by superconducting magnets and are accelerated by superconducting radio frequency cavities. First operation of the LHC is scheduled for 2007 with beam energies of 450 GeV [53].

A certain process, which is characterized by its cross section  $\sigma$ , occurs with a rate  $\dot{N} = \mathcal{L}\sigma$ , where  $\mathcal{L}$  is the luminosity of the accelerator. The LHC is designed for a final luminosity  $\mathcal{L} \approx 10^{34} \text{ cm}^{-2}\text{s}^{-1}$  in the proton-proton mode, however it is planned to run at  $\mathcal{L} \approx 10^{33} \text{ cm}^{-2}\text{s}^{-1}$  during the *low luminosity phase* for three years [54], which sums to approximately  $30 \text{ fb}^{-1}$  integrated luminosity. To achieve the design luminosity the two beams will guide up to 2808 bunches of about  $1.15 \times 10^{11}$  protons each. The bunch spacing will be 25 ns, which is equivalent to a bunch crossing rate of 40 MHz. Within

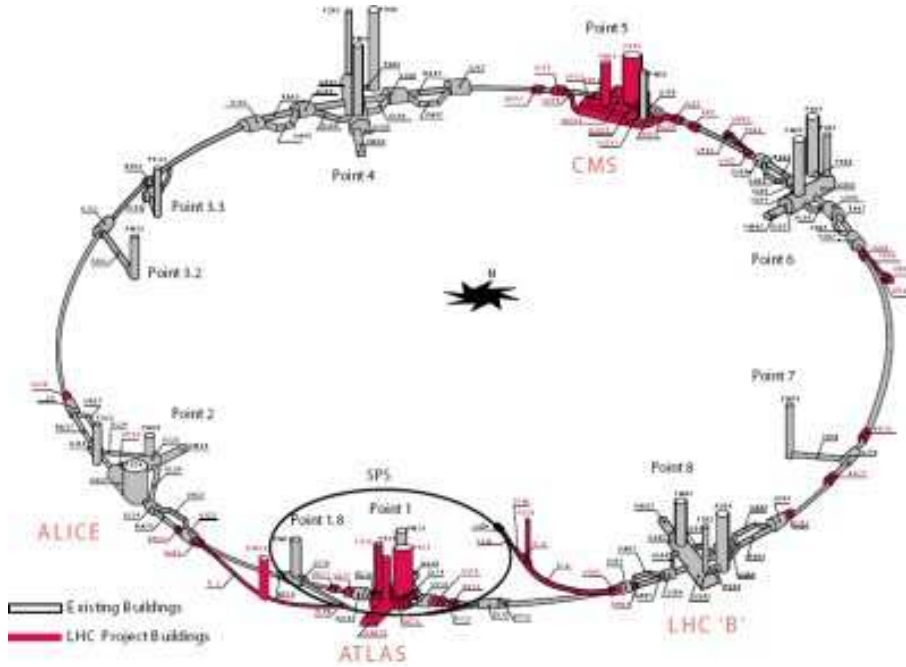


*Fig. 3.1:* The underground structures and experiments of the LHC [49].

the total circumference of about 26.7 km, there will be eight arcs and straight sections. Each straight section is approximately 528 m long and can serve as an experimental or utility insertion. As shown in Figure 3.1, four large experiments will be situated in the four beam crossing sites along the collider:

- ATLAS [55], which is characterized by its sophisticated superconducting air-core toroid muon spectrometer, and features liquid argon calorimetry and silicon pixel and microstrip tracking, as well as transition radiation detectors, within a 2 T solenoid field;
- CMS [56, 57], which is described in more detail below;
- LHCb [58, 59], an experiment dedicated to studying phenomena related to CP-violation and rare B-meson decays at low luminosity, and
- ALICE [60], which is customized for the investigation of ion-ion collisions.

ATLAS and CMS are multi-purpose experiments and were optimized to perform high quality measurements in pp collisions of leptons, hadronic jets and high energy photons. The two detectors have been designed following similar guiding principles and differ mainly in the choice of detector technologies. While ATLAS has invested a large fraction of its resources into superconducting toroid magnets and into a set of precise muon chambers, CMS has put emphasis on the highest possible magnetic field combined with an inner tracker consisting solely of silicon pixel and silicon microstrip detectors, which provide high granularity at all radii. Main topics of the experiments' physics programs are the investigation of the mechanism responsible for electroweak symmetry breaking, which involves finding the Higgs boson, top quark physics and B-meson studies. However, since the LHC is often referred to as a *discovery machine*, a very important task is to search for new physics at high energies, such as SUSY.

## 3.2 Discovery Potential of the LHC Experiments for Supersymmetry

Assuming that supersymmetry is in fact realized in nature, its discovery at the LHC will be relatively straightforward [61]. There are many possibilities to create superpartners at a hadron collider: besides the quark-antiquark annihilation channel, there are numerous processes of gluon fusion, quark-antiquark and quark-gluon scattering. Gluon fusion leads to the largest cross sections, of the order of a few picobarn. SUSY would be revealed by an excess of events with a number of characteristic signatures over the standard model expectations. With  $R$ -parity conserved, the final state in the decay chains of sparticles always contains LSPs, which escape the experiment undetected. Hence, signatures of SUSY are characterized by typically large values of missing transverse energy  $\cancel{E}_T$ .

Table 3.1 gives an overview of the most common initial sparticle states and their expected signatures at the LHC. At LHC energies, the total sparticle production cross section is dominated by strongly interacting gluinos and squarks. They initiate decay cascades which lead to the occurrence of final states with numerous jets and leptons and missing energy due to the existence of at least two LSPs and possibly neutrinos [61]. As a

initial state	main decay modes	signature
$\tilde{g}\tilde{g}, \tilde{q}\tilde{q}, \tilde{g}\tilde{q}$	$\left. \begin{array}{l} \tilde{g} \rightarrow q\bar{q}\tilde{\chi}_1^0 \\ q\bar{q}'\tilde{\chi}_1^\pm \\ g\tilde{\chi}_1^0 \end{array} \right\} m_{\tilde{q}} > m_{\tilde{g}}$ $\left. \begin{array}{l} \tilde{q} \rightarrow q\tilde{\chi}_i^0 \\ \tilde{q} \rightarrow q'\tilde{\chi}_i^\pm \end{array} \right\} m_{\tilde{g}} > m_{\tilde{q}}$	$\cancel{E}_T + \text{multijets (+leptons)}$
$\tilde{\chi}_1^\pm \tilde{\chi}_2^0$	$\tilde{\chi}_1^\pm \rightarrow \tilde{\chi}_1^0 \ell^\pm \nu, \tilde{\chi}_2^0 \rightarrow \tilde{\chi}_1^0 \ell\ell$ $\tilde{\chi}_1^\pm \rightarrow \tilde{\chi}_1^0 q\bar{q}', \tilde{\chi}_2^0 \rightarrow \tilde{\chi}_1^0 \ell\ell,$	three leptons + $\cancel{E}_T$ two leptons + jet + $\cancel{E}_T$
$\tilde{\chi}_1^+ \tilde{\chi}_1^-$	$\tilde{\chi}_1^\pm \rightarrow \tilde{\chi}_1^0 \ell^\pm \nu$	two leptons + $\cancel{E}_T$
$\tilde{\chi}_i^0 \tilde{\chi}_i^0$	$\tilde{\chi}_i^0 \rightarrow \tilde{\chi}_1^0 X, \tilde{\chi}_i^0 \rightarrow \tilde{\chi}_1^0 X'$	two leptons + jet + $\cancel{E}_T$
$\tilde{t}_1 \tilde{t}_1$	$\tilde{t}_1 \rightarrow c\tilde{\chi}_1^0$ $\tilde{t}_1 \rightarrow b\tilde{\chi}_1^\pm, \tilde{\chi}_1^\pm \rightarrow \tilde{\chi}_1^0 q\bar{q}'$ $\tilde{t}_1 \rightarrow b\tilde{\chi}_1^\pm, \tilde{\chi}_1^\pm \rightarrow \tilde{\chi}_1^0 \ell^\pm \nu,$	2 noncollinear jets + $\cancel{E}_T$ single lepton + $\cancel{E}_T + b$ two leptons + $\cancel{E}_T + b$
$\tilde{l}\tilde{l}, \tilde{l}\tilde{\nu}, \tilde{\nu}\tilde{\nu}$	$\tilde{\ell}^\pm \rightarrow \ell^\pm \tilde{\chi}_i^0, \tilde{\ell}^\pm \rightarrow \nu_\ell \tilde{\chi}_i^\pm$ $\tilde{\nu} \rightarrow \nu \tilde{\chi}_1^0$	two leptons + $\cancel{E}_T$ single lepton + $\cancel{E}_T$

**Tab. 3.1:** Compilation of initial sparticle states, main decay modes, and their signatures at the LHC [62].

consequence of LSP production, a complete mass reconstruction of gluinos and squarks is possible only in long decay chains. So SUSY signal observability is based on an excess of events of a given topology over known or expected backgrounds. Figure 3.2 (*left*) shows the distribution of the quantity  $M_{\text{eff}}$  – i.e. the sum of  $\cancel{E}_T$  and the transverse momenta  $p_T$  of the four highest energetic jets – for events with  $\cancel{E}_T > 100$  GeV and at least four jets with  $p_T > 50$  GeV/c, compared to the SM background. With an integrated luminosity of  $10 \text{ fb}^{-1}$ , the signal over background ratio is approximately 10 for large values of  $M_{\text{eff}}$  [55].

The LHC can discover squarks and gluinos up to masses well in excess of  $2 \text{ TeV}/c^2$ , which covers the entire parameter space over which supersymmetry can plausibly be relevant to electroweak symmetry breaking. In Figure 3.2 (*right*) the reach of the gluino/squark search is displayed for  $10 \text{ fb}^{-1}$  of data. The solid lines show the  $5\sigma$  contours for final states with different lepton multiplicity. Additionally, contour lines for the resulting neutralino dark matter densities  $\Omega h^2 = 0.25, 0.5$  and  $1.0$  are given. The cosmologically preferred density of  $\Omega h^2 \approx 0.1$  (see chapter 2) is well within the reach of the LHC.

Sleptons can be produced in pairs, for example, directly via  $q\bar{q}$  annihilation. If sleptons are more massive than the lightest charginos and neutralinos, they decay directly into these via  $\tilde{\ell}^\pm \rightarrow \ell^\pm \tilde{\chi}_{1,2}^0$  or  $\tilde{\ell}^\pm \rightarrow \nu_\ell \tilde{\chi}_1^\pm$ . Similar decay channels exist for sneutrinos. On the contrary, light sleptons can indirectly originate from charginos and neutralinos via e.g.  $\tilde{\chi}_2^0 \rightarrow \tilde{\ell}^\pm \ell^\mp$  or  $\tilde{\chi}_1^\pm \rightarrow \tilde{\nu}_\ell \ell^\pm$ , where the charginos and neutralinos themselves dominantly stem from gluino and squark pairs. This leads to an experimental signature characterized

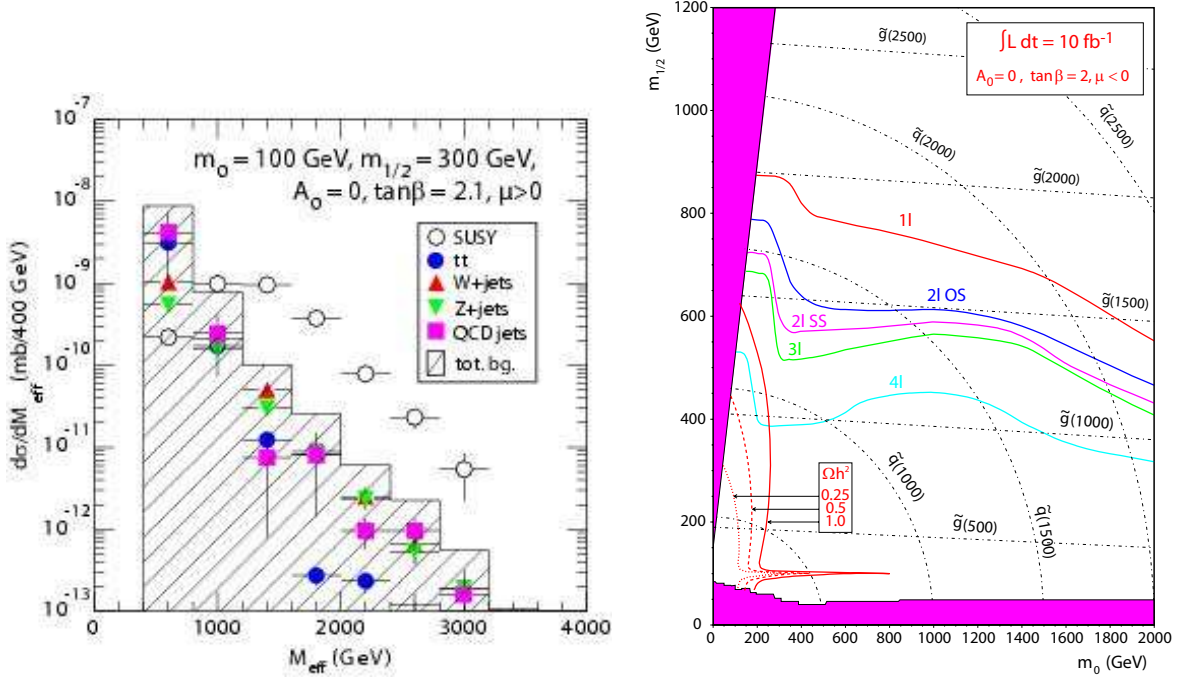


**Fig. 3.2:** Distribution of  $M_{\text{eff}}$  for the SUSY signal and the expected background for an integrated luminosity of  $10 \text{ fb}^{-1}$  (left) [63]; reach ( $5\sigma$  contours) of the gluino/squark search in various lepton multiplicity final states (OS – opposite charge sign; SS – same sign) for  $10 \text{ fb}^{-1}$ . The neutralino dark matter density contours of  $\Omega h^2 = 0.25, 0.5$  and  $1.0$  are also shown. Dash-dotted lines denote squark/gluino isomass contours (right) [61].

by 2 isolated leptons, missing transverse energy, and the absence of jets, which allows to detect sleptons up to masses of about  $350 \text{ GeV}/c^2$  [61].

Following the possible detection of SUSY signals in channels such as those described above, the most important tasks would be to measure the particle masses and to narrow down the range of model parameters. Leptonic decays of the second-lightest neutralino,  $\tilde{\chi}_2^0$ , have a useful kinematical feature: the two-lepton invariant mass spectrum has an edge near the kinematical upper limit with a maximum value of  $m_{\ell^+\ell^-}^{\text{max}} = m_{\tilde{\chi}_2^0} - m_{\tilde{\chi}_1^0}$  in the case of direct three-body decays via  $\tilde{\chi}_2^0 \rightarrow \ell^+\ell^-\tilde{\chi}_1^0$ , and

$$m_{\ell^+\ell^-}^{\text{max}} = \sqrt{(m_{\tilde{\chi}_2^0}^2 - m_{\tilde{\ell}}^2)(m_{\tilde{\ell}}^2 - m_{\tilde{\chi}_1^0}^2)}/m_{\tilde{\ell}} \quad (3.1)$$

in the case of two-body cascade decays  $\tilde{\chi}_2^0 \rightarrow \ell^\pm \tilde{\ell}^\mp \rightarrow \ell^+\ell^-\tilde{\chi}_1^0$ , thus allowing a measurement of the mass difference of the two neutralinos. The  $\tilde{\chi}_2^0$  dominantly stem from gluinos, which decay into heavy quark-squark pairs, as for example  $\tilde{g} \rightarrow b\bar{b}$ ,  $\tilde{b} \rightarrow \tilde{\chi}_2^0 b$ . Thus the experimental signature is characterized by the occurrence of isolated same-flavor opposite-charge lepton pairs in conjunction with at least four jets. Figure 3.3 (left) shows the invariant mass of lepton pairs from events which match these requirements for an integrated luminosity of  $30 \text{ fb}^{-1}$  and a particular choice of parameters. The background expected from SM processes is also shown. While the narrow peak around  $90 \text{ GeV}/c^2$

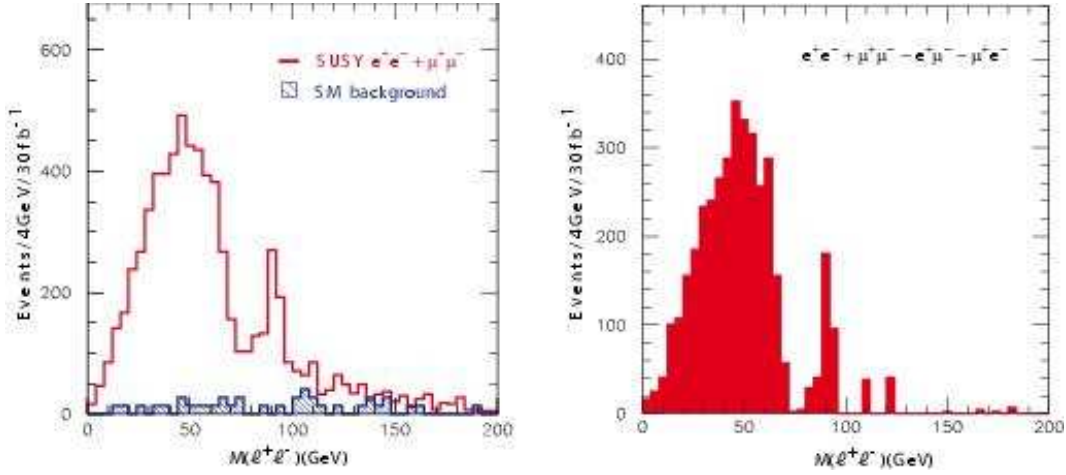


**Fig. 3.3:** Distribution of the dilepton invariant mass for  $m_0 = 800 \text{ GeV}/c^2$ ,  $m_{1/2} = 200 \text{ GeV}/c^2$ ,  $A_0 = 0$ ,  $\tan \beta = 10$ ,  $\mu > 0$ , and the SM background, for  $\mathcal{L}_{\text{int}} = 30 \text{ fb}^{-1}$  (left); same with mixed-flavor pair distribution subtracted (right). Taken from [55].

stems from  $Z^0$  production in the decays of heavy neutralinos, the edge at lower invariant masses indicates the mass difference  $\Delta m_\chi = m_{\tilde{\chi}_2^0} - m_{\tilde{\chi}_1^0}$ , which in this case approximately equals  $68 \text{ GeV}/c^2$ . The background is mostly due to  $t\bar{t}$  or  $WW$ +jet production. However, in that case the final state contains as many same-flavor leptons as different-flavor ones and with identical distributions. Hence, by subtracting the different-flavor distribution, the SM background can be canceled up to statistical fluctuations (Figure 3.3, right).  $\Delta m_\chi$  can then be determined with a statistical accuracy of about  $50 \text{ MeV}/c^2$  [55].

As eq. (3.1) suggests, the dilepton edge is also sensitive to the intermediate slepton mass. Through analysis of particular kinematical distributions, the masses of the two lightest neutralinos as well as the slepton mass can be determined [61]. Additionally, events near the edge can be used to reconstruct the  $\tilde{\chi}_2^0$  momentum vector. This would permit the search for resonance structures in the distribution of the  $\tilde{\chi}_2^0$ +jet invariant mass and possibly provide access to the mass of the decaying squarks. Apart from these event topologies, a variety of other signatures would facilitate the determination of sparticle masses and SUSY model parameters [55, 57, 61, 63, 64, 65]. The ultimate goal of such studies would be to use very many measurements to make an overconstrained fit to the model, rather in the same way that current data are used to test the SM.

## 3.3 Silicon Microstrip Detectors for CMS

### 3.3.1 The CMS Experiment

CMS is a general purpose high energy physics experiment which is particularly optimized for the detection of particles stemming from proton-proton collisions. Its design goals comprise, amongst others, providing a high-quality and redundant muon system, best possible electromagnetic calorimetry and excellent tracking in a strong magnetic field.



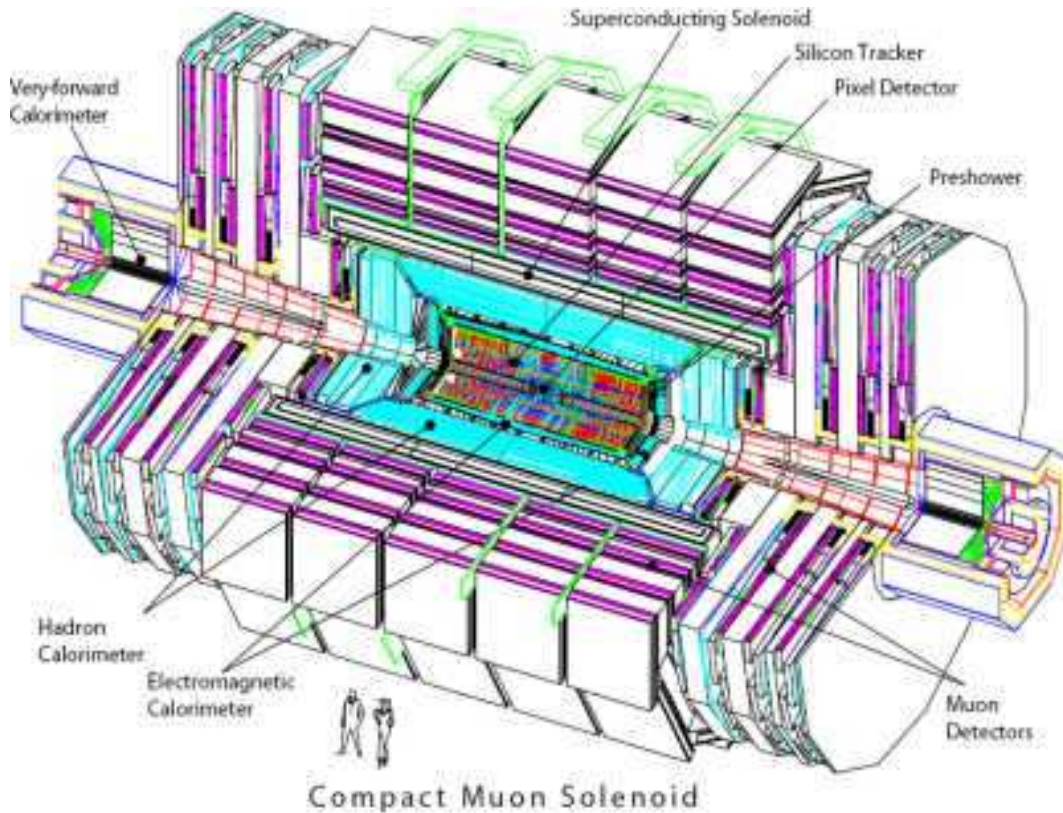


*Fig. 3.4:* The CMS experiment (from [56]).

Its layout is that of a classical hermetic detector with a barrel region and two endcaps, covering practically the full  $4\pi$  solid angle. CMS will have a length of 21.6 m, a diameter of 14.6 m, and 14500 t of weight [66]. Figure 3.4 gives an overview of the experiment and its subdetectors, which will briefly be discussed in the following.

**The Magnet System** [67] consists of a superconducting solenoid coil in conjunction with a saturated iron yoke for flux return. The 12.5 m long solenoid will provide an homogeneous magnetic field of 4 T in the central region, which decreases to about 1.7 T in the outermost parts of the experiment.

**The Muon System** [68] is integrated in the return yoke of the magnet system and will be used to identify muons and measure their charge sign and momentum. Furthermore, it will play an important role for triggering the CMS experiment. The Muon System consists of three subdetectors: drift tube chambers in the barrel region, cathode strip chambers in the endcaps, and fast resistive plate chambers in both the barrel and endcap. When combined with data from the tracker, the expected momentum resolution  $\sigma_{p_T}/p_T$  for muons ranges from 1 % for  $p_T < 10$  GeV/c to about 6–17 % for  $p_T = 1$  TeV/c, depending on the direction of the emerging particle. The Muon System also provides a track reconstruction efficiency of better than 90 % in the transverse momentum range up to 100 GeV/c, decreasing to  $\gtrsim 70$  % at  $p_T = 1$  TeV/c.

**The Calorimeters** [69, 70] of CMS will measure the energy and direction of electrons, photons and jets and, moreover, deliver information crucial for the trigger system.

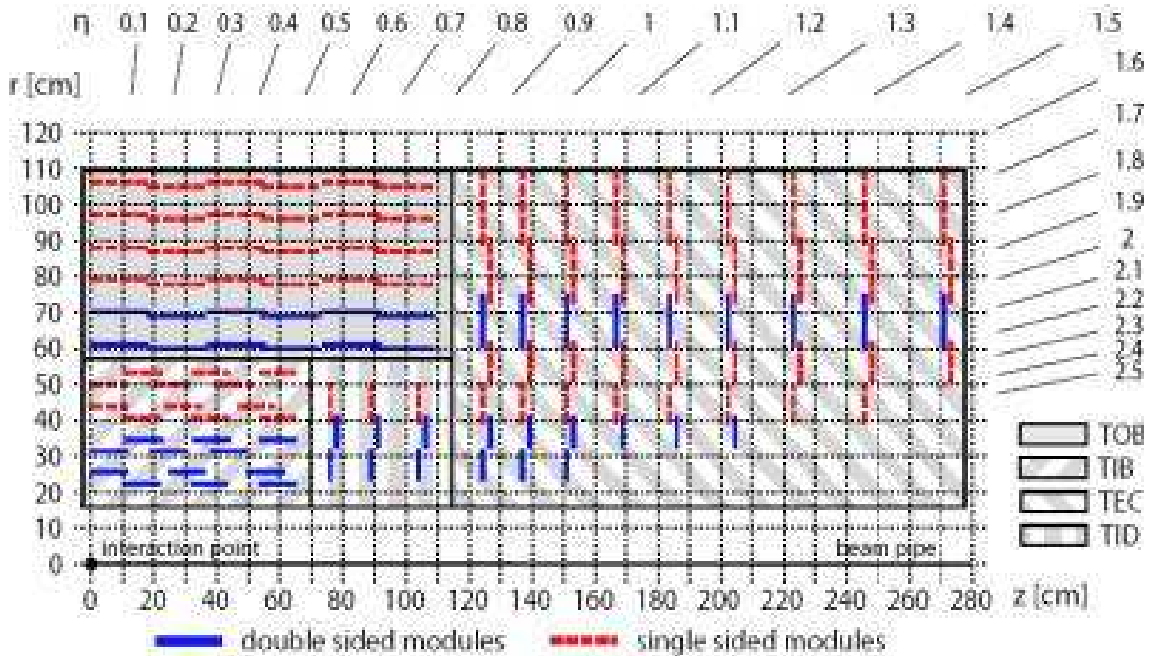


**Fig. 3.5:** Cross section through one octant of the CMS silicon strip tracker [72]. The pixel detector is not shown.

They are divided into two parts, the electromagnetic calorimeter (ECAL) and the hadron calorimeter (HCAL). The complete ECAL and most parts of the HCAL are located within the magnet coil. The ECAL is composed of 82728 scintillating  $\text{PbWO}_4$  crystals with a depth of 25.8 (barrel) and 24.7 (endcap) radiation lengths, read out by avalanche photodiodes and vacuum phototriodes, respectively. In the barrel part, the ECAL granularity is  $2.2 \times 2.2 \text{ cm}^2$ , providing an excellent separation power for close-to-collinear particles. The endcaps have less fine granularity and a silicon strip preshower detector will be installed in front of them to help with  $\pi^0$ - $\gamma$  separation.

The HCAL consists of a barrel and two endcap (HC) sections inside the magnet coil and a tail catcher outside the magnet. It is a sampling calorimeter composed of copper absorber plates interleaved with 4 mm (front part) or 8 mm (back part) plastic scintillator tiles read out by hybrid photodiodes. In addition two forward quartz fiber calorimeters (HF) are placed around the beam pipe beyond the endcap magnet yokes to provide hermetic closure of the detector. The energy resolution  $\sigma_E/E$  of the calorimeters is given by

$$\left(\frac{\sigma_E}{E}\right)^2 = \left(\frac{a}{\sqrt{E}}\right)^2 + \left(\frac{\sigma_n}{E}\right)^2 + b^2, \quad (3.2)$$

with  $E$  in units of GeV and  $a = 2.7\%$ ,  $\sigma_n = 155 \text{ MeV}$ ,  $b = 0.5\%$  for the ECAL (barrel,  $\eta = 0$ ), and  $a = 100\%$ ,  $b = 4.5\%$  with negligible  $\sigma_n$  for the HCAL with the ECAL in front.

**The Tracking System** [71, 73] consists of two subsystems, the pixel detector and the silicon strip detector, with an overall transverse momentum resolution of  $\delta p_T/p_T \lesssim$

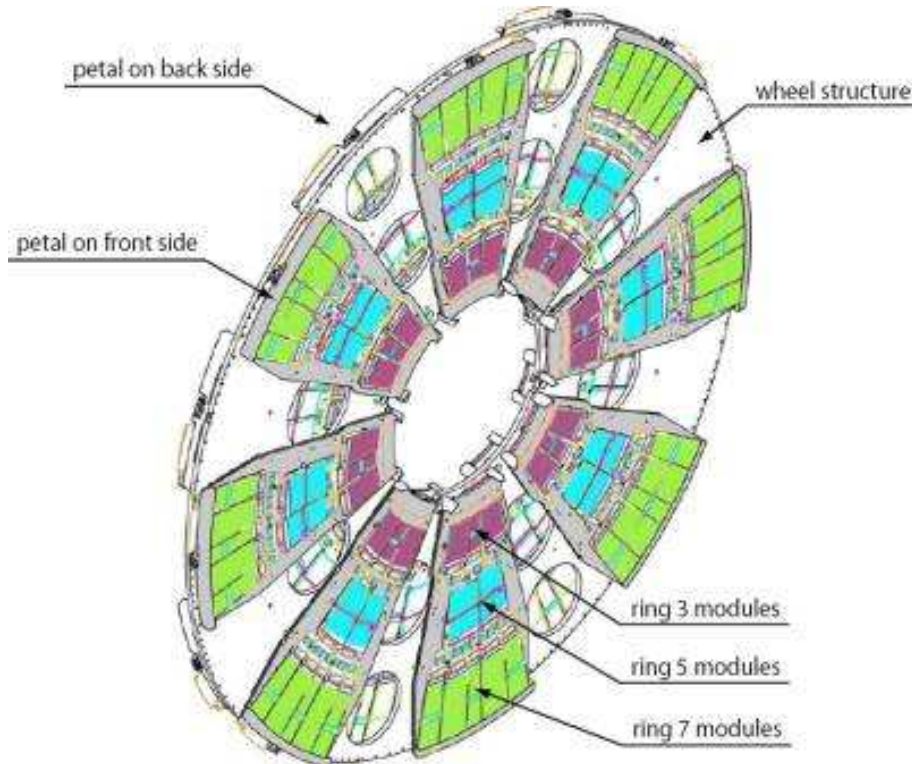


**Fig. 3.6:** Schematic view of the fourth TEC disk ( $z \approx 170$  cm). It carries 16 petals – eight on the front and eight on the back side – on which the silicon strip modules are mounted. The petals on this disk do not carry modules of ring 1 (compare Figure 3.5).

( $15 \cdot p_T / \text{TeV} \oplus 0.5$ ) %. The pixel detector forms the innermost part of the tracker, close to the beam pipe. It consists of three 53 cm long barrel layers and two endcap disks on each side of the barrel. The barrel layers are placed at distances of 4.4, 7.3 and 10.2 cm from the beam line, while the two disks are situated at 34.5 and 46.5 cm from the interaction point. To achieve an equally good hit resolution of  $15 \mu\text{m}$  in the transverse and the longitudinal planes, a design with a square pixel shape of dimensions  $150 \times 150 \mu\text{m}^2$  and thickness  $300 \mu\text{m}$  is used [74].

The pixel detector is enclosed by the silicon strip detector (SST). With more than 15000 silicon modules, adding up to a total active silicon area of about  $200 \text{ m}^2$ , and roughly 10 million electronics channels, it will be the largest silicon detector ever built [72]. Figure 3.5 displays a cross section through one octant of the SST and shows its division into four subsystems: the *Tracker Inner Barrel* (TIB), the *Tracker Inner Disks* (TID), the *Tracker Outer Barrel* (TOB) and the *Tracker Endcaps* (TEC). The TEC and their components are described in the next section.

### 3.3.2 Silicon Microstrip Detectors

Each TEC consists of nine circular disks perpendicular to the beam direction, on which the silicon sensors are mounted via modular support structures (*petals*) as shown



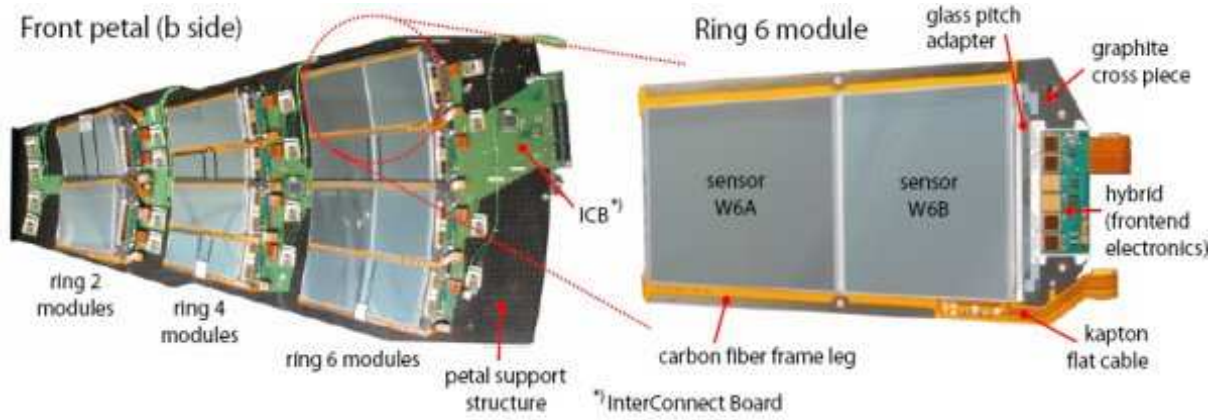


**Fig. 3.7:** Photograph of a fully assembled TEC petal (b-side), carrying modules of rings 2, 4 and 6, and a view of a 22.5 cm long ring 6 module [72].

in Figure 3.6. One or two silicon sensors are integrated in *modules* together with the frontend readout electronics. The modules are arranged on both sides of the support structures forming up to seven concentric *rings* around the beam pipe with the sensitive strips oriented radially. Modules belonging to odd-numbered rings (1, 3, 5 and 7) are mounted on one petal side, while those of even-numbered rings (2, 4 and 6) are mounted on the other side, so that there is an overlap between adjacent rings in  $r$  and  $\phi$ . Rings 3, 4, 6 and 7 have single sided modules consisting of one single silicon plane. Modules of the rings 1, 2 and 5 are double sided (*stereo*) with two coplanar silicon planes mounted back to back and tilted at an angle of 100 mrad with respect to each other. Since at a given  $z$  position the silicon microstrip sensors are sensitive only to one of the coordinates spanning the sensor plane, single sided modules yield measurements of only the  $\phi$  and  $z$  coordinates of particle hits, while double sided modules measure all coordinates simultaneously. The spatial resolution of single hit measurements in a TEC sensor is about  $30\,\mu\text{m}$ . Figure 3.7 shows a fully assembled petal (b-side), carrying modules of rings 2, 4 and 6. Due to the overall circular geometry of the TEC the modules have a trapezoidal shape and increase in size towards the outer edge of the disks.

For the modules of ring 6, the Physikalisches Institut 1B at the RWTH Aachen is involved in the final assembly steps of wirebonding. Such a ring 6 module is shown in the enlarged view on the right side of Figure 3.7. Two carbon fiber frame legs are connected via a graphite plate (*cross piece*), serving as the mechanical support structure for the two trapezoidal silicon sensors named W6A and W6B. The latter are electrically insulated from the support structure with bands of kapton foil, which at the same time carry electrical circuitry for the application of high voltage to the sensors. The frontend electronics, assembled on a kapton/copper board laminated on thin ceramics (*hybrid*), are glued on the cross piece. A thin glass plate with strip conductors, the *pitch adapter*, guides the signals from the sensors to the readout electronics. Each of the single sided (double sided) sensors has 512 (768) readout strips. For ring 6 the strip pitch varies from

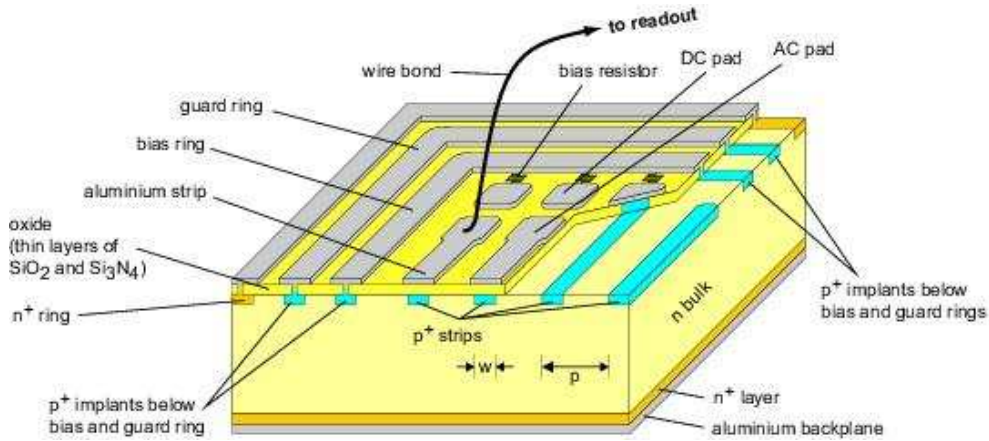


**Fig. 3.8:** Schematic cross section of a silicon microstrip sensor [75].

163 to 205  $\mu\text{m}$ . The inter-strip connections from sensor to sensor, sensor to pitch adapter, and pitch adapter to hybrid are established via 25  $\mu\text{m}$  aluminum wirebonds.

The structure and working principle of a silicon microstrip sensor is illustrated in Figure 3.8. Strips of  $p^+$  doped silicon are implanted into the surface of the 500  $\mu\text{m}$  thick<sup>1</sup>  $n^+$  doped silicon bulk. They are insulated via a continuous  $\text{SiO}_2/\text{Si}_3\text{N}_4$  layer, and are covered with aluminum metallization for readout purposes (*strips*). The strip width varies between 53 and 67  $\mu\text{m}$  for ring 6 modules. In this configuration, the implants form a series of p-n junctions, with the aluminum strips capacitively coupled to them. On both ends of each strip, the aluminum broadens and forms two *AC pads* to house the wirebond. In addition to the AC pads, *DC pads* are located beyond the ends of each strip. These provide a direct connection to the implants and are thus not used for wirebonding. The DC pads are connected to the *bias ring* via 1.5 M $\Omega$  polysilicon bias resistors, hence providing all implants with a common potential. The opposite surface of the sensors is finished with a thin  $n^+$  silicon layer and finally coated with an aluminum backplane.

The frontend electronics on the hybrid are equipped with APV25-S1<sup>2</sup> [76] integrated circuits (IC). The APV25-S1 is a 128 channel analog pipeline with 192 columns of analog storage. Each strip is connected to one single electronics channel. Strip signals are amplified into 50 ns shaped pulses of magnitude 100 mV per 25000 electrons. These are sampled at a rate of 40 MHz and stored in the pipeline. Useful data are marked after a programmable latency, and held in the pipeline until such a time that they can be read out. If no trigger is received within 4.8  $\mu\text{s}$  the pipeline cells are overwritten. A set of 512 strip signals is referred to as an *event* in the following. The APV25-S1 can be operated in two different readout modes; in *peak mode* only one sample per channel is read from the pipeline while in *deconvolution mode* three samples are read sequentially, and the final output is the weighted sum of all three. In the latter case, the shaping constant is reduced from 50 ns to 25 ns at the expense of slightly higher noise. Besides a set of other parameters, the gain of the amplifier stage of the APV25-S1 can be varied. In addition

<sup>1</sup>For rings 5–7; sensors of the rings 1–4 have a thickness of 300  $\mu\text{m}$  instead.

<sup>2</sup>APV – Analogue Pipeline (Voltage mode)

to the APV25-S1, the hybrid houses an IC to multiplex a pair of two APV25-S1 analog outputs onto a single differential line (*MUX*), the *detector control unit (DCU)* IC for slow control purposes and an IC for processing the trigger signal supplied by the CMS trigger electronics (*TPLL*) [77].

With a voltage  $V$  applied to the sensor backplane and the bias ring grounded, the p-n junctions are reverse biased, and *depletion zones* form at their locations. The width  $d$  of the depletion zones can be calculated in good approximation as

$$d \approx \sqrt{\frac{2\epsilon\epsilon_0}{qN_D}V}, \quad (3.3)$$

where  $N_D$  is the effective doping concentration and  $q$  is the elementary charge. Full depletion is reached if  $d$  equals the sensor thickness  $d_s$ , hence the corresponding depletion voltage  $V_{\text{dep}}$  is found to be

$$V_{\text{dep}} \approx \frac{qN_D}{\epsilon\epsilon_0} \frac{d_s^2}{2}, \quad (3.4)$$

equal to about 100 V for  $N_D \approx 0.5 \cdot 10^{12}/\text{cm}^{-3}$  [71] in a  $500\mu\text{m}$  thick ring 6 sensor. However, it must be pointed out that  $N_D$  and consequently  $V_{\text{dep}}$  will strongly vary as the silicon is irradiated during operation of the CMS experiment, essentially leading to a type inversion from the initially n-type silicon to p-type silicon [78].

Charged particles traversing the sensor ionize the silicon and create electron-hole pairs. A minimum-ionizing particle (MIP) deposits a most probable energy of 260 eV within  $1\mu\text{m}$  of material along its flight path [32]; with an energy of 3.6 eV required to create one electron-hole pair in silicon [79], it follows that a MIP releases about 36000 pairs or 5.8 fC per charge sign when traversing a ring 6 sensor. The charge carriers are separated in the electric field of the depletion zones and move towards the electrodes. The signal is then created on the aluminum strips by induction and carried to the frontend electronics through the wirebonds.

Irradiation with light also generates electron-hole pairs in silicon. The penetration depth  $a$  – i.e. the depth at which the intensity  $I$  of the incident light has decreased to  $1/e$  of its initial value  $I_0$  – strongly depends on the wavelength  $\lambda$ . In the near infrared domain, it is a monotonously increasing function of  $\lambda$ , and reaches a value of about  $400\mu\text{m}$  at  $\lambda = 1050\text{ nm}$  in the case of pure silicon [80]. The mean depth  $\bar{x}$  of energy loss of light in a silicon sensor of thickness  $b$  as the expectation value of the intensity distribution  $I(x) = I_0 \cdot \exp(-x/a)$  along  $x$  is

$$\bar{x} = a - b \cdot \frac{e^{-b/a}}{1 - e^{-b/a}}. \quad (3.5)$$

For  $\lambda = 1050\text{ nm}$  and  $b = 500\mu\text{m}$ ,  $\bar{x}$  equals  $200\mu\text{m}$ , which is close to  $\bar{x} = 250\mu\text{m}$  obtained for the uniform energy loss attributed to a MIP. Although the silicon of the sensors is not pure but doped, the effect of the doping concentration on  $\bar{x}$  is negligible for photons with energies above the 1.12 eV band gap of silicon, equivalent to a wavelength of 1107 nm.

There exist several sources of noise superimposed on the strip signals. Besides noise due to thermal excitations in the silicon, to the readout electronics and low-frequency

voltage noise, the module output suffers to a small extent from the so called *common mode noise* (CMN), which is basically caused by electromagnetic pick-up at the APV25-S1 preamplifier inputs. One characteristic feature of the CMN is that it simultaneously affects groups of strips, and thus appears as a shift of their common baseline randomly varying with time. The APV25-S1 features a facility for CMN reduction; it has an external resistor in the power supply line common to all 128 channels, which collectively drives down their output in case of a CMN pulse. The remaining CMN can be determined and subsequently subtracted for each of these groups separately within the data of one event.

During the intended operating time of ten years, the components of the CMS tracker will be exposed to an aggressive environment. The radiation level within the tracker volume will be extremely high, such that some components will encounter a fluence of up to  $1.6 \cdot 10^{14}$  MeV-equivalent neutrons per  $\text{cm}^2$  [81]. As a consequence, the silicon has to be protected from radiation damage by cooling it to a temperature of  $-10^\circ\text{C}$ .

## 3.4 A Laser Test Facility for Silicon Microstrip Detectors

To provide a stable and proper operation of the CMS tracker according to its performance specifications, care has to be taken that all assembled components fulfill strict quality requirements. Regarding the silicon microstrip detector modules, these requirements are summarized within a grading scheme as follows [82]. Modules are classified as *grade A* if they have less than 1 % defective strips, as *grade B* if they have between 1 and 2 % defective strips, or *grade C* otherwise. Modules of grades A and B are used for tracker assembly with grade A preferred. In addition to the requirement regarding defective strips, modules may also be disqualified due to deviations in their electric properties, the response of the frontend electronics and the mechanical precision of assembly.

### 3.4.1 Possible Module Defects

After completing the ring 6 module assembly with the final steps of sensor to sensor and sensor to pitch adapter wirebonding, there are three main categories of flaws which may be responsible for the occurrence of a defective strip:

- **Open or missing wirebonds**, which are caused by flawed calibration of the wire-bonding facilities or improper handling of the modules. In principle, this category also includes interruption of any signal lines, such as the pitch adapter conductors or the aluminum strips themselves. Open or missing wirebonds can largely be repaired.
- **Inter-strip short-circuits** – ohmic contacts between adjacent strips – which almost exclusively result from manufacturing defects. They degrade the detector resolution and are in most cases irreparable defects. Hence, inter-strip short-circuits are considered in the module grading and must therefore be identified.
- The so called **pinholes**, which represent ohmic contacts between the aluminum strips and the underlying  $\text{p}^+$  implants through the insulating oxide/nitride layer. Pinholes may result from manufacturing defects or from flawed wirebonding. One

particular issue about pinholes is that already a single one allows current to flow from the sensor bulk into the frontend electronics, possibly leading to a breakdown of the corresponding 128 APV25-S1 channels at a time. Hence, strips affected by pinholes must be detected and detached from the hybrid by removing the wirebonds.

A test facility for silicon microstrip detector modules must reliably detect defects from these three categories. It has to provide easy handling and, once the module is mounted for testing, fully automatic operation and high throughput are required. In total, 1061 ring 6 modules (including spares) are produced for the SST, all of which are wirebonded at the Physikalisches Institut 1B at the RWTH Aachen. A test facility for these modules, which meets the above requirements, has been developed and is described in the following.

#### 3.4.2 The Setup of the Module Test Facility

The basic principle of the module test facility (MTF) is the generation of signals in the silicon sensors by laser illumination and their subsequent analysis. As will be shown, each defect leaves a signature in the signal of the affected strip, characteristic of each of the above categories and allowing their detection and tagging. Since the implants are capacitively coupled to the readout strips, the illuminating laser must be pulsed.

The modules are read out via the ARC<sup>3</sup> system [77, 83]. ARC is a multicomponent readout system developed for module testing purposes and comprises the ARC controller board, two frontend hybrid adapters, an ISA card interface for personal computers, and the operating software package ARCS. The ARC board represents the core of the system and performs clock and trigger generation and distribution, data sampling and buffering, as well as slow control and voltage control for the IC on the hybrids. Two modules can be read out in parallel; their data are sampled by a group of three 8-bit analog-to-digital converters at optionally 20 or 40 MHz. The ARC board additionally accepts external trigger signals. Of the two frontend adapters, one houses amplifiers, line drivers and communication circuits while the other serves as a voltage regulator for the hybrids. The operating software ARCS is arranged in three levels: a hardware device driver, a package of communication routines written in the high-level programming language C++, and a graphical user interface. In the configuration implemented in the MTF, the ARC system can deliver data at a maximum rate of about 200 Hz. A detailed description of ARC is given in [77].

The electronic and optical signal lines of the MTF are depicted in Figure 3.9. They are grouped in two branches, a laser or signal generation branch and a branch for trigger generation and readout. Both branches start at the pulse generator's output jacks, which deliver two separate square-wave signals with a duty cycle of 50% and a frequency of 180 Hz. The first signal with positive voltage and an amplitude of 0.8 V is fed in the laser unit, which emits at a central wavelength of 1050.5 nm with an amplitude of 0.43 mW. This infrared light is guided via a single-mode optical fiber to the laser optics, which focus the beam on the silicon sensor surface at a distance of 50 mm. The resulting laser spot has a nearly Gaussian intensity profile with a minimum achievable width of 10  $\mu\text{m}$ . For

---

<sup>3</sup>ARC – APV readout controller



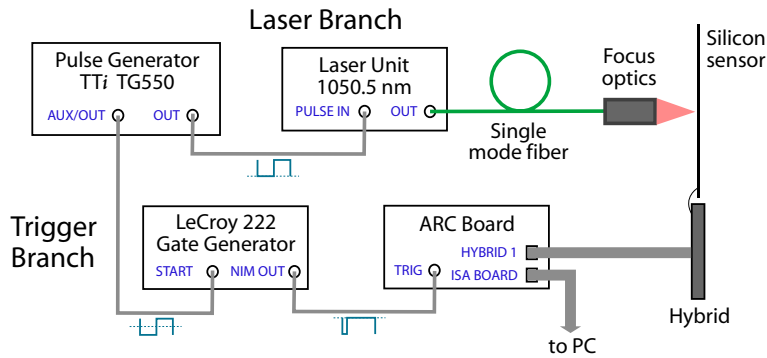


**Fig. 3.9:** Schematic view of the laser test facility's optical and electrical circuitry.

the purpose of module testing, the spot width has been fixed close to this minimum value, so that the strips can be targeted individually.

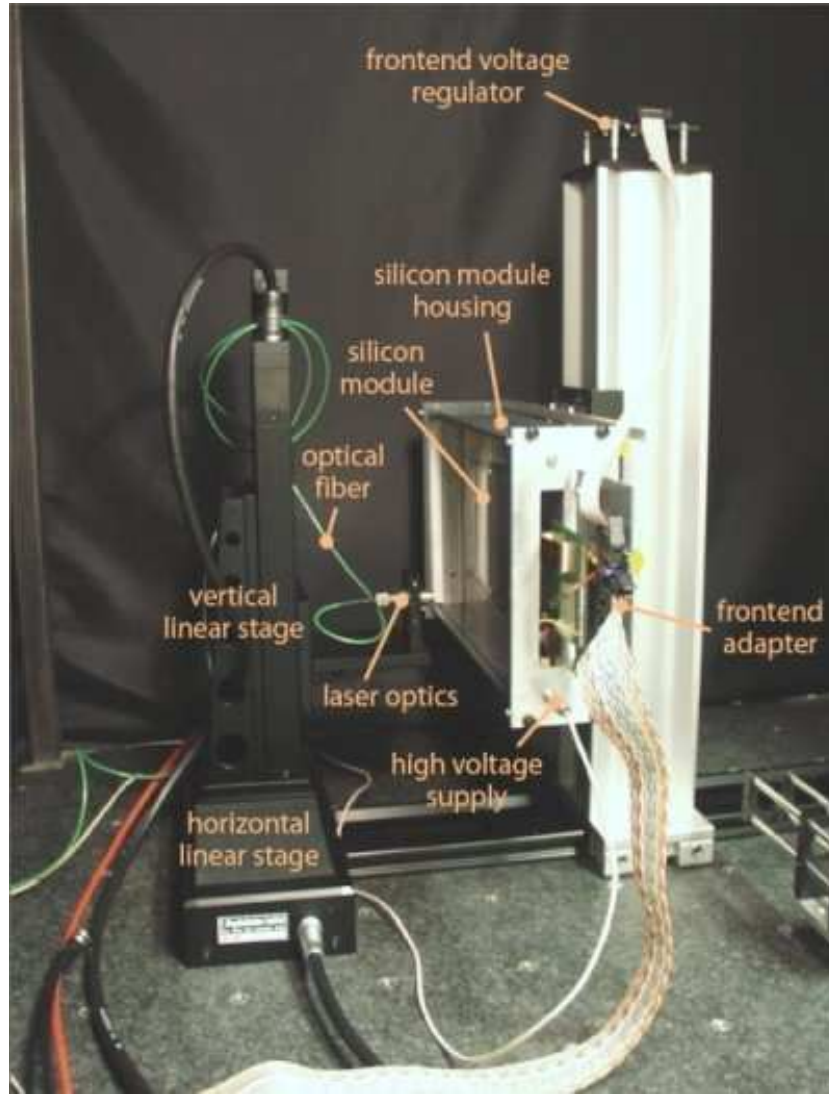
Simultaneously, a second signal leaving the pulse generator with alternating voltage sign is fed into the trigger unit (gate generator), which transforms it into a series of standardized logic NIM<sup>4</sup> signals with voltages of 0 V and  $-0.8$  V for logic 0 and 1 respectively. The output is connected to the trigger input jack of the ARC board. On the arrival of a logic 1 pulse, the ARC board executes the readout sequence of the APV25-S1 at a constant phase with respect to the laser pulse inducing signals in the silicon sensor. The phase – i.e. the pipeline slot to be read out – is determined by the difference of the total delay times for signals traveling along the two branch lines and has been optimized by sampling tests.

Figure 3.10 shows a photograph of the mechanical layout of the MTF. During the final steps of their assembly, the modules are mounted on standardized aluminum support plates for easy handling and interim storage. For laser testing, a module is placed in an aluminum/plastic composite box which is equipped with a slide-in slot for quick insertion of the support plate. The box itself is mounted on a rigid aluminum pole and carries the electrical connectors for the readout system and the depletion voltage supply. Across from the module housing box, a motorized linear stage is mounted horizontally, itself carrying a second vertically oriented motorized stage, to which the laser optics are attached. By these means, the optics can be moved in a plane parallel to the module and illuminate any point on the silicon sensors. Both stages are driven by servo motors and offer a positioning accuracy of less than  $16\text{ }\mu\text{m}$ . The entire setup is housed in a lighttight cabinet and is mounted on an air-cushioned granite table to protect it from vibrations. Table 3.2 summarizes the components of the MTF and their properties.

### 3.4.3 The Test Procedure

A personal computer (PC) is deployed for controlling the course of a module test session with the MTF. It addresses the two linear stages, operates and monitors the high voltage power supply, and stores the silicon module data from the ARC board. The custom

<sup>4</sup>NIM – Nuclear Instrumentation Modules



**Fig. 3.10:** Photograph of the module test facility.

software package for the MTF is written in C++ and makes use of the ARCS hardware device driver and hybrid communication routine level, as well as a custom device driver for the linear stage controller board. Figure 3.11 illustrates the path followed by the laser spot in the plane of the module surface during the course of the fully automated testing procedure. In a first step, after insertion of the module into the MTF box, the depletion voltage for the module is slowly ramped up to 100 V to avoid high currents flowing into the capacitance of the growing depletion zones around the p-n junctions. The ramp time is set to 30 s. Subsequently, the laser spot is moved to a position away from the silicon sensor surfaces in order to take pedestal data without laser illumination.

The pedestal  $P_i$  of a sensitive detector element  $i$  is defined as its average output level if no signal is present. Due to manufacturing tolerances of the hybrid IC, the pedestals of the individual strips differ slightly from each other and must therefore be determined for



**Fig. 3.11:** Schematic view of the path which the laser spot follows during the test procedure in the plane of the module surface (solid blue line).

later subtraction from the signal data. For this purpose, the module is read out a certain amount of times  $n$  with the laser in the offside position and the resulting data  $D_{i,n}$  are stored for each strip  $i$ . The pedestals are then calculated according to

$$P_i = \frac{1}{n} \sum_{k=1}^n D_{i,k} . \quad (3.6)$$

controller	Intel P3 866 MHz personal computer
linear stages	OWIS Limes 90 (vertical) and Limes 120 (horizontal) DC servo stages with 150 mm and 200 mm travel, respectively, and $<16 \mu\text{m}$ positioning accuracy; OWIS DSC 1000 servo amplifier actuated by a Galil DMC 1040 motion controller for ISA bus
pulse generator	TTi TG550 function generator
laser source	Custom built single-mode diode laser unit, center wavelength $\lambda = 1050.5 \text{ nm}$ , with output power $< 1 \text{ mW}$ and 1 ns rise time
trigger unit	LeCroy model 222 gate generator
laser optics	Schäfter+Kirchhoff micro focus ( $f = 50 \text{ mm}$ ) mounted on a fiber collimator ( $f = 18.4 \text{ mm}$ ); 1.5 m long single-mode fiber with $7.5 \mu\text{m}$ core diameter; $8^\circ$ angled polish connectors
module readout	ARC system including ARC board, frontend adapters, ISA computer interface and cabling
depletion voltage supply	ISEG SHQ 222m power supply with RS 232 interface
software	Linux kernel 2.2.14 operating system, custom driver for linear stages, ARCS driver, custom software for module test operation

**Tab. 3.2:** Details of the components of the laser test facility.



In the case of the MTF, a value of  $n = 10000$  has been chosen to determine the pedestals with high accuracy.

Since at the beginning of a test session the state and position of the linear stages must be assumed to be unknown, an absolute position calibration is performed as the next step. For this, the two stages are moved towards the upper (vertical stage) or right (horizontal stage) boundary of their range, until they are stopped by their internal limit switches. This position is reproducible within the  $16\ \mu\text{m}$  accuracy of the servomotors and is then defined as the reference point by resetting the position encoders to zero.

After calibration, the MTF is ready for laser testing. The laser spot is moved successively over both sensors in a direction perpendicular to the strips at a constant speed of  $200\ \mu\text{m/s}$ . During the scans the individual strip signals are read out and stored with the APV25-S1 operated in peak mode. To allow checking the full strip length for possible defects, the sensors are scanned at the end far from the readout electronics. Scanning both sensors separately gives additional information about the identity of the sensor or wirebond which is affected by a particular defect. The channel numbering used in the following is indicated on the left side of Figure 3.11 and starts at zero. The laser moves along the direction of increasing strip numbers in both cases. The final output of the procedure is an array of 512 values for each scan – the set of the *maximum signal* delivered by each of the 512 strips. From these numbers, the corresponding pedestal values are subtracted. Including pedestal data collection and calibration of the linear stages, the total time needed for a test session with the MTF amounts to approximately 900 seconds per ring 6 module.

### 3.4.4 Investigation of Artificially Bonded Defects

To investigate the performance of the MTF and to assure its applicability for reliable detection of module defects, a *reference module* has been prepared with artificially bonded defects. Two pairs of short-circuited strips were simulated by placing a wirebond between the AC pads of the strip pair. Additionally, three pinholes resulted by wirebonding the AC and DC pads of a strip, thus establishing a perfect short-circuit between the surface aluminum and the underlying implant. The wirebonding was performed at the far end of sensor W6A, at maximum distance from the hybrid. Furthermore, one open wirebond between the sensor W6B and the pitch adapter appears on the reference module. Table 3.3 summarizes the artificial defects and gives the number of the affected strips on the module.

defect type	number	strip numbers
inter-strip short-circuits	2	269–270, 288–289
pinholes	3	309, 329, 349
open wirebond	1	411

**Tab. 3.3:** The type and number of artificially bonded defects on the reference module and the affected strip numbers.

Prior to the laser testing procedure, the pedestals and the CMN corrected noise of the reference module have been determined with the ARCS software [75]. Since the analog inputs of the APV25-S1 are bundled in four blocks of 32 channels each, the CMN correction algorithms implemented in ARCS are based on this group definition [77]. The results are depicted in Figure 3.12. The left part of the figure shows the strip pedestals, which exhibit a typical structure with sharp edges at the APV25-S1 borders and a slope within the range of the individual APV25-S1, which is probably due to a drop of supply voltage across the channels. No hint for any defective strip can be observed in these data.

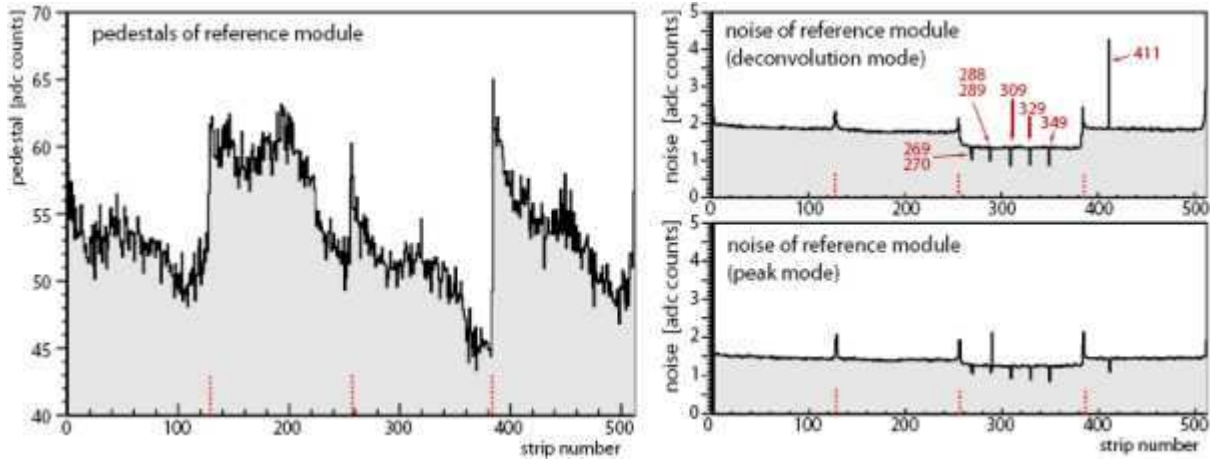


**Fig. 3.12:** The pedestals (*left*) and the common mode subtracted noise for the two APV25-S1 readout modes (*right*) for the MTF reference module. The APV25-S1 border channels are indicated by red dashed marks.

The right side of Figure 3.12 displays the noise of the strips of the reference module for the two APV25-S1 readout modes. In both cases, the noise data show a largely flat common baseline with a series of spikes of varying amplitude in both directions and a lower plateau in the strip range of one APV25-S1. The artificially bonded defects, indicated by the corresponding strip numbers, are clearly visible as distinct peaks or dips and can thus in principle be tagged as faults. However, a number of effects complicate the identification of defective strips in the noise data.

First, the channels on the APV25-S1 borders and especially the outermost strips close to the edge of the module show an increased noise level. This behavior is mostly due to their position which affects the capacitive couplings to their neighbors and other circuit paths on the module (e.g. to the guard or bias ring, see Figure 3.8). Despite the peculiarities shown by border and edge strips in the noise data, they are not to be considered as defective, thus making it necessary to distinguish them from the truly faulty channels. Furthermore, the signature of the different categories of defects is not unique in the noise data. Obviously, as apparent for example in the behavior of the pair of short-circuited strips 288–289 and the open wirebond (number 411), the signature varies with the readout mode, as the channels exhibit a lower or higher than average noise level in the two cases, respectively. The reason for this behavior lies in the CMN correction facility of the

APV25-S1, which applies also to channels with lower noise as for example those affected by an open wirebond. The correction may then lead to a higher apparent noise level, depending on the readout mode. In addition, the presence of multiple pinholes in the strip range of a single APV25-S1 leads to a significant lowering of the noise baseline due to an increased current flow between the silicon and the APV25-S1, which complicates the detection of defects. Finally, the signatures of defects in the noise data are highly sensitive to the environmental circumstances under which the module is operated, such as grounding and electromagnetic shielding, making them generally unpredictable and unreliable for testing purposes.

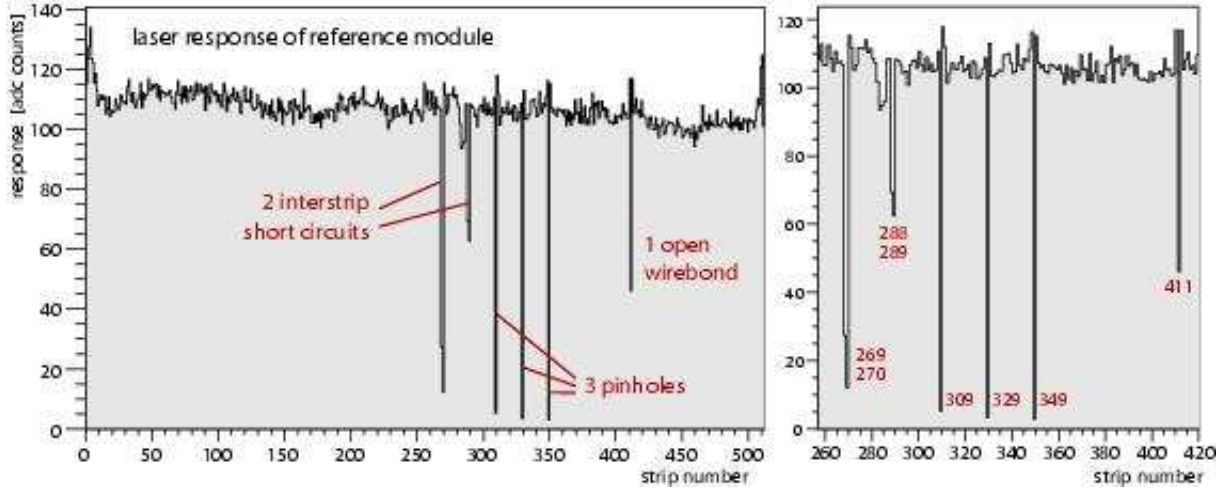


**Fig. 3.13:** Laser scan results from sensor W6A of the reference module (*left*); enlarged view of the strip interval exhibiting conspicuous strip signals from artificially bonded defects. The strip numbers are indicated (*right*).

Figure 3.13 displays the result of the laser testing procedure as it was applied to sensor W6A of the reference module. The overview histogram on the left side contains the maximum laser scan signal for each of the 512 channels; the right side shows an enlarged view of the strip range with bonded defects. As apparent in the overview, the normal channels show a nearly constant response to the laser illumination of about 110 adc counts. However, a slightly negative slope remains, which is caused by interference effects from light reflected at the metalized backplane of the sensors. Such effects are due to slight variations of the sensor thickness of the order of a few micrometers and have already been observed previously [84]. All artificially bonded defective channels clearly appear as distinct negative spikes from the common baseline and consistently show a lower response, independent of the readout mode. An indication for the type of defect can be obtained from the laser scan signature in the following way.

- Short-circuited strips are recognizable through their pairwise occurrence. Besides, since they are connected, the charge induced on one strip is shared among the two readout channels and leads to a reduced signal response for both. As a consequence of the increased strip capacitance at each channel input, the noise level is higher,

so that the resulting laser response of two particular pairs of short-circuited strips may significantly differ.

- Pinholes represent direct connections from the aluminum strips to the underlying  $p^+$  implants, permanently forcing the channel inputs of the affected strips to the implant potential. Therefore, no signal is observed at any time and the noise level is very small. Pinholes are thus identifiable through their particularly small response to laser illumination.
- Open wirebonds, similar to pinholes, prohibit the observation of any signal in response to laser illumination. However, due to the noisy behavior of the affected channels, resulting from the CMN correction described above, their mean observed response is typically higher than in the case of a pinhole.

It must be pointed out that, as a consequence of the statistical character of signal noise, the above criteria for identification of the type of defect must not be considered to be unambiguous in every case. The main purpose of the MTF is reliable defect detection. Figure 3.14 displays the distribution of the response for the channels of the reference module. The bulk of flawless strips show an approximately Gaussian distribution with a mean of 107 and a standard deviation of 4.3 adc counts. A small tail on the right side is caused by the slightly higher response of the module's edge strips. The region populated by the defective channels on the left side is clearly separated from the bulk by more than 8 standard deviations. Hence, all artificially bonded defects are reliably identifiable through their low response to laser illumination.

#### 3.4.5 Results from the TEC W6 Prototype Series

The TEC collaboration produced a prototype series – the *express-line 2* – of nine ring 6 modules. The main purpose of the express-line modules was to allow the development, improvement and validation of module test procedures prior to series production. Contrary

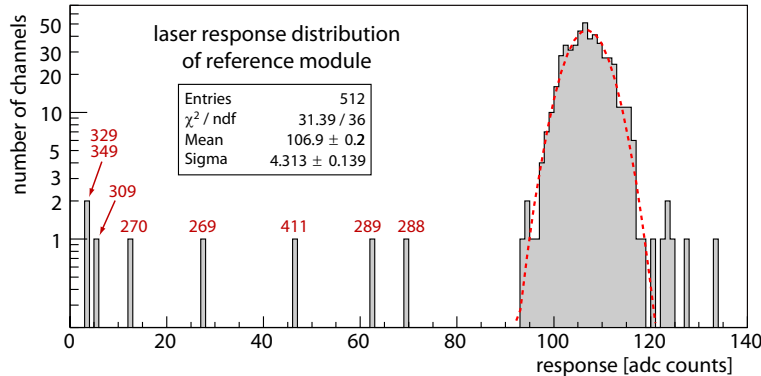


**Fig. 3.14:** Distribution of the laser response of the reference module channels. The red dashed line represents a Gaussian fit to the bulk of faultless strips, whose parameters are given in the legend. Defective channels are indicated by their strip numbers.

to the final module design, the express-line modules are equipped with ceramic hybrids instead of the kapton/copper ones, which, however, has no effect on their readout properties in this procedure. Individual modules are distinguishable through identification numbers on the support frame, which are listed in Table 3.4.

All nine modules of the express-line have been tested with the MTF according to the procedure described in § 3.4.3. The results of the individual scans of the W6A sensors are depicted in Figure 3.15. Confirming the earlier results on the reference module, defective strips are clearly visible through their strongly reduced response to laser light. Four of the modules turned out to have no faulty channels at all; their laser scan results are summarized in panel a) of the figure. Three of the remaining modules (M2, M3 and M6) have one defective channel each, while modules M4 and M7 each have two faulty channels. According to the grading scheme introduced in § 3.4, based on the number of defective strips, all modules must be considered as grade A. Nevertheless, modules M5, M6 and M7 were later classified as grade C due to their high leakage current [85].

module	frame id number	faulty channels
M1	30200020000501	–
M2	30200020000502	17 <sup>b</sup>
M3	30200020000641	242 <sup>b</sup>
M4	30200020000643	447 <sup>p</sup> , 509 <sup>p</sup>
M5	30200020000503	–
M6	30200020000644	357 <sup>p</sup>
M7	30200020000640	77 <sup>p</sup> , 89 <sup>b</sup>
M8	30200020000642	–
M9	30200020000645	–

**Tab. 3.4:** The results of the express-line module tests with the MTF. Faulty channels are indicated by the type of defect: <sup>p</sup> for a pinhole and <sup>b</sup> for an open wirebond.

Table 3.4 gives an overview of the modules and the defective channels detected. From the seven defects listed, two have been identified as open wirebonds by visual inspection, and four represent pinholes. The failure of channel 242 on M3 is probably due to a broken pitch adapter line [85]. No short-circuited strips were observed. The results of the express-line module tests with the MTF turn out to be consistent with those from other facilities using different testing techniques [77].

Following the express-line module tests the MTF is established as a practicable and reliable facility for the detection of defective strips on the TEC modules. Furthermore, with its high positioning accuracy and stability of the laser intensity, the MTF is well suited as a precision tool for the in-depth investigation of silicon microstrip sensor properties. However, the disadvantage of the facility are the high costs of the hardware. In order to provide all laboratories involved in module testing with identical test facilities, the decision was made to use an extension to the ARC system [75] for testing during the series production of the modules. Besides test procedures based on measurements of the sensor leakage current, APV25-S1 amplifier gain linearity, noise distributions and fron-

tend electronics performance, the extended ARC can perform illumination of the silicon sensors with light-emitting diodes.

The assembly of the CMS Tracker Endcaps was finished in November 2006 and first operation of the LHC is scheduled for 2007. The following chapters describe the search for signatures of supersymmetry in the cosmic ray spectra and the analysis of data from the AMS-01 experiment, which bases on the reconstruction of multi-particle events in a large-scale application of a silicon microstrip detector which was operated in space. The subject is introduced with a discussion of cosmic rays in the next chapter.



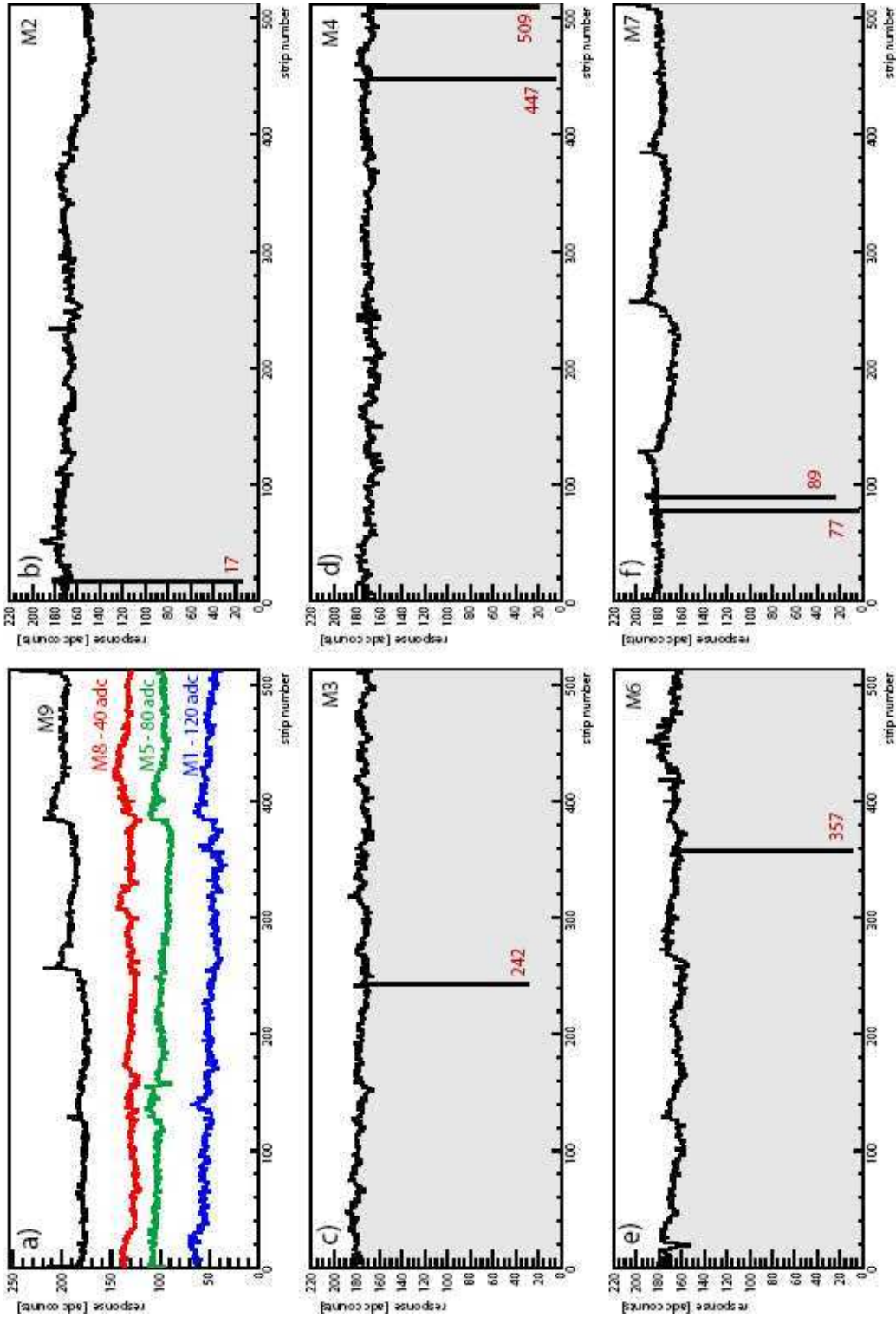


**Fig. 3.15:** Laser scan results from W6A sensors of the express-line modules. Display a) combines the scans of the four modules without defects M1, M5, M8 and M9. For the sake of clarity, the common baselines of the channels have been shifted downward by 120, 80, 40 or 0 adc counts, respectively. The remaining histograms b) to f) show the individual results for modules M2, M3, M4, M6 and M7, with the defective strips indicated by their strip numbers.



## 4 Cosmic Rays as Tracers of Dark Matter

The Earth is continuously exposed to a flux of particles of extraterrestrial origin, referred to as cosmic rays. This was discovered in 1912 by V. Hess, who observed an increasing discharge rate of electrometers towards higher altitude during a series of balloon flights [86]. Historically, the investigation of cosmic rays has played an important role in the development of particle physics, as they were the only source of high energy particles before the emergence of accelerators. Thus, the positron [87], the muon [88], the pion [89], the kaon [90] and other strange mesons have been discovered in cosmic rays.

Experimental knowledge about cosmic rays spans a very wide energy range. Particles from the solar wind typically propagate with a few keV, while, on the other hand, cosmic rays have been observed with energies higher than  $10^{20}$  eV [94]. Moreover, the abundance of cosmic rays strongly varies as a function of energy. Over large energy intervals the spectra follow a steep power law with a spectral index of roughly 3, meaning that the intensity of cosmic rays decreases by a factor of 1000 for each decade in energy [95].

Regarding the search for dark matter, one of the most important properties of the spectral shapes of cosmic rays is their smoothness on small scales. As will be shown in this chapter, the cosmic ray background produced in conventional high energy processes

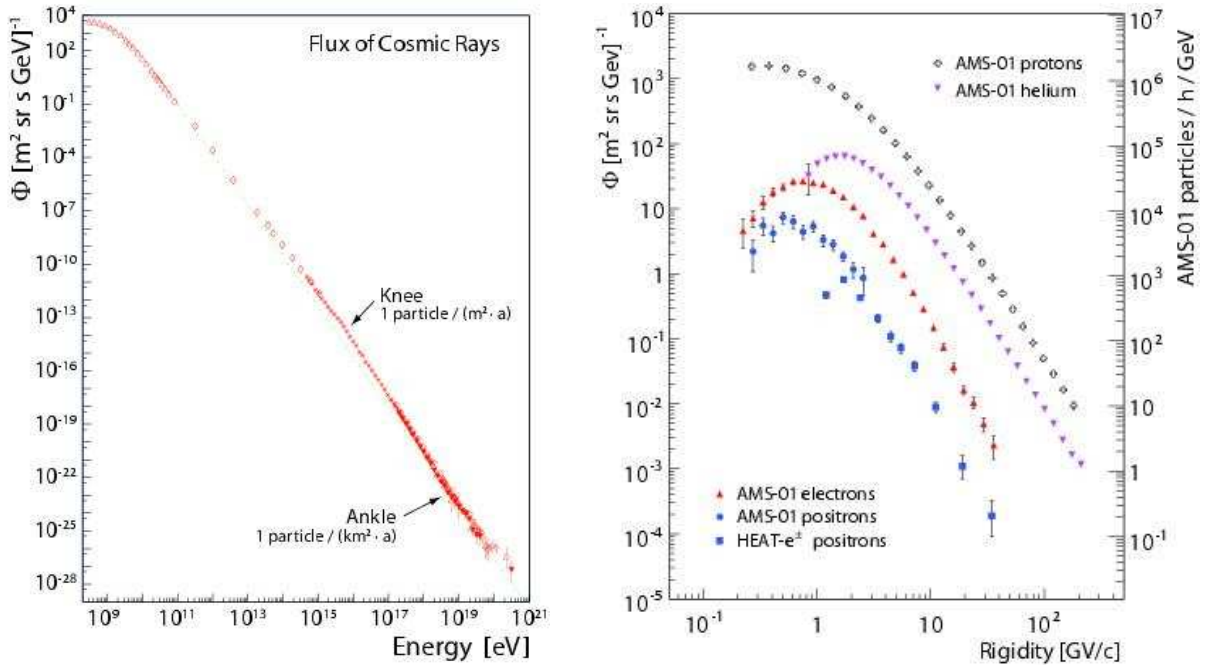


**Fig. 4.1:** Total cosmic ray flux as a function of energy [91] (left); fluxes of some of the most abundant cosmic ray components as measured by AMS-01 [2, 92, 93] and HEAT- $e^\pm$  [3] (right).

in the universe is expected to lack any structure. Reaction chains involving dark matter may be additional sources of standard model particles and would cause an excess within limited energy ranges. Of particular interest are the fluxes cosmic ray particles of low abundance, such as the positron, since exotic sources would lead to significant excesses.

## 4.1 Cosmic Ray Composition and Spectra

The particles reaching the top of the Earth’s atmosphere are mainly electrons and fully ionized light atomic nuclei, such as hydrogen and helium. Nuclei with higher charge and other particles amount to less than 1 % of the total intensity. Table 4.1 gives an overview of the approximate abundance of the most dominant cosmic ray components at 1 GeV energy. Antinuclei have not been observed yet [96]. The chemical composition of cosmic rays is similar to that of the sun, which indicates that they are predominantly of stellar origin. Exceptions are the nuclei of elements from Li to B and from Sc to Mn, which are overabundant as the products of spallation of carbon and oxygen and of iron, respectively.

Component	Abundance [%]	Component	Abundance [%]
Hydrogen	90	Positrons	0.4
Helium	4.6	Carbon	0.2
Electrons	2.3	Oxygen	0.2
Deuterons	1.7	Other nuclei	0.3

**Tab. 4.1:** Approximate abundances of the most dominant components of cosmic rays at 1 GeV (or 1 GeV/nucleon for nuclei) energy, in percent of the total intensity. Based on data from [2, 46, 92, 93, 97, 98].

Due to the deflection of charged particles in the galactic and solar magnetic fields, the arrival directions of cosmic rays are randomized at detection, so that the fluxes are widely isotropic. Their energy spectra above 10 GeV can be described by a segmented power law of the form

$$\frac{dN}{dE} \propto E^{-\gamma}, \quad (4.1)$$

with the *spectral index*  $\gamma$  as an essential parameter. Up to energies of  $10^{16}$  eV  $\gamma$  is equal to 2.7 and then steepens to 3.0 for higher energies (see Figure 4.1, *left*). The break in the spectra at  $10^{16}$  eV is commonly referred to as the *knee*. At approximately  $10^{19}$  eV – the *ankle* – and above, the spectra seem to flatten again. This behavior is independent of the incident direction, i.e. the spectral shapes are also isotropic. Below 10 GeV, the spectra are modulated by the solar and geomagnetic influence, which is the subject of § 4.3.

The reason for the two breaks in the spectra has not been fully understood as yet [95]. The conventional explanation is that they represent the power limits of different acceleration mechanisms at successive energy scales. Obviously, these mechanisms must be based on a common principle, since the spectral shape is universal over large energy ranges. It was proposed in 1949 by E. Fermi [99], that the spectral shape may originate from

repeated finite energy gains of particles in collisions with moving objects, e.g. magnetic fields in shock waves of supernovae. Let a particle of initial energy  $E_0$  undergo such a repeated acceleration and gain a fraction  $\xi E$  of its energy  $E$  each time. Then, after  $n$  collisions, it will have

$$E_n = E_0 (1 + \xi)^n, \quad (4.2)$$

giving for  $n$

$$n = \ln(E/E_0) / \ln(1 + \xi). \quad (4.3)$$

Assuming a probability  $p_w$  for a particle to escape the acceleration mechanism, the number of particles with an energy larger than  $E$  is

$$N(\geq E) \propto \sum_{m=n}^{\infty} (1 - p_w)^m = \frac{(1 - p_w)^n}{p_w}. \quad (4.4)$$

Substituting  $n$  from eq. 4.3 yields

$$N(\geq E) \propto \frac{1}{p_w} \left( \frac{E}{E_0} \right)^{-\alpha}, \quad \alpha \approx p_w / \xi, \quad (4.5)$$

which leads to the observed form of the spectra [100]. This is the principle on which the so called *second order Fermi acceleration mechanism* is based. However, in this simple form, it cannot sufficiently explain the isotropy of the observed spectra. Furthermore, it requires large initial energies and is very inefficient, so that cosmic rays of highest energy are unlikely to have been accelerated in this way. Consequently, Fermi's theory has undergone fundamental further development in the past decades [101].

Figure 4.1 (*right*) shows the spectra of protons, helium nuclei, electrons and positrons with energies up to approximately 100 GeV. It is apparent that in this energy regime protons are by far the most abundant cosmic ray component. In particular, their flux exceeds that of positrons by a factor of  $10^3 - 10^4$ . The ratio of the positron to electron flux varies from roughly 1:7 to 1:20. Moreover, the energy spectra of the leptons ( $\gamma \approx 3.4$ ) are slightly steeper than those of nuclei ( $\gamma \approx 2.7$ ).

## 4.2 Origin and Propagation of Cosmic Rays

Cosmic rays can be classified in two main categories of different origin, *solar* and *galactic* cosmic rays. As obvious from these terms, solar cosmic rays have their origin and are accelerated in the vicinity of the sun, while galactic cosmic rays are produced somewhere in the galactic volume. However, it is often assumed that cosmic rays of highest energies may even originate from extragalactic sources. On their way to Earth, cosmic ray particles are involved in a plenitude of processes, including elastic and inelastic scattering off the interstellar medium, deflection by magnetic fields and deceleration through emission of radiation.

Solar cosmic rays mostly consist of ionized coronal material which is accelerated by shock waves associated with the solar wind [102]. The abundance of these particles decreases steeply with energy. At low energies, below 100 MeV, they constitute the major

part of the observable cosmic ray flux, but in the GeV energy range their persistent contribution is negligible. Only in the rare case of intense solar flares may particles be accelerated up to 1 GeV or even more [103]. These events have typical durations of the order of minutes or hours. The composition of cosmic rays produced in solar flares is quite similar to that of galactic cosmic rays [104].

Supernovae provide the dominant power input to the galaxy. An average supernova explosion releases between 1 and 10 solar masses of material and a total energy of  $10^{44}$  J. Taking into account a supernova explosion frequency in the galaxy of roughly  $3 \times 10^4 \text{ Ma}^{-1}$ , it follows that each supernova would only have to contribute  $\sim 3\%$  of its output power to the total cosmic ray power<sup>1</sup> of  $10^{34}$  W [104]. For this reason supernovae are believed to be the dominant accelerators of cosmic rays to energies up to  $10^{16}$  eV. Since particles are scattered by interstellar gas and therefore their energy declines inversely with the cube root of the number density, they cannot be accelerated too soon after the explosion. Rather than that, the acceleration takes place when the interstellar gas is passed by the shock waves emerging from the supernova. Evidence comes from observations of supernova remnants in the keV X-ray band [105], yielding a flat spectrum which can be interpreted in terms of bremsstrahlung emission from protons or electrons. Furthermore, recent results from imaging atmospheric Čerenkov telescopes reveal that these remnants also emit gamma rays with up to TeV energies [106], in agreement with the X-ray measurements regarding the spatial location of the sources. Besides supernovae, other candidates for sources of cosmic rays are pulsars, close binary systems and stellar winds [107]. Particles which are produced and accelerated in the vicinity of these sources are, with respect to their origin, commonly referred to as *primary cosmic rays*.

Between its acceleration and its detection a galactic cosmic ray particle traverses an average amount of interstellar matter of  $10 \text{ g cm}^{-2}$  [108] within typically 20 Ma of time [109]. The propagation volume is permeated by the galactic magnetic field, whose regular (large scale) component has a strength in the order of  $5 \mu\text{G}$  [110], however with turbulent local variations. As a consequence, in addition to their convective thermodynamic motion, charged particles diffuse due to interactions with the magnetic field inhomogeneities. While propagating through the galaxy, cosmic rays also lose energy. For nuclei, the dominant energy loss processes are ionization in the interstellar medium and scattering off thermal electrons in plasmas [109]. Electrons and positrons additionally undergo bremsstrahlung, synchrotron radiation and inverse Compton scattering with starlight or with the cosmic microwave background [111]. Assuming the presence of a galactic wind, i.e. a constant flow of magnetic irregularities, particles may also gain energy while propagating from shock acceleration (*diffuse reacceleration*).

The destruction of primary nuclei via spallation in the interstellar medium gives rise to secondary nuclei and rare isotopes. Photons and antiparticles are also rare in cosmic rays. Apparently, they are not directly produced in the cosmic ray sources, but emerge as secondary products from processes involving primary cosmic rays, and are thus called *secondary cosmic rays* (see Figure 4.2, *left*). Antiprotons largely stem from proton-proton, proton-nucleus and nucleus-nucleus interactions [112]. Photons are decay products of neutral pions from such processes and also result from synchrotron radiation of high

---

<sup>1</sup>i.e. the estimated total power leaving the galactic disk in form of cosmic rays



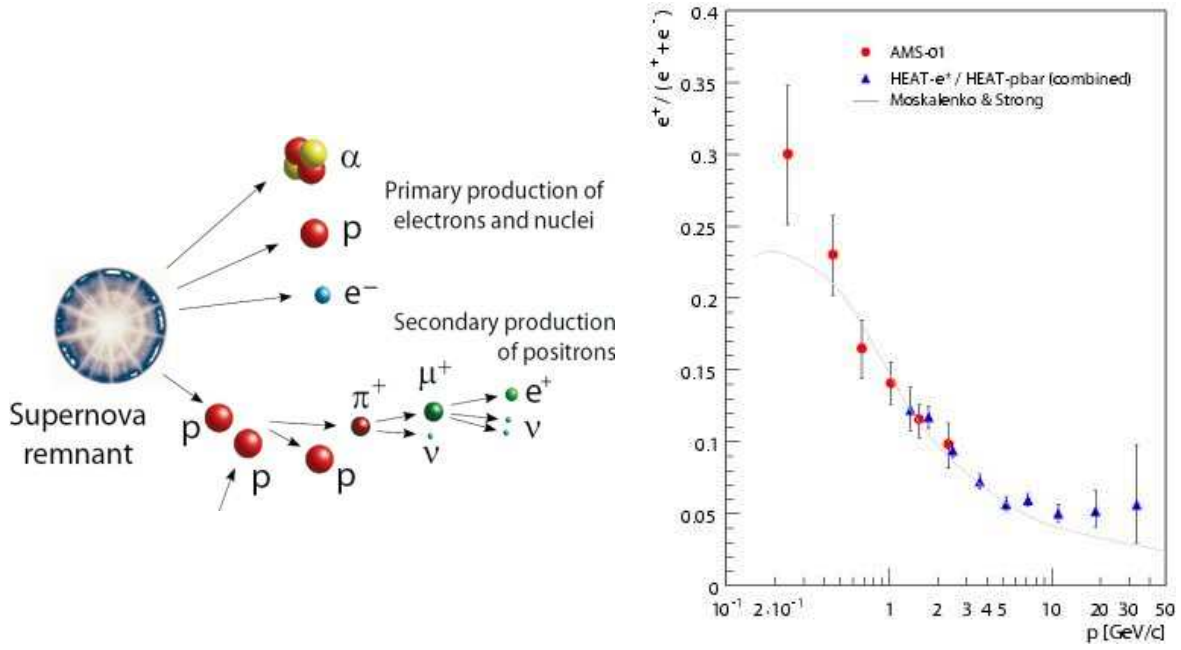


**Fig. 4.2:** Principle of primary and secondary cosmic ray production (*left*); model calculation of the positron fraction  $e^+/(e^+ + e^-)$  for purely secondary positron production from [111] (solid line) together with recent data from AMS-01 [2], HEAT- $e^\pm$  and HEAT-pbar [7] (*right*).

energetic particles or inverse Compton scattering. Positrons are mainly created by protons in reactions of the type  $pp \rightarrow \pi^+ + X$  or  $pp \rightarrow K^+ + X$ , where the pions and kaons decay into positrons via muons. Furthermore, the  $\gamma e^+ e^-$  decay channel of neutral pions from reactions of the type  $pp \rightarrow \pi^0 + X$  contributes to the positron flux. In addition to protons, light nuclei may also be involved in these interactions [113].

The cross sections of the processes which contribute to the positron flux are strongly energy dependent and the spectra of their individual contributions are smeared by energy losses during particle propagation. The ratio of the positron and electron fluxes, commonly written in terms of the *positron fraction*  $e^+/(e^+ + e^-)$ , is thus a smooth function of momentum. Figure 4.2 (*right*) shows a model calculation of the positron fraction for purely secondary positron production (without reacceleration) together with recent experimental data. In the range from a few hundred MeV/c to 50 GeV/c it decreases monotonously from 0.2 to roughly 0.03 and then flattens out. In particular, for purely secondary positron production, the positron fraction does not exhibit any small scale features, peaks or dips.

## 4.3 Cosmic Rays in the Earth's Vicinity

Within the heliosphere, cosmic rays are influenced by the solar wind, a continuous stream of charged particles emanating from the sun. The magnetic field associated with this stream has irregularities which scatter particles in a frame of reference moving outwards of the solar system. As a result, cosmic rays are effectively decelerated (or even deflected) in the vicinity of the sun, an effect which is referred to as *solar modulation*. According

to the so called force field approximation [114], the influence of solar modulation can be parameterized with a single parameter  $\phi$ , which represents an effective potential and is given in units of volts. Thus a particle with charge  $Ze$  experiences an energy loss  $Ze\phi$  when approaching the Earth from outside the heliosphere. As displayed in Figure 4.3, the solar modulation parameter is time dependent and follows the 11 year solar cycle, typically varying from 300 MV to 1300 MV. As can be seen e.g. in Figure 4.1 (*right*), the solar modulation is apparent as a decrease with respect to the power law expectation of the cosmic ray fluxes below approximately 10 GeV. There is evidence that solar modulation is charge sign dependent at low particle energies [115].

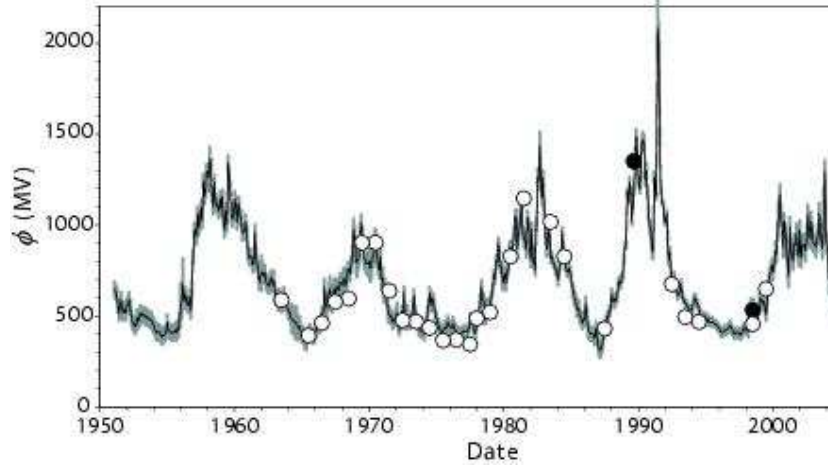


**Fig. 4.3:** The solar modulation parameter  $\phi$  (solid line) with 68 % confidence intervals (grey area) as a function of time [116]. The circles denote reference data.

Immersed in the heliospheric particle streams is the magnetosphere of the Earth. The rather complex magnetic field generated by the Earth's body (*internal field*) is commonly treated as the derivative of a scalar potential,  $\mathbf{B} = -\text{grad } V$ , with  $V$  expanded in terms of spherical harmonics,

$$V = a \sum_{n=1}^{\infty} \sum_{m=0}^n (g_n^m \cos m\phi + h_n^m \sin m\phi) \left(\frac{a}{r}\right)^{n+1} P_n^m(\cos \theta) . \quad (4.6)$$

Here,  $a$  is the mean radius of the Earth,  $(r, \phi, \theta)$  are geocentric coordinates,  $P_n^m(\cos \theta)$  are the associated Legendre functions, and  $(g_n^m, h_n^m)$  are the Gauss coefficients describing the field contribution of the separate terms in the sum [117]. Additional terms may also incorporate external magnetic field sources, such as particle streams generated by interactions with the solar wind. The dominant terms in eq. (4.6) are related to  $n = 1$ , i.e. the geomagnetic field is in first order that of a dipole, tilted by about  $168.5^\circ$  with respect to the rotation axis of the Earth<sup>2</sup> and displaced approximately 400 km from its center. The field strength on the Earth's surface varies between  $20 \mu\text{T}$  and  $70 \mu\text{T}$ . As shown in Figure 4.4 (*left*), at distances of a few Earth radii, the geomagnetic field is

<sup>2</sup>The geomagnetic north pole lies in the southern geographic hemisphere.

distorted by the solar wind, a highly dynamic process which gives rise to a shock front (*bow shock*) along the border between interplanetary magnetic fields and the Earth's magnetosphere (*magnetopause*).

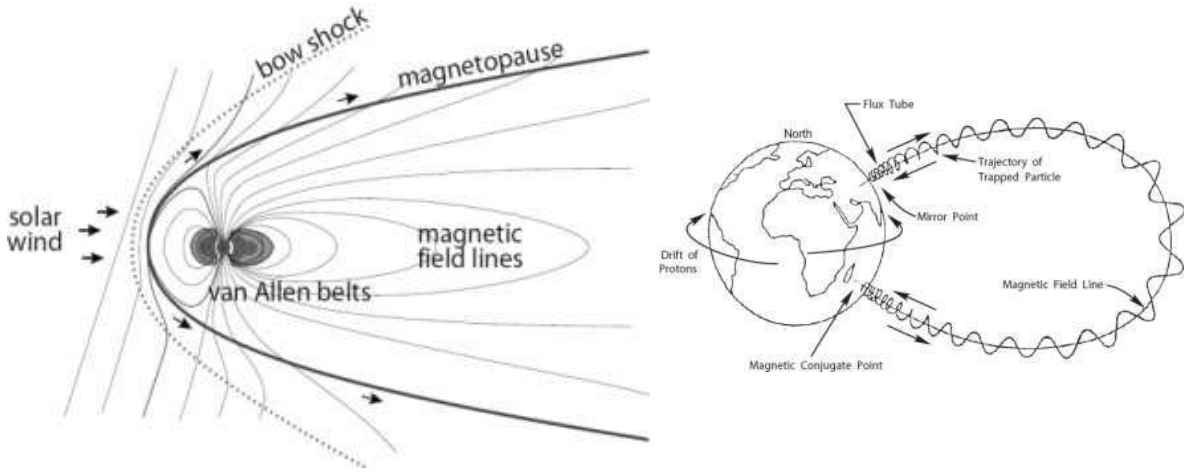


**Fig. 4.4:** Schematic view of the Earth's magnetosphere and the van Allen belts, as distorted by the solar wind (*left*); trajectory of a charged particle in the geomagnetic field (*right*) [118].

Low energy charged particles can be trapped in the geomagnetic field. The path which such a particle travels is schematically illustrated in Figure 4.4 (*right*). The basic trajectory is a helix following the field lines, with an increasing radius of curvature of its gyromotion (*gyroradius*) as the particle moves further away from the Earth. Near the Earth's surface, where the field strength is larger, the gyroradius decreases. The particle's energy then becomes dominated by the gyromotion contribution at the expense of the forward motion along the field line. Consequently, the particle is deflected back along its path, only to repeat the process at the other end. As the trapped particle bounces back and forth along the magnetic field, it also drifts around the Earth because, in part, its gyroradius is larger on the outer part of its trajectory than on the inner part. This effect causes negatively charged particles to drift in the direction of the Earth's rotation (eastward) and positively charged ones to drift in the opposite direction [118].

It follows that, in the dipole approximation, the region which can be occupied by trapped particles forms a nearly toroid-shaped volume symmetrical about the dipole axis. The *Van Allen radiation belts* surround the Earth at a distance of roughly 1.5 and 4-5 Earth radii from its center [119]. While the inner belt mostly consists of protons with energies larger than 100 MeV and is relatively stable, the outer belt is largely populated with electrons ranging in energy from 400 keV to above 15 MeV, and dynamically deformed by the solar wind. Protons from the inner belt can interact with atmospheric molecules, giving rise to secondary particles (*atmospheric secondaries*) such as, amongst others, positrons.

The ability of a cosmic ray particle to penetrate the Earth's magnetosphere is uniquely determined by its *rigidity*, the momentum divided by the charge, given in units of volts. Cosmic ray particles with rigidities below a certain *geomagnetic cutoff* are deflected by the geomagnetic field and cannot reach the vicinity of the Earth. The value of this cutoff

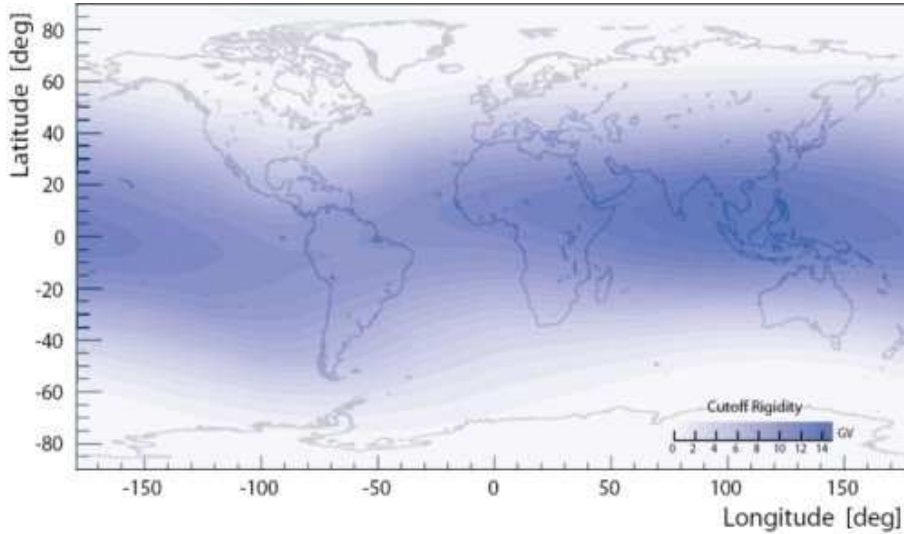


**Fig. 4.5:** The vertical cutoff rigidity at an altitude of 450 km under magnetically quiet conditions. Based on data from [120].

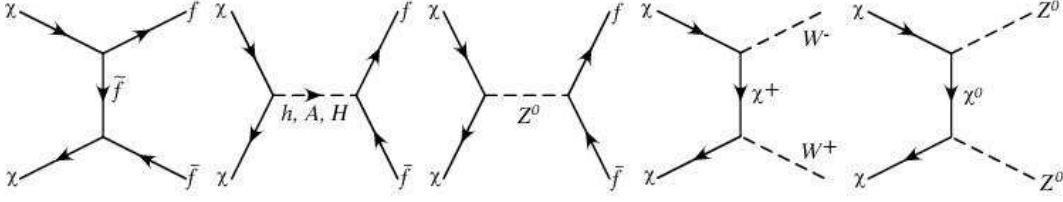
not only depends on the geomagnetic coordinates of the particle's entry point into the magnetosphere, but also on its incident direction.

Figure 4.5 shows the cutoff rigidity for vertical incidence at an altitude of 450 km above the Earth's surface under magnetically quiet conditions [120]. It ranges from a few MV in the polar regions up to approximately 15 GV near the equator. Similar to the solar modulation effect, the geomagnetic cutoff modulates the spectra of cosmic rays having rigidities in this range. Particles detected in an experiment with rigidities below their cutoff cannot be of galactic origin, but must stem from within the magnetosphere. They are mostly produced as atmospheric secondaries and are trapped in the Earth's radiation belts.

## 4.4 Signatures of SUSY Dark Matter in the Cosmic Ray Spectra

As stated already in sec. 2.4, neutralinos as Majorana particles could annihilate pairwise into SM particles, which then propagate as cosmic rays and are thus accessible to experiments. This process would constitute an additional primary source of cosmic rays with a unique spectral shape, and may thus appear as an excess of particles over conventional expectations. However, since the corresponding source strength is assumed to be small compared to that of supernovae, the dark matter annihilation signal should be sufficiently significant only in the spectra of cosmic ray particles which are exclusively produced through secondary processes at low rates, such as positrons, antiprotons or gamma rays (see § 4.2).

Figure 4.6 shows the Feynman diagrams for the dominant neutralino annihilation channels. The process can proceed through the t-channel exchange of sfermions, charginos or



**Fig. 4.6:** The dominant annihilation channels for the lightest neutralino  $\chi$  [47].

neutralinos, or through s-channel annihilation via  $Z^0$  or pseudoscalar Higgs bosons. The final states are either fermions or gauge bosons. The total cross section for neutralino annihilation strongly depends on the individual channel amplitudes, and thus on the choice of supersymmetric parameters. For example, in the case of fermion final state diagrams, the amplitude is proportional to the fermion mass in the low velocity limit and inversely proportional to the squared mass of the sfermion  $\tilde{f}$ . Furthermore, the amplitude for Higgs exchange is proportional to  $\tan\beta$  for down-type quarks [47]. This implies that at values of  $\tan\beta \gtrsim 5$  neutralino annihilation is dominated by s-channel Higgs exchange with  $b\bar{b}$  pairs as the final state.

Subsequent to their generation,  $b$ -quarks hadronize and give rise to decay cascades in which, amongst others, positrons and antiprotons are produced, as well as typically 30–40 photons per annihilation [122]. Additional positrons originate from the decay of gauge bosons and of  $\tau$  and  $\mu$ . Direct annihilation into electron positron pairs is helicity suppressed [43]. As an example, Figure 4.7 (*left*) shows the raw spectra of positrons (prior to their propagation through the interstellar medium) from the different annihilation modes of neutralinos with a mass of  $300 \text{ GeV}/c^2$ . The spectral shapes differ significantly,

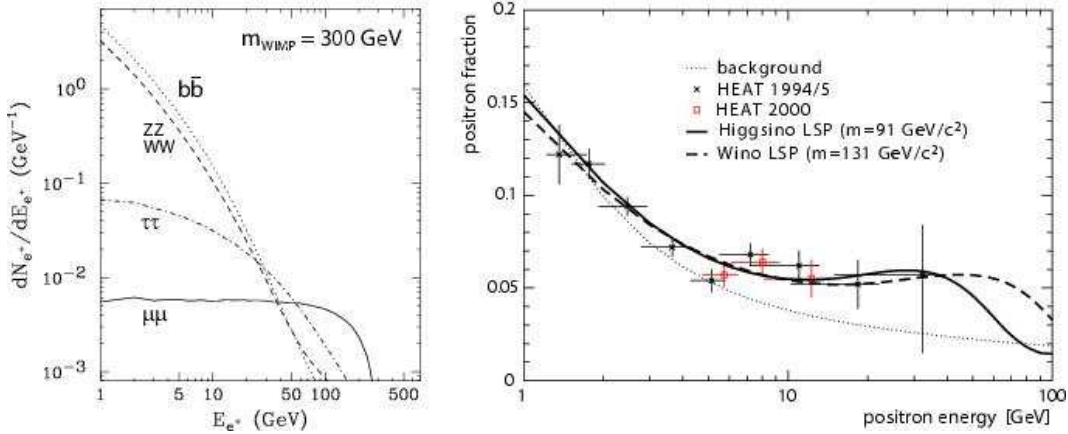


**Fig. 4.7:** The positron spectrum from neutralino annihilations, prior to propagation, for selected annihilation modes and a neutralino mass of  $300 \text{ GeV}/c^2$  [42] (*left*); positron fraction data and simulation results for purely secondary positron production (background) and with additional positrons from neutralino annihilation for two mSUGRA parameter sets, resulting in either a higgsino- or wino-like neutralino [121] (*right*).



since annihilations to heavy quarks and gauge bosons produce a much softer spectrum than the  $\tau$  or  $\mu$  channels. The shape of the overall resulting spectrum is a mixture of the above and is determined by the cross section of the individual modes, which depend on the supersymmetric parameters. The positrons then propagate through the galactic volume and experience energy loss and deflection due to scattering and interactions with magnetic fields, which finally result in a smearing of the initial raw spectrum when observed near Earth.

Quark hadronization functions and branching ratios of the decay modes involved in positron production from neutralino annihilations are known to a high degree of precision [32]. Using models of particle propagation in the interstellar medium, the spectra of secondary particles near Earth can be simulated and compared to flux measurements. Figure 4.7 (*right*) displays the positron fraction as a function of the particle energy together with data from HEAT- $e^\pm$  [3] and HEAT-pbar [123]. When compared to the background expectation, the data show an indication for an excess number of positrons at energies above 6 GeV. The solid and dashed lines represent simulations of the positron fraction including contributions from neutralino annihilation for two particular sets of supersymmetric parameters [121]. The spectral shape differs mainly due to the choice of neutralino mass. In the one case, the neutralino with a mass of  $91 \text{ GeV}/c^2$  is *Higgsino-like*, meaning that in the linear combination of eq. (2.7) the coefficients  $c_{31}$  and  $c_{41}$  are large compared to the bino and wino contributions. In the other scenario, the  $131 \text{ GeV}/c^2$  neutralino is *wino-like* with a dominant contribution from  $c_{21}$ . In contrast to the *bino-like* neutralino, which largely annihilates to heavy fermions, gauge boson final states are preferred in the two cases above [42].

Both results involving dark matter annihilation clearly improve the agreement with the data compared to the background-only prediction. Clearly, in order to further constrain

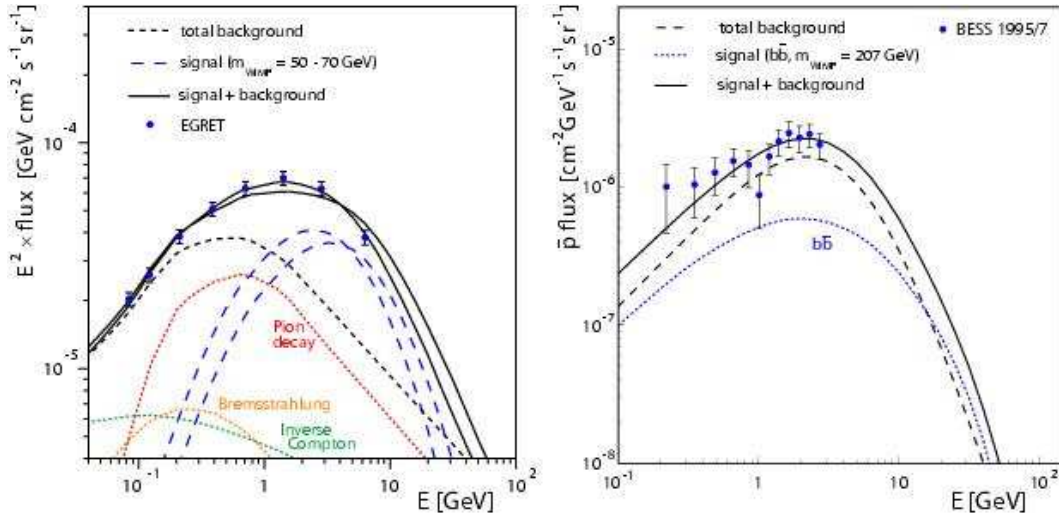


**Fig. 4.8:** Data of the diffuse gamma ray energy spectrum fitted with the simulated background from different processes and an annihilation signal from a  $50\text{--}70 \text{ GeV}/c^2$  neutralino (*left*) [47]; same for antiprotons with an assumed neutralino mass of  $207 \text{ GeV}/c^2$  (*right*) [124].



the mass range of the neutralino, better data is needed, especially at higher energies in order to capture the trailing edge of the dark matter signal. The simulated positron flux resulting from annihilation is almost always too small to produce a visible signal. However, it may be increased by a *boost factor*  $B$ , which can be explained by assuming a clumpy nature of the dark matter distribution. In particular, since the neutralino annihilation rate is proportional to the square of its density, a signal enhancement is expected in high density regions like the center of the Galaxy. The boost factor is thus proportional to the mean deviation of the squared density  $\rho$ ,  $B \propto \langle \rho^2 \rangle / \langle \rho \rangle^2$ .

Figure 4.8 shows the simulated background spectra of gamma rays and antiprotons compared to experimental results. In both cases the background alone turns out to be inconsistent with the measured fluxes, so that an additional source of particles is assumed to fit the data. In the gamma ray spectrum on the left side of Figure 4.8, a signal from the annihilation of neutralinos with masses of 50–70 GeV/c<sup>2</sup> is found to explain the observed excess well [47]. The right side of Figure 4.8 shows the measured spectrum of antiprotons, which can again be fitted with the assumption of neutralino annihilation, however with a significantly different neutralino mass of 207 GeV/c<sup>2</sup> [124].

Despite the hints for the presence of a dark matter signal in the spectra of secondary particles, the neutralino hypothesis remains controversial. It has been pointed out recently that the excess of gamma rays, if explained as a signal of neutralino annihilation as shown in Figure 4.8 (*left*), may not be compatible with the observed abundance of antiprotons [125]. Other possible contributions to the cosmic ray positron flux have been proposed, such as electron-positron pairs from annihilations of hypothetical Kaluza-Klein particle states [42], or from conversion of synchrotron photons emitted by galactic pulsars [126]. Consequently, more data is necessary to allow further development of these models. While new experiments are yet under construction, one possible approach is the reanalysis of data from past experiments such as AMS-01 with new techniques. The description of the AMS-01 detector is subject of the next chapter.



## 5 The AMS-01 Experiment

### 5.1 AMS-01 Detector Construction

As a prototype for the AMS-02 experiment, the AMS-01 detector was flown on board the space shuttle *Discovery* in a near Earth orbit during the *STS-91* mission from June 2nd to 12th, 1998. Its main purpose was to verify the feasibility of engineering a space borne high-energy particle detector, launching it into orbit, and operating it safely under space environment conditions. Furthermore, the main design principles of the future AMS-02 experiment were tested. During its flight, AMS-01 has recorded a large amount of data for the determination of particle fluxes in the Earth's vicinity, leading to precise proton [6, 92] and helium [93] flux spectra, measurements of the characteristics of leptons in near earth orbit [2], and to a significant improvement of the upper limit on the relative flux of antihelium to helium [96] in cosmic rays.

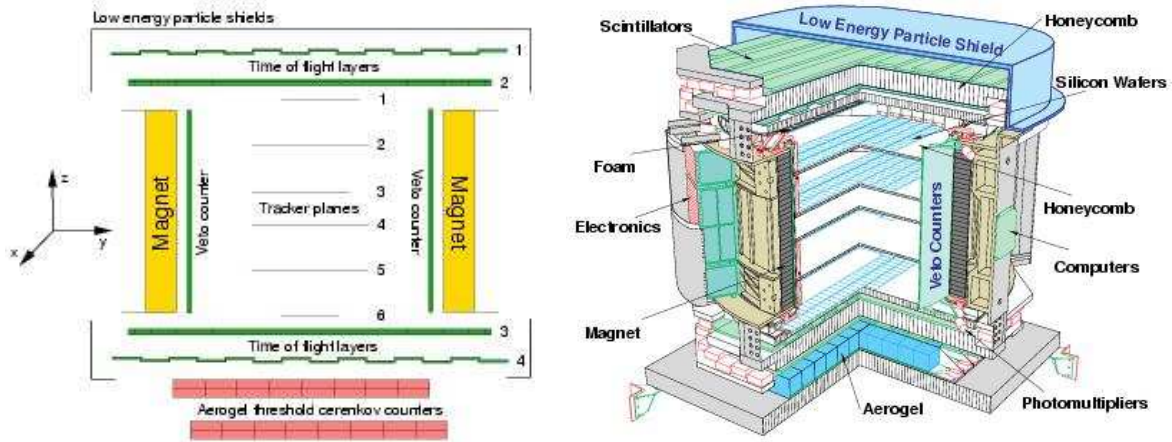


**Fig. 5.1:** The AMS-01 detector: schematic cross section in the y-z plane (*left*) and three dimensional illustration (*right*).

The structure of AMS-01 is illustrated in Figure 5.1. Six layers of double sided silicon strip sensors enclosed in a cylindrical permanent magnet formed the experiment's tracking chamber. The particle flight direction and velocity was measured with plastic scintillator paddles arranged in two double planes, one above and one below the magnet (time of flight hodoscopes, TOF). Additionally, the inner surface of the magnet was covered with scintillators to reject background from particles which traverse the magnet wall or the support structure (anticoincidence or veto counters). As a complement to the velocity measurement with the hodoscopes, two layers of threshold Čerenkov counters were situated at the lower end of the detector. In order to keep very low energy particles (up to several MeV) from entering, AMS-01 was shielded by thin carbon fiber

walls with a thickness of 10 mm above or 6 mm underneath the experiment (low energy particle shield, LEPS). The top shielding was covered with a blanket of Beta cloth<sup>1</sup> and a Nomex/Aluminum/Mylar composite with a thickness of approximately 1.7 mm. By these means AMS-01 was protected against mechanical damage and excessive warming from exposure to direct sunlight.

Figure 5.1 (*left*) shows the definition of the AMS-01 coordinate system. Its origin lies in the center of the magnet bore. The z-axis is perpendicular to the tracker and TOF planes and points upward, with the Čerenkov counter at negative values of z. The x-axis points into the direction of the magnetic field's dominant component<sup>2</sup>.

### 5.1.1 The Magnet

A permanent magnet with a nominal bending power of  $BL^2 = 0.14 \text{ Tm}^2$  was chosen for AMS-01 because of its compact and rigid structure and the low amount of maintenance and operating expenses. The magnet had a cylindrical shape with an inner radius of 558 mm, 95 mm wall thickness and a length of 800 mm along its cylinder axis, resulting in a free area of  $0.98 \text{ m}^2$  and a geometrical acceptance of  $0.82 \text{ m}^2\text{sr}$ . It consisted of 6400 blocks of Nd-Fe-B alloy, sized  $2 \times 2 \times 1$  inches each, arranged in 64 sectors. The blocks were magnetized in such a way that the resulting dipole field was to first order perpendicular to the longitudinal axis (z-axis) and parallel to the positive x-axis as shown in Figure 5.2.

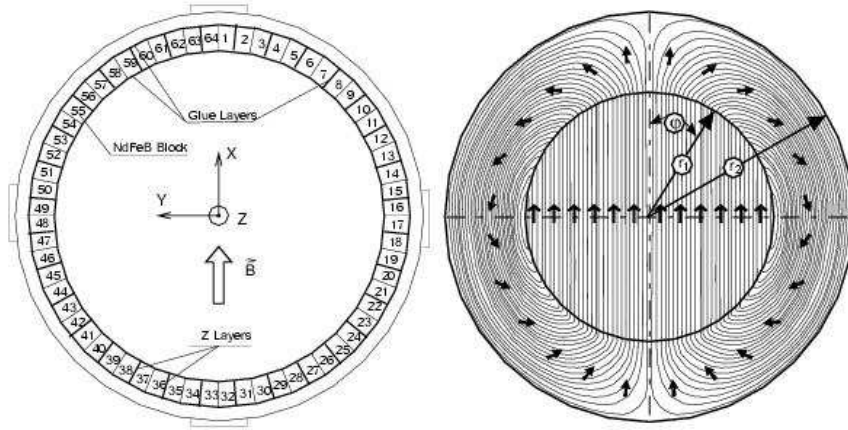


**Fig. 5.2:** x-y cross section through the AMS-01 permanent magnet: arrangement of block sectors and AMS coordinate system definition (*left*); magnetization of blocks and resulting field lines (*right*).

The magnetic field was not homogenous. As seen in Figure 5.3 (*left*), its dominant component  $B_x$  reached a flat maximum of 0.14 T at the center of the magnet and dropped

<sup>1</sup>Beta cloth is a fabric woven from fine quartz threads and impregnated with teflon or silicone based materials [127].

<sup>2</sup>Details about the connection of the AMS-01 coordinate system to the Shuttle and the Earth frames of reference are given in [128].

quickly with increasing values of  $|z|$ . At the upper and lower edges of the magnet its strength decreased to about 64 % of its maximum, while it was down to 14.9 % at  $z = 83$  cm, the upper end of the detector. Furthermore,  $B_x$  was not constant within a cross section in the x-y-plane (Figure 5.3, *right*), but grew with increasing values of  $|x|$  up to approximately 250 mT. The magnet had very small flux leakage outside its volume and a vanishing dipole moment, since the latter, in combination with the geomagnetic field, would have implied a torque on the spacecraft. The strength of the magnetic field as a function of the space coordinates was measured with high accuracy and is available for the offline analysis of AMS-01 data.

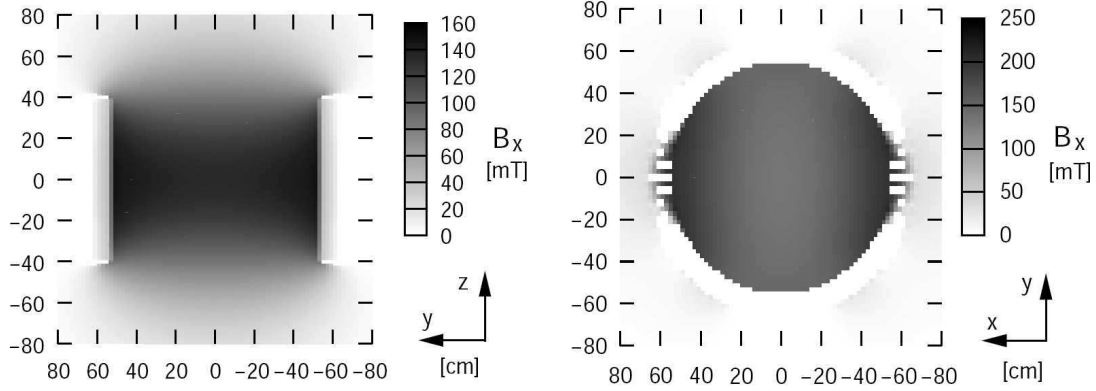


**Fig. 5.3:** The strength of the x-component  $B_x$  of the magnetic field: vertical cross section at  $x = 0$  (*left*) and horizontal cross section at  $z = 0$  (*right*). White areas denote negative values.

### 5.1.2 The Time of Flight Hodoscopes

The time of flight scintillation counter hodoscopes (TOF) of AMS-01 basically had three different tasks:

- delivering a fast trigger signal to the data acquisition system,
- measuring the value and direction of an incident particle's velocity,
- determining the absolute charge of a particle from its energy loss in the scintillators.

The TOF system consisted of four planes of Bicron BC-408 scintillator paddles, each plane covering a total area of roughly  $1.6 \text{ m}^2$ . The planes were grouped in two stations, i.e. double layers of scintillator paddles oriented perpendicularly to each other, allowing two space points to be measured on the particle trajectory, one above and one below the magnet. The distance of two paired planes was 12 cm, the distance from the upper to the lower station approximately 130 cm. Thus a particle with  $\beta \approx 1$  traverses the time of flight system in about 4.3 ns.

One TOF plane was composed of 14 rectangular scintillator panels, 1 cm thick and 11 cm wide with a length between 72 and 136 cm to account for the circular shape of the plane. In order to avoid dead space, adjacent paddles were mounted with 0.5 cm overlap. Each paddle was wrapped in aluminized mylar foil and encased in a 0.6 mm thick carbon

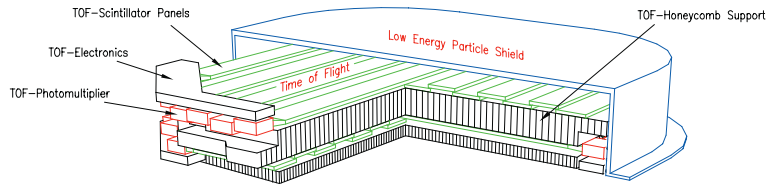


**Fig. 5.4:** Schematic view of the upper TOF planes and the LEPS.

fiber housing. Each scintillator double layer was supported by a 10 cm thick aluminum honeycomb panel glued between two aluminum skins of 5 mm thickness [129].

A total of six photomultipliers (Hamamatsu R5900), grouped in two triplets, was used to read out a single paddle. Both sides of the paddles were terminated with one triplet of photomultipliers via 5 cm long trapezoidal light guides. The anode signals from a triplet, as well as those from the next to last dynodes, were summed to form two output signals for each side of a paddle.

Prior to the launch of the experiment the time resolution of a single scintillator plane was determined from cosmic ray tests [129] to be 126 ps, resulting in an error of 178 ps on the total flight time. The position of passage of a particle through the scintillators can be determined with an accuracy of 1.8 cm along a panel.

The charge measurement is performed using the time information, based on a time-over-threshold method. Though not optimized for this task, the TOF system was thus capable of distinguishing particles with charge  $|Z| = e$ ,  $|Z| = 2e$  and  $|Z| > 2e$  with a purity better than 1 % [130].

### 5.1.3 The Silicon Strip Tracker

For the measurement of position and energy loss of particles AMS-01 featured a high quality tracking device based on silicon microstrip sensor technology [131]. It was designed to provide a position resolution of  $10\ \mu\text{m}$  in the bending plane and  $30\ \mu\text{m}$  in the non-bending plane of the magnetic field.

#### Tracker Layout and Electronics

The layout of the tracker is displayed in Figure 5.5 (*left*). The silicon was arranged in 6 planes roughly 20 cm apart (see Table 5.1). Four of the planes were located inside the magnet bore, enclosed in a carbon fiber cylindrical shell. Each plane was supported by a 12 mm thick aluminum honeycomb disk dressed with  $220\ \mu\text{m}$  carbon fiber skins. Above and below the magnet, two additional layers were mounted on stiffer disks (4 cm thick with 0.7 mm cover) for mechanical stability.

Layer no.	1	2	3	4	5	6
z position [cm]	50.98	29.19	7.79	-7.82	-29.18	-50.98

**Tab. 5.1:** The z position of the tracker layers in the AMS coordinate system.



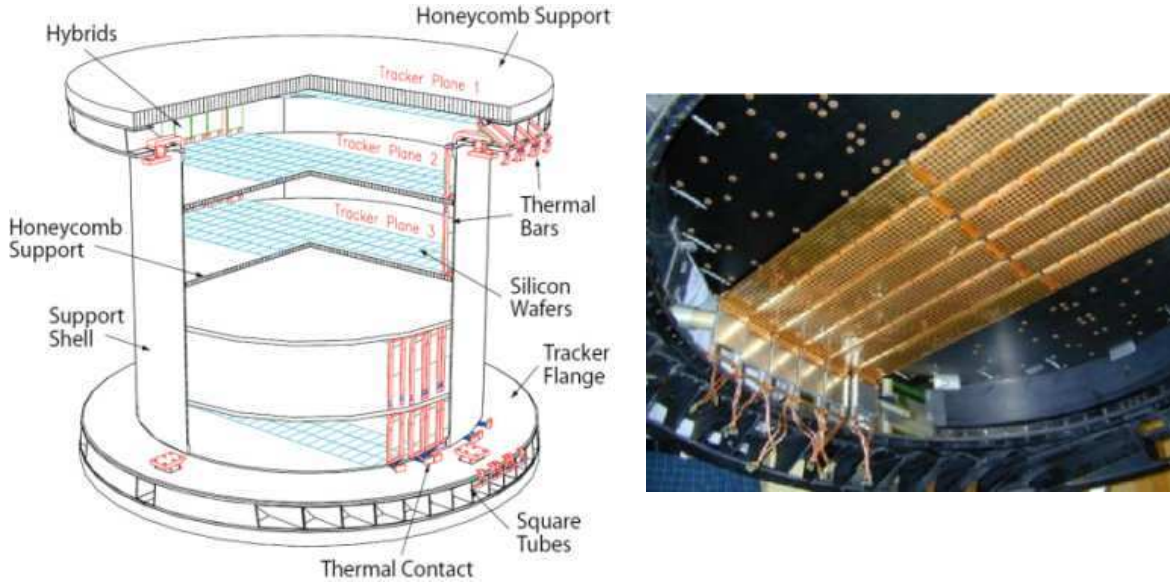


**Fig. 5.5:** Schematic view of the silicon strip tracker and its support structure (*left*); picture of the fifth tracker layer during detector disassembly (*right*).

The basic tracker elements were the  $300\,\mu\text{m}$  thick silicon microstrip sensors of size  $40.14 \times 72.04\,\text{mm}^2$ . The sensors were double sided with parallel strips implanted in the  $n^+$  bulk silicon on both sides. Strips on opposite sensor sides were perpendicular to each other [132]. On the p-(junction-)side, which measures the y-coordinate, the implants had a pitch of  $27.5\,\mu\text{m}$  with every second implant covered with an aluminum readout strip on the surface. On the ohmic n-side the implantation pitch was  $26\,\mu\text{m}$  with every implant aluminized. Every fourth implant was read out on both sides, resulting in a readout pitch of  $110\,\mu\text{m}$  for the p-side and  $208\,\mu\text{m}$  for the n-side.

Between 7 and 15 sensors were arranged in linear structures, the so called *ladders*, of different length to account for the overall circular shape of the layers. Within a ladder, the p-side readout strips of all sensors were daisy chained with wirebonds and connected to the p-side frontend hybrid. The n-side strips were connected to the n-side frontend hybrid through a metalized kapton foil, directly glued to the sensors. The kapton foil incorporated 2 groups of 192 lines each, with adjacent sensors connected to a different group. As a consequence of this bonding scheme [133] (see Figure 5.6) and depending on the number of sensors in a ladder, between 4 and 8 strips on different sensors were connected to the same readout channel, thus leading to an ambiguity in the assignment of tracker hits to the n-side strips. The two hybrids were attached back-to-back at each ladder's very end, close to the magnet wall, and were perpendicular to the sensor planes. They were equipped with 64-channel  $VA_{\text{hdr}}$  readout chips [134], which performed charge-sensitive signal preamplification and shaping and also provided a sample-and-hold stage, buffer and multiplexer for sequential analog data output. In the onboard readout electronics, the output was digitized by fast 12-bit ADC after amplification. Further downstream, digital signal processors performed pedestal subtraction, noise determination and clustered the strip signals, so that compressed hit information was transmitted to the data

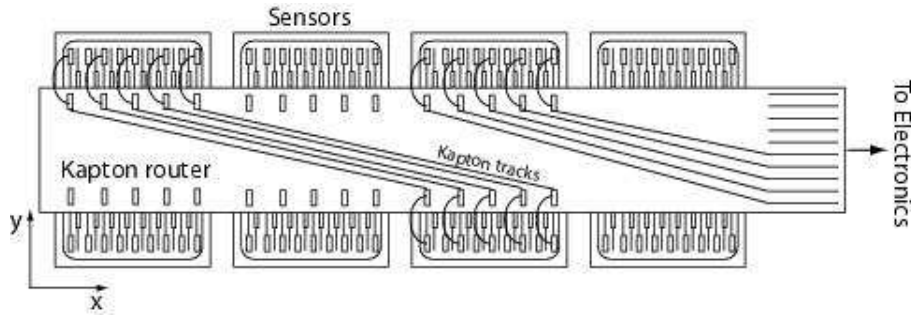


**Fig. 5.6:** The principle of n-side strip connection to the frontend electronics as a cause for ambiguities in the hit reconstruction. Connection via one kapton track group only is displayed.

acquisition of the experiment (zero suppression). For clustering, strips with signal amplitudes more than three times above their noise level  $\sigma_{\text{ped}}$  were used as seed strips and grouped with neighboring strips having amplitudes above  $1\sigma_{\text{ped}}$  to form clusters of at most 5 strips [131]. The cluster position was determined from the center of gravity of the strip signal amplitudes.

As evident from Figure 5.5 (*right*), the tracker planes were not fully instrumented. From the full number of 1912 sensors, 778 were finally assembled [135], covering a total area of more than  $2\text{ m}^2$ . In this configuration, the tracker had an acceptance of  $0.31\text{ m}^2\text{sr}$  for particles traversing four or more layers of instrumentation [132].

## Tracker Characteristics and Performance

Using the framework of the offline software, the characteristics and the performance of the tracker were determined with single-track events from flight and from test beam data. Two different methods were used for track fitting, based on an iterative Kalman filter approach or on the numerical integration of the equation of motion of particles in a magnetic field. For singly charged particles, Figure 5.7 (*left*) shows the rigidity resolution  $\Delta R/R$  as a function of rigidity, for tracks with 4, 5 or 6 measured points from flight and CERN-PS test beam data, in comparison with Monte Carlo results [136]. Multiple scattering limits the rigidity resolution to a level of 9% in the low rigidity range up to approximately 10 GV. For higher energies, the resolution deteriorates rapidly as a consequence of the finite magnetic field and the sensor spatial resolution.

On the right side of Figure 5.7, the average energy loss per tracker plane is displayed for protons and helium nuclei from flight data [131]. The energy loss is derived solely from p-side strip amplitudes and corrected for path length in the silicon. Fits of a sum of Landau and Gauss functions to the distributions give a most probable energy deposition of 96 keV for protons and 397 keV for helium nuclei.

The detection efficiency for a single plane is determined by the number of bad channels in the silicon, as well as by the fact that adjacent ladders were mounted on the support structures without overlap. The average total efficiency of the individual tracker planes varied between 80 % and 85 %, depending on the signal to noise ratio, which is a function of tracker temperature and thus of time. The contribution from bad channels – which

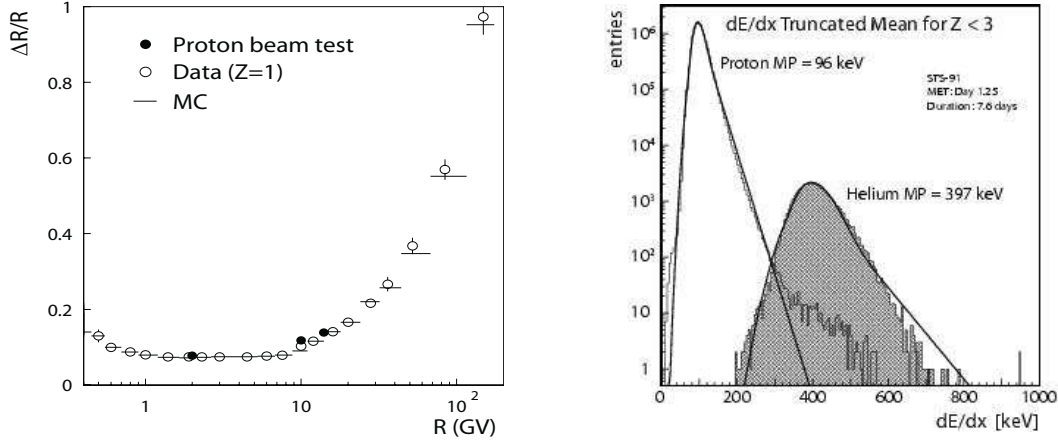


**Fig. 5.7:** The tracker rigidity resolution as a function of rigidity [136] determined for well defined tracks from flight and test beam data and compared with Monte Carlo simulations (*left*); truncated mean of energy loss in the tracker planes [131] for protons and helium nuclei (hatched histogram) from data, based on p-side strip measurements (*right*).

may be due to high noise level, defective readout electronics, or non-linear signal response – sums up to approximately 12 % of the inefficiency.

During the Space Shuttle flight there were deviations of the tracker support structure position from its nominal value in the order of 30  $\mu\text{m}$  due to temperature variations. These deformations were monitored with an onboard infrared laser system [137]. The tracker was finally aligned through post-flight metrology and the analysis of high-rigidity tracks from flight data [138].

#### 5.1.4 The Aerogel Threshold Čerenkov Detector

Mounted underneath the lower time of flight scintillator layers, the Aerogel Threshold Čerenkov Detector (ATC) provided separation of antiprotons from electrons or protons from positrons for momenta below 3.5 GeV/c.

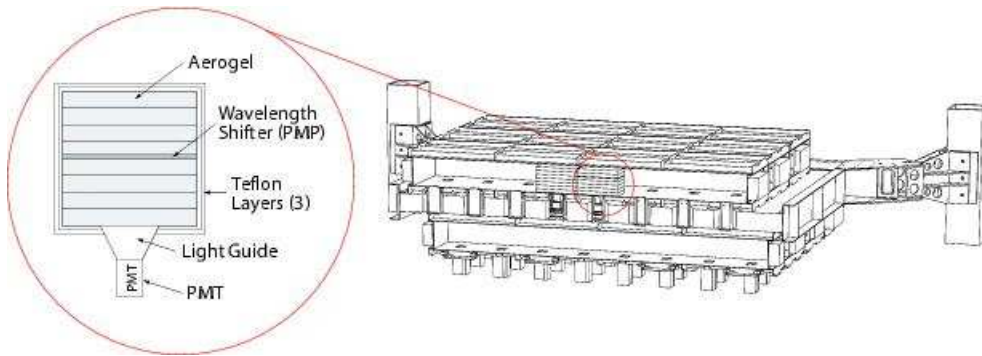


**Fig. 5.8:** Cross section of the Aerogel Threshold Čerenkov Detector and detail of the structure of an aerogel cell [139].

The ATC was composed of aerogel cells with a volume of  $11 \times 11 \times 8.8 \text{ cm}^3$ , as shown in Figure 5.8. Each cell was filled with 8 slabs of 1.1 cm thick aerogel blocks and surrounded by 3 layers of teflon, each  $250 \mu\text{m}$  thick, to reflect Čerenkov photons back into the cell volume. At the bottom end, a photomultiplier was attached to the cell via a light guide. The efficiency of the photomultiplier reached a maximum at wavelengths of approximately 420 nm. In order to reduce photon losses due to scattering and absorption, a  $25 \mu\text{m}$  wavelength shifting layer was inserted between the aerogel slabs in the middle of each cell.

The 168 aerogel cells were grouped into two layers of  $8 \times 10$  and  $8 \times 11$  cells respectively, and were enclosed in a thin carbon fibre structure. Bolted to a 5 cm thick honeycomb plate which was glued into an aluminum frame, the layers were attached to the support structure on which the AMS-01 experiment was mounted in the Space Shuttle payload bay.

The data from the ATC are not used in this analysis, since they provide no background suppression in the high momentum range above 3.5 GeV/c. A detailed description of the device is given in [139].

### 5.1.5 The Veto Counters

The 16 veto or anti-coincidence counters (ACC) were mounted on the inner magnet surface, thus surrounding the tracker. Their purpose was to provide detection of particles which entered or exited the detector volume through the magnet wall, thus typically indicating multi-particle events involving  $\delta$ -ray creation or the presence of low quality tracks. Each counter consisted of a 1 cm thick scintillator paddle 80 cm high and 20 cm wide with implanted wavelength shifting fibers. At both ends of the paddles, the fibers were viewed by a single photomultiplier.

### 5.1.6 Material Budget

Depending on direction of flight, particles had to traverse a certain amount of material before they could reach the tracker. This fact has important implications for this data analysis. Additional material induces multiple scattering of particles and hence reduces the spatial and angular resolution of reconstruction algorithms. On the other hand, it increases the probability of processes such as bremsstrahlung and gamma conversion, which are the focus of this work, and therefore improves the reconstruction efficiency.

Table 5.2 summarizes the dominant contributions to the overall material budget from particular components and subdetectors of AMS-01 outside the tracker. While the thermal shielding and the LEPS were located on top of the experiment, the aerogel was in the lowermost subdetector of AMS-01 and was located below the tracker. As a consequence, for particles entering AMS-01 from the top (*downward*), the total amount of material to be traversed before reaching the tracker was equivalent to 18.2 % of a radiation length, while for particles entering from the bottom (*upward*) it amounted to 19.2 %. Each tracker layer, including the silicon and the support structure, contributed another 0.65 % of a radiation length to the material budget [131].

Component	% $X_0$	Ref.
Thermal shielding	3.2	[140]
LEPS	3.9	[140]
TOF double layer	9.7	[140]
TOF double layer support	1.4	[140]
Aerogel	8.0	[141]

**Tab. 5.2:** Contribution to the overall material budget from the components of AMS-01 outside the tracker, in percent of a radiation length.

In addition to the components of the experiment itself, additional objects have to be considered for the material budget for upward going particles, namely the Space Shuttle and the AMS-01 support structure in it. As shown in Figure 5.9, the mounting frame of AMS-01 (*Unique Support Structure, USS*) consisted of aluminum box beams and truss elements, some of which were within the acceptance of the detector. The 4 mm thick outer aluminum wall was covered with low density silica fiber tiles [142], forming the heat shield. Besides, the floor contained trusses, as well as hydraulic and electric circuitry. Additionally, the inner surface of the payload bay was lined with a protective blanket made of composite fabric material. Precise information about the structure of the Space Shuttle’s payload bay floor, which would allow an exact determination of the material distribution underneath AMS-01, is not available. The amount of this additional material is estimated to be 4.5% of a radiation length from the specifications of dimensions and weight of the Space Shuttle fuselage [142].

## 5.2 Trigger and DAQ Livetime

The trigger chain of AMS-01 was divided into three successive stages: the hardware-based *Fast Trigger*, and the *Level-1* and *Level-3* stages, which were implemented in the data acquisition software<sup>3</sup>. Each trigger stage definitely rejected an event if its particular requirements were not fulfilled [143]. For trigger efficiency studies, a small fraction of events – approximately 1 in 1000 – was accepted after a positive decision of the Fast Trigger only (*prescaled events*).

The **Fast Trigger** signal was derived solely from the photomultiplier triplets (summed anode signals) viewing the TOF scintillators. A Fast Trigger was generated if at least one scintillator panel signaled a hit from one or both end triplets in each of the four TOF planes. The typical time for the Fast Trigger stage to generate the signal was 100 ns. If after another 200 ns none of the following trigger requirements were fulfilled, the event was rejected.

The first trigger condition of the **Level-1 stage** was called *matrix condition* and accounted for the fact that the tracker layers were not fully equipped. By comparison with a correlation matrix, those combinations of TOF scintillator panels on layers 1 and 4 which

<sup>3</sup>A Level-2 stage was not implemented.



were incompatible with a particle traversing the tracker instrumentation were identified and the corresponding events were rejected. The second trigger condition of the first stage demanded the absence of signals in any of the veto counters.

The **Level-3 stage** assured the coincidence of the two photomultiplier triplets on either side of the TOF panels used for the fast trigger decision. Furthermore, it performed a clustering of the TOF hits, forming clusters either from one hit in a single panel or from two hits in two adjacent panels. A single cluster was then required in each of the first and the last TOF planes in coincidence with at least one additional cluster in the second and/or the third plane. These TOF clusters defined a 6 cm wide corridor in the bending plane. The Level-3 stage retained the event, if at least three tracker hits were found within this corridor with a signal to noise ratio above 4 [136]. Events with multiple clusters on a single TOF plane were rejected [144]. The latter trigger criterion has a negative impact on this data analysis, since it deteriorates the acceptance for the signal process towards lower particle momentum (see § 7.2.1).

An additional feature of the Level-3 stage was active during the first seven hours of data taking [144]. Its main purpose was the rejection of low energy particles with  $|Z| < 3$ . The algorithm relied on the measurement of the average residual of tracker clusters with respect to a straight line joining the uppermost and the lowermost cluster. Events were accepted if the average residual was below  $300 \mu\text{m}$ .

The total dead time per trigger operation amounted to  $85 \mu\text{s}$  [46]. In case an event was rejected by the Level-1 stage, it took  $7 \mu\text{s}$  until the data acquisition system (DAQ) was again operational. Consequently, the fraction of time during which the DAQ was active (DAQ *livetime*) significantly depended on the particle rate, which itself varied with the position of the detector in the geomagnetic coordinate system. At low magnetic latitude, particle rates were small and the readout rate reached up to 1.6 kHz. Except over the South Atlantic, where the geomagnetic field is exceptionally weak<sup>4</sup> resulting in very low readout rates due to a large amount of trigger dead time, the minimum readout rate was 100 Hz.

### 5.3 AMS-01 on the Space Shuttle

The AMS-01 experiment was flown on the Space Shuttle *Discovery* in the course of the STS-91 mission<sup>5</sup> from June 2nd to 12th, 1998. Figure 5.9 shows the mounting of AMS-01 in the spacecraft's cargo bay. During its flight the *Discovery* orbited the Earth at altitudes between 320 and 390 km with an orbital period of 93 min and an inclination of  $\pm 51.7$  degrees. From June 4th to 8th, for a total of 95 hours, the Space Shuttle was docked to the *Mir* space station. During docking, parts of the *Mir*, such as the Soyuz-TM and the Priroda modules, were within the acceptance solid angle of the AMS-01 experiment [145] (see Figure 5.11).

The 184 hours of data taking were divided into several periods. As seen in Figure 5.10, the pointing angle of AMS-01 – the angle of the positive z-axis with respect to the zenith direction – varied with time. Before docking to the *Mir*, the pointing angle was kept

<sup>4</sup>A phenomenon known as the *South Atlantic Anomaly* (SAA)

<sup>5</sup>STS: Space Transportation System



constant at 45 degrees. After decoupling from the space station, the experiment was operated at consecutive angles of 0, 20, 30, 45 and 180 degrees. During the latter phase, the z-axis of AMS-01 pointed towards the Earth for the measurement of outbound particles emitted from the atmosphere (*albedo phase*). While the Discovery was docked to the Mir, the pointing angle could not be kept constant; it oscillated between roughly 40 and 140 degrees with the Mir orbital frequency of about  $0.65 \text{ h}^{-1}$ . Several short loss-of-signal periods occurred during the flight, partly because the electronics had to be shut down due to overheating when the shuttle was pointing towards the zenith [146].

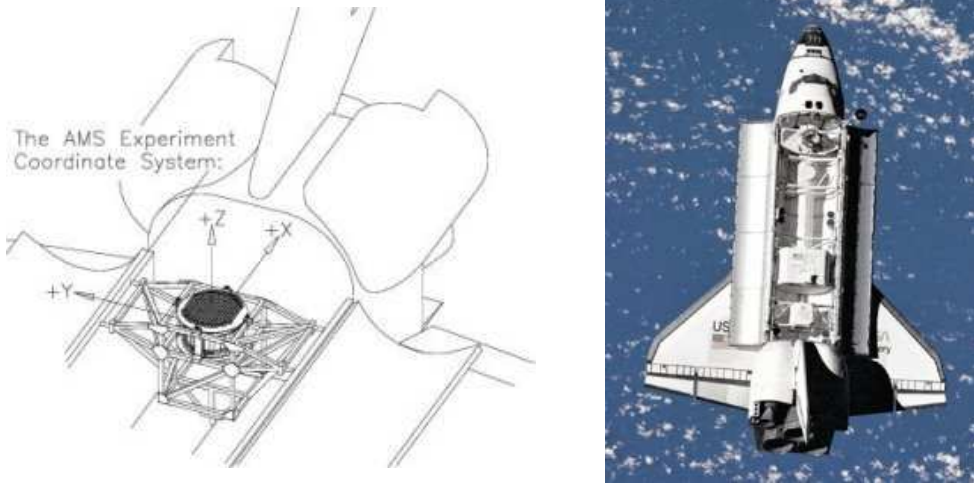


**Fig. 5.9:** The mounting of AMS-01 in the Space Shuttle's cargo bay (*left*); photograph of the Space Shuttle taken from the Mir space station (*right*).

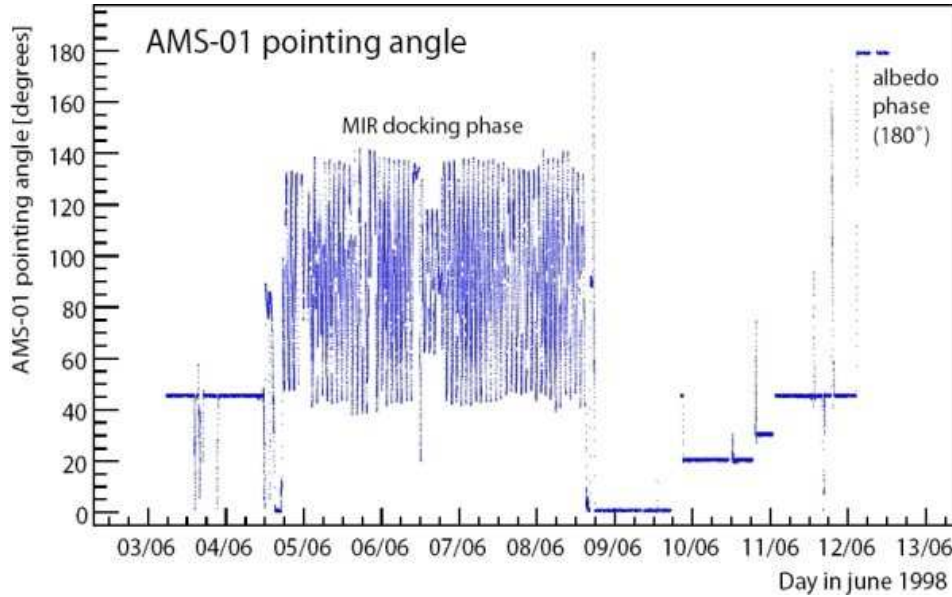


**Fig. 5.10:** The pointing angle of AMS-01 as a function of time.

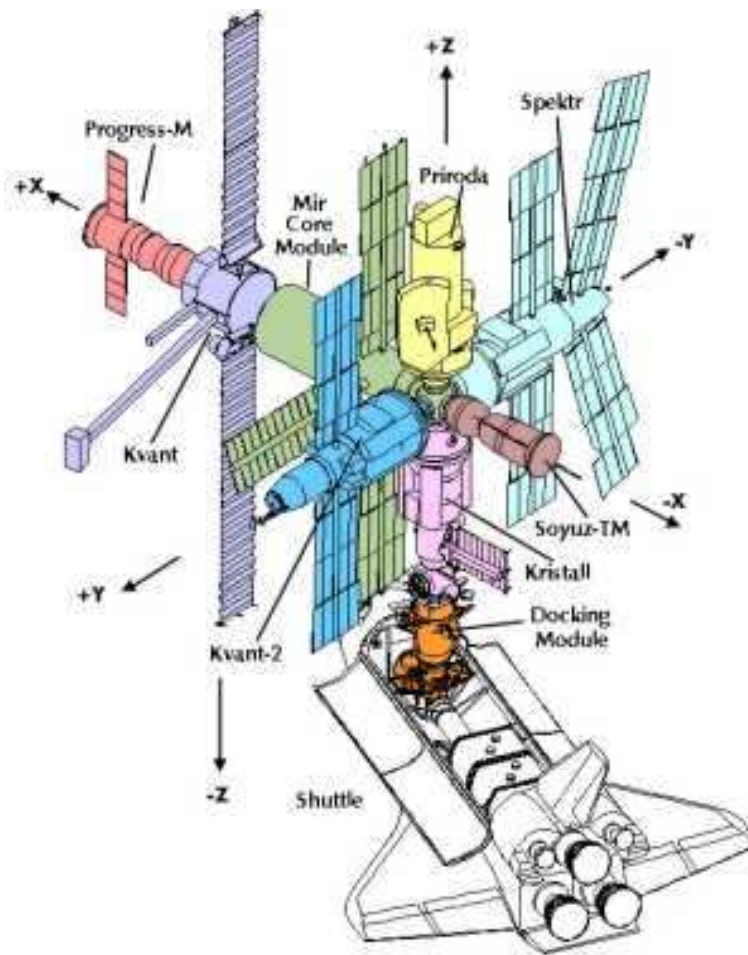


**Fig. 5.11:** Schematic view of the Space Shuttle docked to the Mir space station [147]. The Soyuz-TM and the Priroda modules were within the acceptance of the AMS-01 experiment.

## 6 Positron Identification through Bremsstrahlung Conversion

### 6.1 The Challenge of Positron Measurements

The main challenge of high energy cosmic ray positron measurements is the suppression of the vast proton background. As already stated in chapter 4, the flux of cosmic ray protons exceeds that of positrons by a factor of  $10^4$  in the momentum range of 1–50 GeV/c. Besides the fact that both particle species have the same charge, their energy deposition in traversed material becomes comparable at energies beyond a few GeV. Thus, the identification of positrons must rely either on techniques based on measurement of the Lorentz factor, as realized for example in Čerenkov counters or transition radiation detectors, or on high-resolution calorimetry.

However, as described in the last chapter, AMS-01 was not equipped with a calorimeter and its ATC subdetector provided a sufficient proton rejection only for momenta below 3.5 GeV/c. In order to extend the energy range accessible to the experiment, a completely different approach has been chosen. It relies on the identification of bremsstrahlung emission through photon conversion, the latter also referred to as pair production.

### 6.2 Conversion of Bremsstrahlung Photons

Both bremsstrahlung and photon conversion cannot occur in vacuum, but require the presence of a Coulomb field, predominantly that of a heavy object like a nucleus, so that momentum and energy conservation are satisfied. They are closely related electromagnetic processes whose energy-angle distributions can be calculated with the Bethe-Heitler formalism. For bremsstrahlung from electrons or positrons and in the limit of high energies this distribution is given by the cross section [148]

$$\sigma_b(k, x) \propto Z^2 \frac{dk dx}{m^2 k} x \left\{ \frac{16x^2 E}{A(x)} - \frac{(E_0 + E)^2}{B(x)} + \left[ \frac{E_0^2 + E^2}{B(x)} - \frac{4x^2 E}{A(x)} \right] \cdot \ln M(x) \right\}, \quad (6.1)$$

with

$$A(x) = (x^2 + 1)^4 E_0, \quad B(x) = (x^2 + 1)^2 E_0^2, \quad \frac{1}{M(x)} = \left( \frac{mc^2 k}{2E_0 E} \right)^2 + \left( \frac{Z^{1/3}}{C(x^2 + 1)} \right)^2,$$

where  $E_0$  and  $E$  denote the energy of the lepton before and after the radiation process,  $k = E_0 - E$  the energy of the photon,  $Z$  the charge number of the scattering nucleus,  $m$  the electron mass and  $c$  the speed of light.  $C$  is a constant of the order of  $10^2$ , which expresses the screening effect of the atomic electrons bound to the nucleus. The variable

$x$  is equal to the reduced angle  $\gamma\theta$ ,  $\gamma$  being the lepton's Lorentz factor and  $\theta$  the angle of the radiated photon with respect to the incident lepton.

The bremsstrahlung matrix element is related to those of pair production by the substitutions  $k \leftrightarrow -k$  and  $p \leftrightarrow -p$ , where  $p$  is the four-momentum of the incident particle in bremsstrahlung emission or the four-momentum of one of the pair particles in pair production. Thus, the energy-angle distribution for pair production has a mathematical form similar to that for bremsstrahlung, with  $\theta$  being the angle of one of the leptons with respect to the incident photon [149].

The above cross section (6.1) depends inversely on the square of the incident particle mass. Hence it follows that bremsstrahlung emission is suppressed by a factor of more than  $3 \cdot 10^6$  for protons with respect to positrons. This important property of the bremsstrahlung process has a very beneficial implication: identification of the radiated photon, in conjunction with a measurement of the charge sign of the incident radiating particle, determines the latter almost certainly as a positron (or electron). This principle is the basis for the proton background suppression as performed in this analysis.

### 6.2.1 Event signature

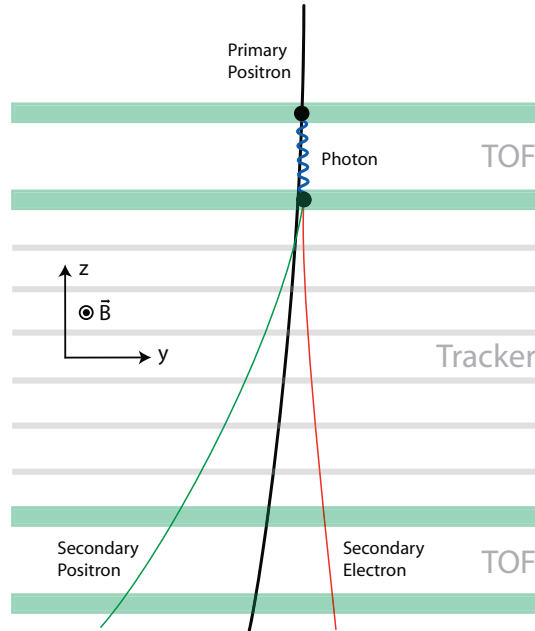


**Fig. 6.1:** Schematic view of a converted bremsstrahlung event caused by a downward going positron.

Figure 6.1 shows the topology of an event with a converted bremsstrahlung photon. Here, a primary positron enters the detector volume from above and emits a bremsstrahlung photon in the first TOF scintillator layer. The photon then converts into a secondary electron-positron pair in the second TOF layer in this example. If the

conversion process takes place above or in the upper part of the tracker, the tracks of three particles can in principle be reconstructed.

Eq. (6.1) can be integrated over  $x$  to obtain the root-mean-square angle  $\theta_{rms}$  of the photon with respect to the incident lepton, yielding  $\theta_{rms} = q(E_0, k, Z)/\gamma \cdot \ln \gamma$  for high energies [150]. Since  $q(E_0, k, Z)$  depends primarily on  $k/E_0$  and is always of the order of unity, it follows that  $\theta_{rms} \approx 1/\gamma$ . As a consequence, in the GeV energy range, bremsstrahlung photons are largely emitted under angles of  $10^{-3}$  rad or smaller. The same applies to the opening angles of the electron positron pairs from pair production. In a tracking detector, these values fall below the typical limit of track reconstruction accuracy given by multiple scattering and thus are practically equal to zero.

Furthermore, it can be seen from eq. (6.1) that the spectrum of the emitted photons is soft, since the cross section decreases with  $1/k$ . Because of the low fraction of momentum which is typically carried away by the photon, the secondary particles have lower momenta than the primary. Therefore, in the bending plane projection of the spectrometer, the secondaries tend to form the left and right tracks, while the primary remains in the middle (see Figure 6.1). It must be pointed out that in the GeV energy range the fraction of momentum given to each of the secondary particles is approximately uniformly distributed between 0 and  $E_\gamma$ . In the limit of high energies, the distribution of the ratio of the two secondary momenta becomes slightly asymmetric, with electron-positron pairs having considerably different momenta being favored.

## 6.2.2 Background

The background to positron identification through bremsstrahlung conversion is caused by protons undergoing hadronic reactions in the material of the experiment, as well as by electrons with wrongly reconstructed momentum sign.

Mesons produced in hadronic reactions involving protons can mimic the three-track signature of converted bremsstrahlung events. These mesons are almost exclusively pions; the cross section for the production of kaons or other mesons is in comparison more than one order of magnitude smaller [151]. Several processes contribute to this background and can be grouped in two categories, where  $p, n$  denote an incident proton, or a proton or neutron in the scattering nucleus (cross sections are taken from [152]):

- processes involving charged pion production, dominantly  $pp \rightarrow pp\pi^+\pi^-$  and  $pn \rightarrow pn\pi^+\pi^-$ , with cross sections of approximately 2 mb above a threshold of 3 GeV incident proton energy, and
- processes involving neutral pion production, such as  $pp \rightarrow pp\pi^0$  or  $pn \rightarrow pn\pi^0$ , with cross sections of approximately 2 mb or 4 mb, respectively, above a threshold of 1 GeV incident proton energy.

In case of neutral pion production, the  $\pi^0$ 's decay almost exclusively into photon pairs after a mean flight path of  $c\tau = 25$  nm. If one of the photon remains undetected, while the other one converts into an electron positron pair, the resulting three-track event signature is that of a converted bremsstrahlung event. Due to the procedure for vertex reconstruction, discussed in § 6.3.4, the fact that – in contrast to the signal process –

only one vertex is present in the above hadronic interaction cannot be used to effectively discriminate against the hadronic background.

The material of the experiment, in which the relevant reactions take place, mainly consists of carbon and hydrogen atoms. According to the optical model [153], the proton-proton cross sections  $\sigma_{pp}$  can be applied to proton-nucleus scattering when appropriately scaled as  $\sigma_{pN} = \sigma_{pp} A^\alpha$ , with  $A$  being the atomic weight of the target nucleus, and  $\alpha = 0.77$  for carbon. Hence, for a scintillator of the TOF system with a thickness of 1 cm, the probability for a proton to undergo one of the above reactions is of the order of 1 % for both charged and neutral pion production. However, the probability for such a reaction to give rise to a background event is much smaller due to several reasons. The spectral distributions of the secondary pions show distinct peaks at 100 MeV and decrease steeply towards higher energies [154]. The resulting momenta are typically very low and tend to prevent a hadronic event from exhibiting a three-track signature due to the strong deflection in the magnetic field. On the other hand, in contrast to converted bremsstrahlung events where the secondary tracks emerge from the vertex at small angles and are thus ordered according to their charge sign by the spectrometer magnetic field, secondary particles from hadronic interactions are emitted under large angles with respect to each other and may be any one of the three tracks with almost equal probability. Background from processes involving neutral pion production is further suppressed by the requirement that exactly one of the two photons from pion decay must convert. Let  $p \approx 7/9 X_0$  denote the pair production probability in a material with a thickness corresponding to a fraction  $X_0$  of a radiation length [155]. Then the suppression factor is  $\{p(1-p)\}^{-1} = 8.33$  for  $X_0 = 0.18$ , in the case of downward particles.

The average transverse momentum  $\langle p_T \rangle$  of mesons stemming from proton-proton interactions is  $\langle p_T \rangle \approx 0.35$  GeV/c, rather independent of the collision energy [156]. As a consequence, the angles  $\theta$  between particles emerging from interactions in the GeV energy range are large compared to those in bremsstrahlung conversion. For example,  $\langle \theta \rangle \approx 33 \cdot 10^{-3}$  rad at 10 GeV. This important characteristic of hadronic interactions allows to effectively discriminate against the proton background.

Determining from first principles the background from electrons with wrongly reconstructed charge sign is naturally harder due to the rather complex behavior of track reconstruction algorithms. As Figure 5.7 on page 59 shows, the rigidity resolution of the tracker has a constant value of about 9 % in the range 1–9 GV and then rises linearly with increasing rigidity. For high energy particles, the resolution rapidly worsens so that the probability of bad reconstruction increases. If the resolution is approximated by the width  $\sigma$  of a normalized Gaussian distribution  $G(R, \hat{R}, \sigma)$  of the rigidity  $R$  around a true mean value  $\hat{R}$  (which is negative for electrons), then the probability  $p_w$  of wrong charge sign reconstruction is given by the integral

$$p_w = \int_0^\infty G(R, \hat{R}, \sigma) dR. \quad (6.2)$$

Due to the quickly falling edges of the Gaussian distribution, the value of  $p_w$  is practically zero for low rigidities. At 50 GV it amounts to approximately 1 % and hence the amount of misidentified electrons remains small compared to the positron to electron ratio.



Apart from these rather coarse estimations, the properties of the background sources, as well as their individual contributions to the signal event sample, must be precisely determined by Monte Carlo simulation. In § 6.4.2 it will be shown that in the course of the analysis the probability for a proton to create a background event can be reduced to less than  $10^{-7}$ , and the contamination of the positron sample from badly reconstructed electrons remains below the percent level.

## 6.3 Event Reconstruction

The task of the event reconstruction process is to identify candidates for converted bremsstrahlung events and reconstruct the event geometry and particle momenta. In order to obtain the highest possible selection efficiency, it is mandatory to apply sophisticated track and vertex finding algorithms which are particularly customized for the signature of converted bremsstrahlung. In a first step, a fairly permissive preselection algorithm extracts signal candidates from the AMS-01 data set. Two independent track finding algorithms, each of them optimized for a particular event topology, are separately applied to the preselected event sample. In case that three particle tracks are found, their corresponding momenta are determined, and the bremsstrahlung and conversion vertices are spatially reconstructed. As argued in § 6.2.1, the middle track is considered to stem from the primary particle, while the left and right tracks represent the secondary electron positron pair. To account for the asymmetric geometry of the detector along its z-axis, event reconstruction and analysis are performed separately for particles traversing the detector from top to bottom (*downward*) and from bottom to top (*upward*).

Before the analysis, the raw data recorded by AMS-01 were preprocessed [157]. This procedure included, amongst others:

- reconstruction of the spatial coordinates of the tracker hits and their errors,
- reconstruction of the energy deposits and relative transit times of particles in the TOF scintillator layers, and
- calculation of the *trigger livetime*, i.e. the fraction of time over which the trigger electronics of the experiment were accepting signals (see § 7.2.2).

### 6.3.1 Preselection

The event reconstruction algorithms developed for this analysis are rather complex and require substantial amounts of computing time because of their combinatorial character. The task of the preselection is to considerably reduce the size of the AMS-01 data, so that the algorithms can operate on a reasonably small sample of event candidates.

In a first step, all hits in the silicon strip detectors of the tracker are projected into the bending plane for one dimensional clustering. On a particular tracker layer, a cluster seed is defined by a single arbitrary tracker hit. Subsequently, further hits are added to an existing cluster if their distance from the barycenter<sup>1</sup> of this cluster along the y-axis is

---

<sup>1</sup>The barycenter is the weighted mean of the hit coordinates, with the hit amplitudes as weights.

smaller than  $100\ \mu\text{m}$ . If a hit cannot be added to any existing cluster, it is used to start a new cluster. In this procedure, the x-coordinates of the tracker hits are not regarded, and the clusters are defined in the bending plane (y-z plane) only (see Figure 6.3). Thus the hits in a given cluster may spread over the whole length of the particular tracker layer along the x-axis. Most of them are virtual hits caused by the tracker bonding scheme (see § 5.1.3). This ambiguity is resolved by the track finding algorithms in a subsequent step (see § 6.3.2). Moreover, there may be clusters comprised of a single hit only.

For further analysis, a minimum of 8 tracker clusters are required. Events are selected in which at least two of the six layers of silicon detectors contain exactly three clusters each (*triplets*). By these means, a reduction of the data size by a factor of 25 is achieved.

### 6.3.2 Track Finding

AMS-01 was designed for single particle detection, thus the software package for data analysis provided by the AMS-01 collaboration is optimized for the reconstruction of single-track events. The track finding algorithms implemented in this package have a small reconstruction efficiency for multi-track events, resulting in low event statistics when applied to a rare process such as bremsstrahlung conversion. As a consequence, alternative reconstruction methods had to be developed for this analysis. Two different track finding algorithms – in the following referred to as the *successive* and the *combinatorial* algorithm – are independently applied each to a subsample of the preselected events. Their purpose is to establish if an event exhibits a three-track signature and, if so, find the correct assignment of the tracker clusters to the three tracks. Each algorithm is optimized for a particular cluster topology and returns a set of parameterized track information.

With  $t$  denoting time, and  $\mathbf{p}$  and  $\mathbf{v}$  being the momentum and velocity of a particle of charge  $e$ , its equation of motion in a magnetic field  $\mathbf{B}$  is

$$\frac{d\mathbf{p}}{dt} = e(\mathbf{v} \times \mathbf{B}) . \quad (6.3)$$

In a homogeneous field, the solution of this equation is a helix trajectory. Since the magnetic field within AMS-01 is inhomogeneous, eq. (6.3) is preferably solved numerically. Nevertheless, the resulting trajectories can still be well approximated by a helix. The latter is fully parameterized with a set  $\mathbf{h}$  of five numbers, defined on any given plane  $z = z_0$  as

$$\mathbf{h} = \left[ x, \frac{dx}{dz}, y, \frac{dy}{dz}, \frac{1}{p} \right] . \quad (6.4)$$

An iterative fitting algorithm [158], particularly adapted for the AMS-01 experiment [159], is used to determine  $\mathbf{h}$  from a set of point measurements  $i$  of a particle's trajectory. The algorithm is based on minimization of the quantity

$$\chi^2 = \sum_i \left\{ \left( \frac{\hat{x}_i - x_i}{\sigma_{\hat{x}}} \right)^2 + \left( \frac{\hat{y}_i - y_i}{\sigma_{\hat{y}}} \right)^2 \right\} , \quad (6.5)$$

with  $x_i, y_i$  being helix parameters on the given  $z$  plane and  $\hat{x}_i, \hat{y}_i$  the measured hit coordinates on that plane with the corresponding measurement errors  $\sigma_{\hat{x}}, \sigma_{\hat{y}}$ . The algorithm returns  $\mathbf{h}$  at the  $z$ -position of the first measurement in the direction of flight. The minimum rigidity that can be reconstructed is 100 MV.

### The successive track finding algorithm

The successive track finding algorithm is customized for events in which at least three tracker layers are found with exactly three clusters on each of them. Its working principle is illustrated in Figure 6.2. Since particle tracks diverge in the magnetic field, the triplets – clusters on layers with exactly three clusters – are required to have increasing cluster distances along the  $z$ -axis in the direction of flight. With three particles having traversed the tracker, the clusters in the triplets can directly be assigned to a left, a middle and a right track segment (*initial track seeds*).

Subsequently, starting from the uppermost layer, further clusters on the other layers are tentatively added to each of the tracks. A cluster is finally appended to the track which yields the lowest  $\chi^2$  according to eq. (6.5), if the value of  $\chi^2$  is below a threshold of 30 (the fitting procedure is described in the next paragraph). In this case, the helix parameters of this track, including the new cluster, are updated. As the tracks grow, as many clusters as possible are attached to them. Clusters caused by noise or the occurrence of  $\delta$ -ray electrons are mostly incompatible with any of the tracks and remain isolated.

For the fitting procedure mentioned above, it is necessary to resolve the ambiguities in the  $x$ -coordinates of the clusters, caused by the clustering only in the bending plane projection. For this, a linear regression procedure [160] is carried out to obtain a straight line through the hits in the TOF system (see Figure 6.3). In the non-bending plane ( $x$ - $z$ -plane), a corridor of 10 cm width is defined around the straight line and only hits within

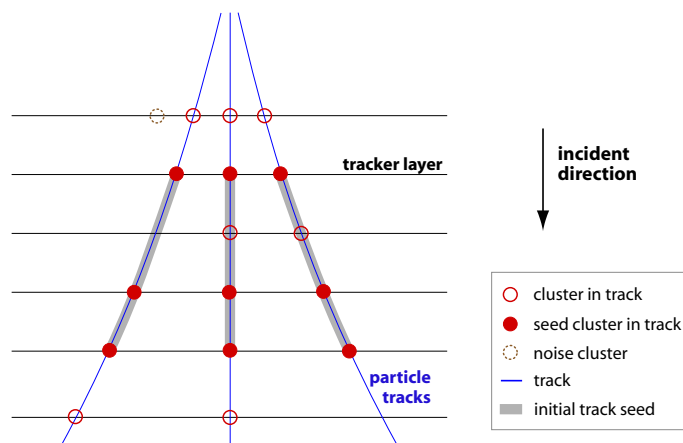


**Fig. 6.2:** Principle of the successive track finding algorithm in the bending plane projection. Initial track seeds are created from seed clusters on layers with exactly three clusters. Further clusters are successively added to the tracks, while noise clusters, which do not fit to any track, remain isolated. Missing clusters occur in parts of the tracker which are inefficient or not instrumented.

this corridor are retained. All possible combinations of remaining hits in the track – with at most one hit from each cluster – are then tentatively fitted, and the helix parameters are updated from the combination which yields the lowest value of  $\chi^2$  according to eq. (6.5).

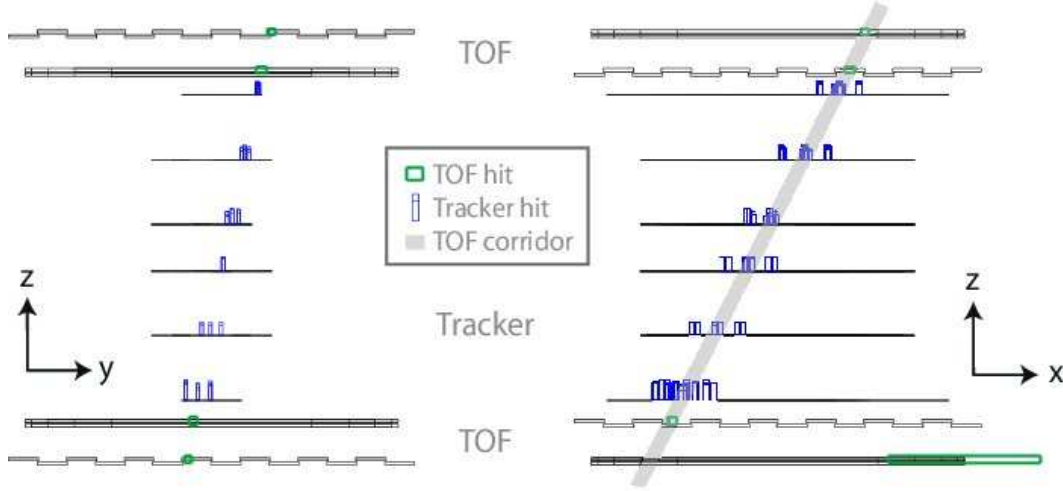


**Fig. 6.3:** Display of a three-track event, projected in the bending plane (*left*) and in the non-bending plane (*right*). Only the TOF system and the tracker are shown. The height of the hit boxes is proportional to the hit amplitudes, while their width represents the position measurement errors. On the right side, the hit selection corridor is plotted.

### The combinatorial track finding algorithm

In order to increase the efficiency for converted bremsstrahlung events, a generalized algorithm has been developed for the treatment of events that feature only two tracker layers with exactly three clusters each [161]. It is based on a combinatorial approach to the track finding problem. The basic idea is to examine every possibility (*track hypothesis*) of arranging the tracker clusters into three tracks and determine those combinations yielding the lowest value of  $\chi^2$  according to eq. (6.5). These track hypotheses have to pass several tests in order to reject wrongly assigned tracks. Additionally, two tracks may share one single cluster. The algorithm leads to an improvement of the efficiency by 40 %. A detailed description of this method is given in [161].

### 6.3.3 Vertex Reconstruction

Vertex reconstruction is based on parallel backtracing of tracks through the magnetic field of the detector using the functionality of the GEANT3 package (routine GRKUTA) [162]. For a given track of a particle  $i$  with charge  $q$  and momentum  $\mathbf{p}$ , a virtual particle  $\hat{i}$  with charge  $-q$  and momentum  $-\mathbf{p}$  is started at the first tracker cluster found in the flight direction of particle  $i$ . The propagation of  $\hat{i}$  is then performed by numerically solving the equation of motion in steps of  $100 \mu\text{m}$ , so that  $\hat{i}$  will follow the trajectory of the original particle  $i$  backward against its original flight direction.

The vertex finding for the case of downward going particles is performed as follows. The left and right tracks may have their starting cluster on different tracker layers. As a first step, the track starting at the lower layer is backtraced upward until it reaches the starting layer of the other track. Both tracks are then backtraced in parallel until their projected distance along the y-axis reaches a minimum. The vertex is then defined as the barycenter of the track points at the z-coordinate of closest approach of the tracks. In case the tracks intersect in the bending plane projection, the intersection point is taken as the vertex. The vertex finding for upward going particles is exactly similar, but with all directions reversed in z.

Finally, the four-vector of the photon is reconstructed from the four-vectors of the left and right tracks at the vertex position. Using the algorithm described above, the vertex of the photon and the middle track is then computed. In this case, the photon is simply propagated along a straight line.

### 6.3.4 Reconstruction Quality and Monte Carlo

The quality of the reconstruction algorithms is verified with  $16.8 \cdot 10^6$  electron and positron events from a complete Monte Carlo simulation of the experiment using GEANT3. The incident momentum spectrum of these Monte Carlo particles is proportional to  $p^{-1}$  and ranges from 1 to 60 GeV/c. For background studies an additional  $170 \cdot 10^6$  proton Monte Carlo events have been generated in the momentum range 6–150 GeV/c. All Monte Carlo particles are injected both from above and below into the acceptance solid angle of the experiment with a uniform spatial and angular distribution.

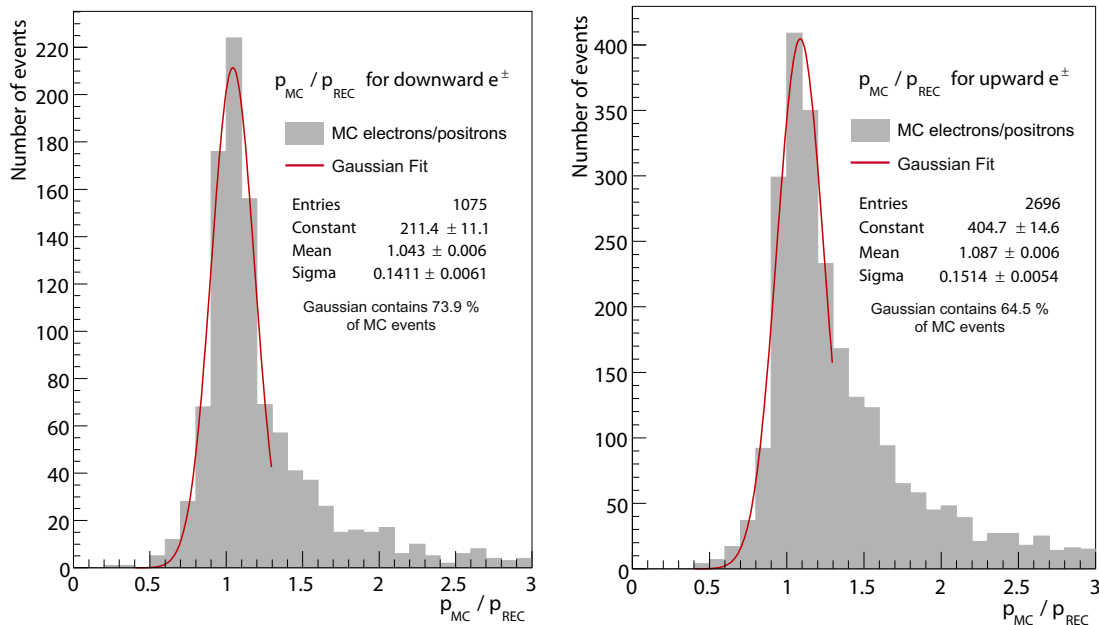


**Fig. 6.4:** Comparison of generated and reconstructed momentum (sum of three track momenta) for downward (left) and upward (right) going positrons.

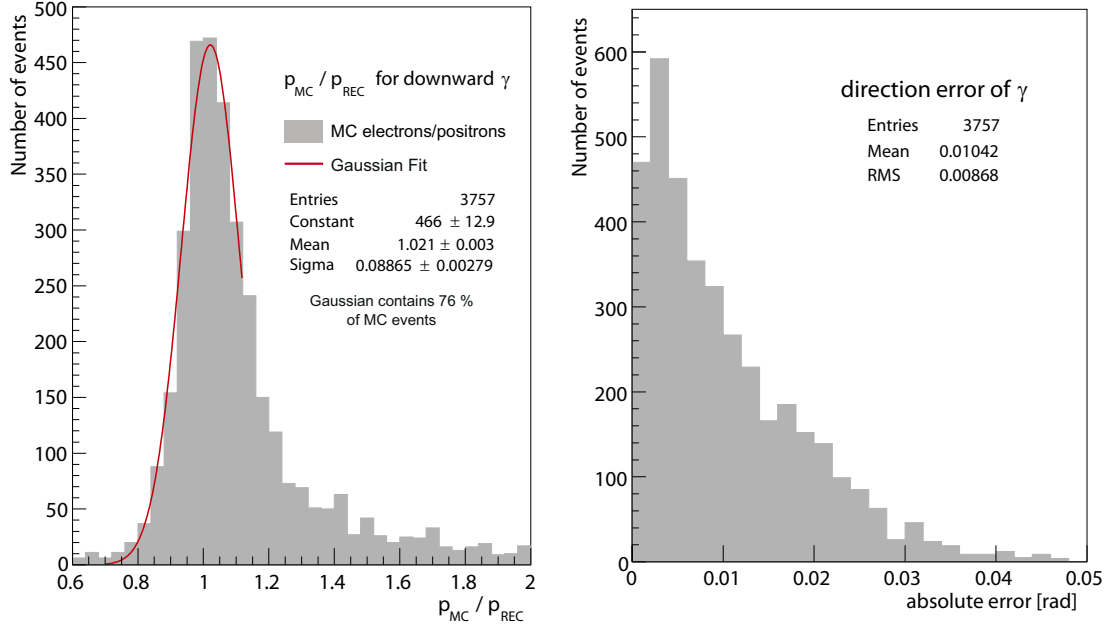


**Fig. 6.5:** Comparison of generated and reconstructed bremsstrahlung photon momentum (left) and the absolute error in its direction (right) for downward and upward going particles combined.

Figure 6.4 shows the ratio of generated and reconstructed momentum of converted bremsstrahlung events as the sum of the three track momenta for downward (left) and upward (right) going positrons. A Gaussian fit results in a momentum resolution of approximately 14 % and 15 % for the downward and upward case, respectively. This resolution is quite comparable to that for single-track events in the energy range of 10 GeV and above [131, 163], where the reconstruction algorithms have their peak sensitivity (see § 7.2).

The tails towards higher relative momenta are caused by additional bremsstrahlung photons which are emitted from the primary before it enters the tracking volume. If such a photon remains undetected, the measured momentum of the primary will be lower than the true initial momentum. This effect is especially apparent in the case of upward going particles due to the high amount of material they have to traverse before reaching the tracker.

As displayed in Figure 6.5, the properties of the bremsstrahlung photon can be particularly well reconstructed. A Gaussian fit to the photon's relative momentum results in a momentum resolution better than 9 %, while the absolute error in its direction has a standard deviation below 9 mrad. The secondary tracks from which the photon is reconstructed typically have lower momenta than the primary particle, resulting in a better momentum resolution. Additionally, in the case of the photon, the direction information of both secondary tracks enters into the reconstruction, thus increasing the resulting precision.

The spatial reconstruction of the vertices is rather poor due to the low angles under which the particles emerge from them. Figure 6.6 (left, middle) shows the absolute error of



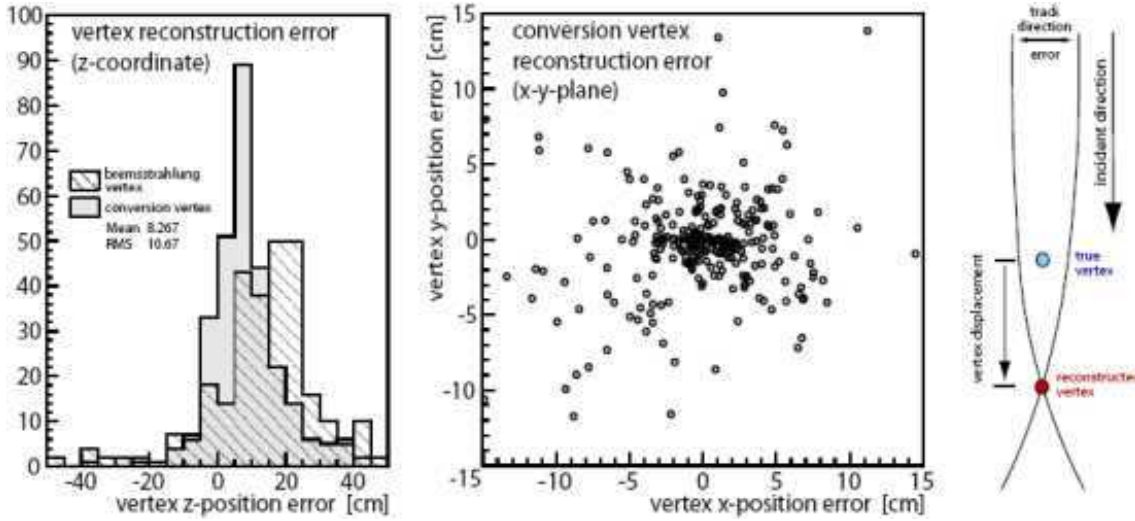


**Fig. 6.6:** Absolute vertex position reconstruction error  $z_{MC} - z_{rec}$  along the z-coordinate (*left*) and in the x-y-plane (*middle*), schematic view of the vertex finding in case of intersecting tracks (*right*).

the reconstructed vertex positions, calculated from downward going Monte Carlo electrons and positrons. For the conversion vertex, the resolution of the z-position is not better than 10 cm. Furthermore, a mean displacement of 8 cm is observed, i.e. the vertex is typically reconstructed too close to the center of the detector. The reason for this displacement lies in the geometrical characteristics of the vertex finding algorithm. As displayed in Figure 6.6 (*right*), small errors in the track directions may lead to intersecting tracks in the bending plane projection, always resulting in a vertex position which is shifted in the flight direction of the particle. For the same reasons, the bremsstrahlung vertex is reproduced with an accuracy of 16 cm and a displacement of about 13 cm in the flight direction. For the conversion vertex, the width of the error distribution in the x-y-plane (Figure 6.6, *middle*) is mostly a consequence of the z-errors when tracks are tilted with respect to the AMS-01 z-axis. Since the opening angles of the tracks vary only slightly with vertex position, the low quality of the vertex position reconstruction has almost no implications for the analysis.

## 6.4 Analysis

Analysis and suppression of background mainly rely on the evaluation of the topology and of the geometrical properties of the reconstructed events and are therefore based on data from the tracker. Additionally, cuts are applied on data from the TOF system. However, substantial parts of the analysis deal with measures to account for the environmental circumstances under which the AMS-01 experiment was operated, especially the effect of the geomagnetic field.

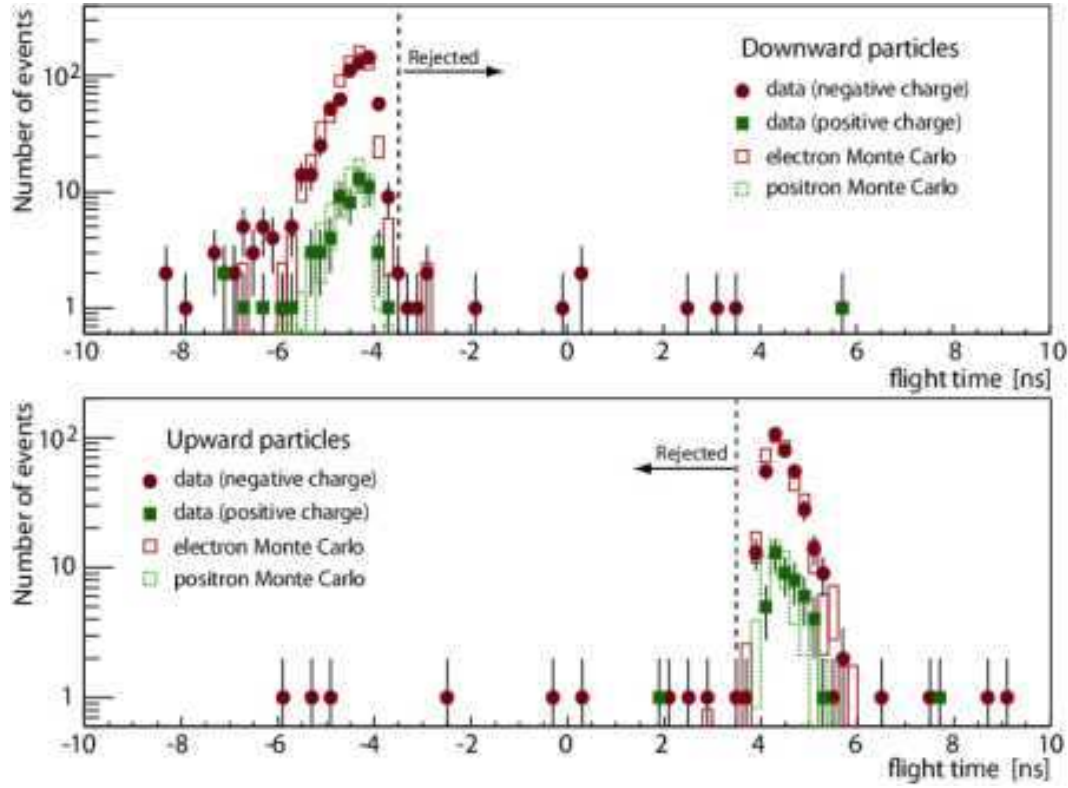


**Fig. 6.7:** Flight time along the z-axis measured with the TOF system for downward (*top*) and upward (*bottom*) going electron and positron candidates from data and Monte Carlo. The Monte Carlo distributions are scaled to the data by integral.

### 6.4.1 Basic Cuts

Several simple cuts are applied to the data in order to eliminate wrongly reconstructed events and a large portion of the background:

- As mentioned in § 6.3.2, the reconstruction of tracks with momenta lower than 100 MeV is not reliable. Tracks reconstructed with momenta below this value are tagged by the track fit algorithm and events containing them are rejected.
- Due to the deflection in the magnetic field and in conjunction with the small emission angles, the charge signs of the secondaries are exactly constrained depending on the direction of incidence. For downward going particles the left track is required to have positive charge sign, while the right track must be reconstructed with negative charge sign. For upward going particles, these requirements are reversed. Thus the charge sum of all three tracks must be  $\pm 1 e$ .
- With higher energies, the track momentum resolution and the signal over background ratio deteriorate. Thus the total reconstructed momentum must not exceed 50 GeV/c.

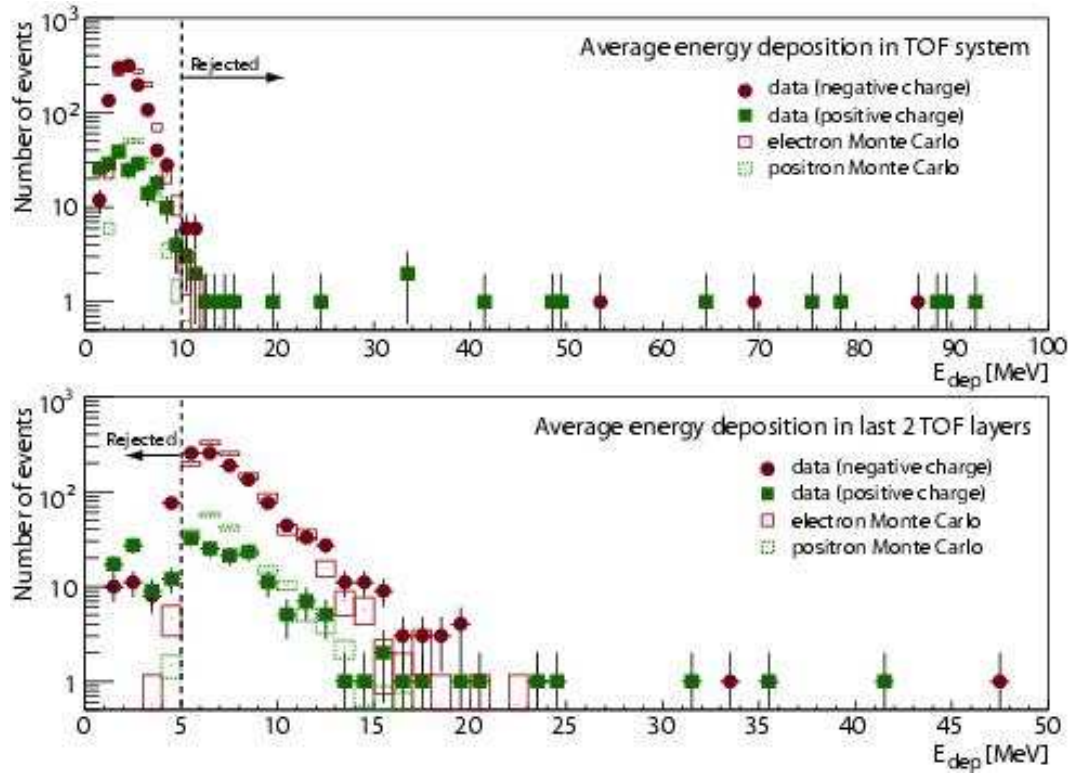


**Fig. 6.8:** Average energy deposition in the TOF scintillators (*top*) and average energy deposition in the last two TOF layers in flight direction (*bottom*) for data and Monte Carlo electron and positron candidates. The Monte Carlo distributions are scaled to the data by integral.

The requirement for increasing cluster distances within the seed triplets along the flight path (see § 6.3.2) largely distinguishes between downward and upward going particles. To make sure the flight direction is correctly recognized, timing information from the TOF system is used. Figure 6.7 shows the distributions of flight times  $t_f$  for downward and upward going particles calculated according to

$$t_f = (t_1 + t_2)/2 - t_3, \quad (6.6)$$

where the  $t_i$  denote the time of passage measured in TOF layer  $i$  ( $i$  is counted from top to bottom). Due to high voltage failures in TOF layer 4 [129], its timing information is not used. The sign of  $t_f$  in eq. (6.6) depends on the flight direction. If it is not compatible with the flight direction derived from the cluster topology, the event is rejected. The time needed by a particle with  $\beta \approx 1$  to pass the distance between the two TOF stations is about 4.3 ns. In rare cases particles are attributed flight times considerably smaller than this. The reason for these unphysical results is wrong reconstruction of the time of passage in the scintillators. To account for the uncertainty of the time measurements,  $|t_f|$  is required to be larger than 3.5 ns.

The energy loss  $E_{\text{dep}}$  in a TOF scintillator can be calculated with the Bethe-Bloch equation [164]. For an electron or positron in the momentum range 1 to 50 GeV/c it

amounts to about 2.5 MeV, with fluctuations of about 0.7 MeV [165]. Thus, to make sure that there are three particles traversing the detector, consistent with the signature of a converted bremsstrahlung photon, a minimum average energy loss is required in the last two TOF layers in the direction of flight. The distribution of this average is shown in Figure 6.8 (*bottom*). To account for the fluctuations of the energy loss, events with an average energy loss smaller than 5 MeV in the last two TOF layers in the direction of flight are rejected.

Apart from protons, nuclei such as He or N have been observed to induce background events through hadronic interactions in a few cases. Such particles with  $Z > 1$  deposit significantly more energy in the subdetectors than singly charged particles ( $E_{\text{dep}} > 8$  MeV for  $^4\text{He}$  in 1 cm scintillator). Thus they can be identified through the average energy deposition in all TOF scintillators. The energy loss of an individual particle, due to its stochastic nature, follows a Landau distribution [32], which exhibits a long tail towards higher values of  $E_{\text{dep}}$ . To account for this effect, the truncated mean of the energy deposition in the scintillators is calculated by omitting the highest value. Figure 6.8 (*top*) shows the distribution of this truncated mean. Events with a mean greater than 10 MeV are rejected.

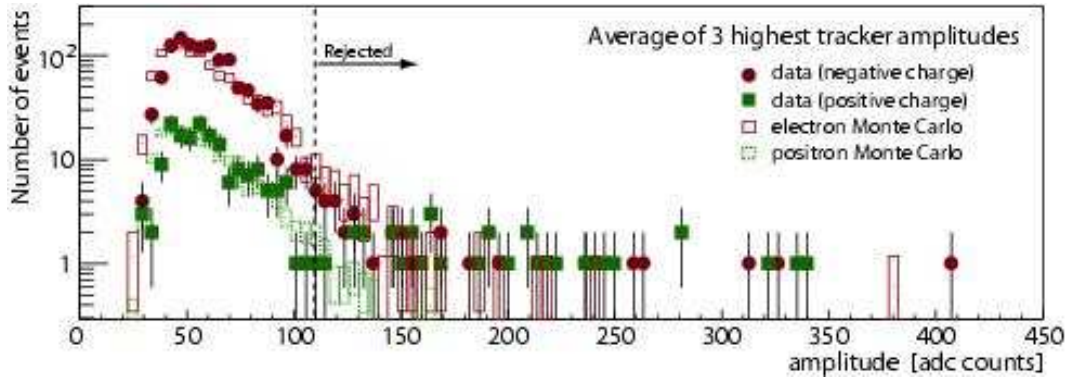


**Fig. 6.9:** Average of the three highest tracker hit amplitudes for data and Monte Carlo electron and positron candidates. The Monte Carlo distributions are scaled to the data by integral.

In addition to the TOF system, the energy deposition in the silicon strip detectors can be used to discriminate against particles with charge  $q > 1$ . The amplitudes of the hits in the tracker are given in ADC counts, thus the corresponding cut is determined from the electron data sample. In Figure 6.9 the distribution of the average of the three highest tracker hit amplitudes, regardless of the track to which they belong, is shown. The accumulation of positively charged events at higher amplitude is caused mostly by helium nuclei. Thus the average amplitude is required not to exceed 110 ADC counts. In case of negative total charge, the events at higher amplitude mostly result from wrongly reconstructed low momentum background protons.

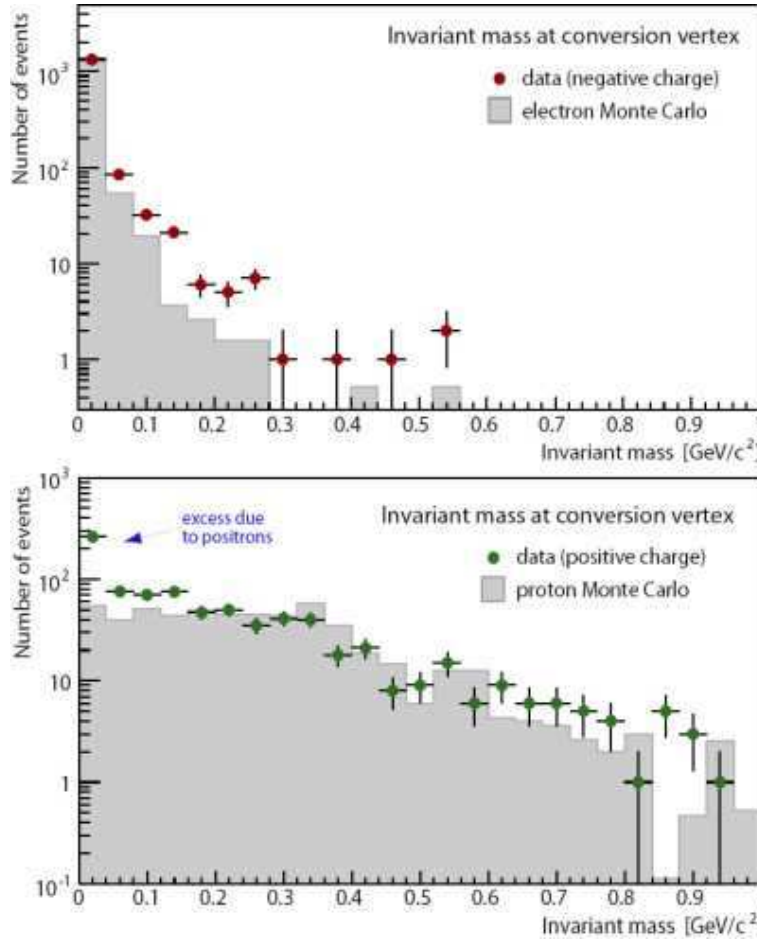


**Fig. 6.10:** The distribution of the invariant mass at the conversion vertex for data (*dots*) and Monte Carlo (*shaded histograms*): data events with negative total charge compared to electron Monte Carlo (*top*) and data events with positive total charge compared to proton Monte Carlo (*bottom*). The Monte Carlo distributions are scaled to the data by integral.

### 6.4.2 Suppression of Background

For the suppression of background, use is made of the fact that bremsstrahlung and photon conversion imply small opening angles of the particles at the vertices (see § 6.2.1), while in hadronic reactions the particles are emitted under large angles (see § 6.2.2). However, the latter are defined in the center-of-mass frame but observed in the laboratory frame, whose relative speed varies with the particles' incident momentum. Thus, in order to make the angles independent of the frame of reference, the corresponding invariant mass is calculated according to

$$m_{inv}^2 = 2 \cdot E_1 \cdot E_2 \cdot (1 - \cos \theta), \quad (6.7)$$

where  $\theta$ ,  $E_1$  and  $E_2$  denote the opening angle and the energies of the primary particle and the photon and of the conversion pair, respectively.



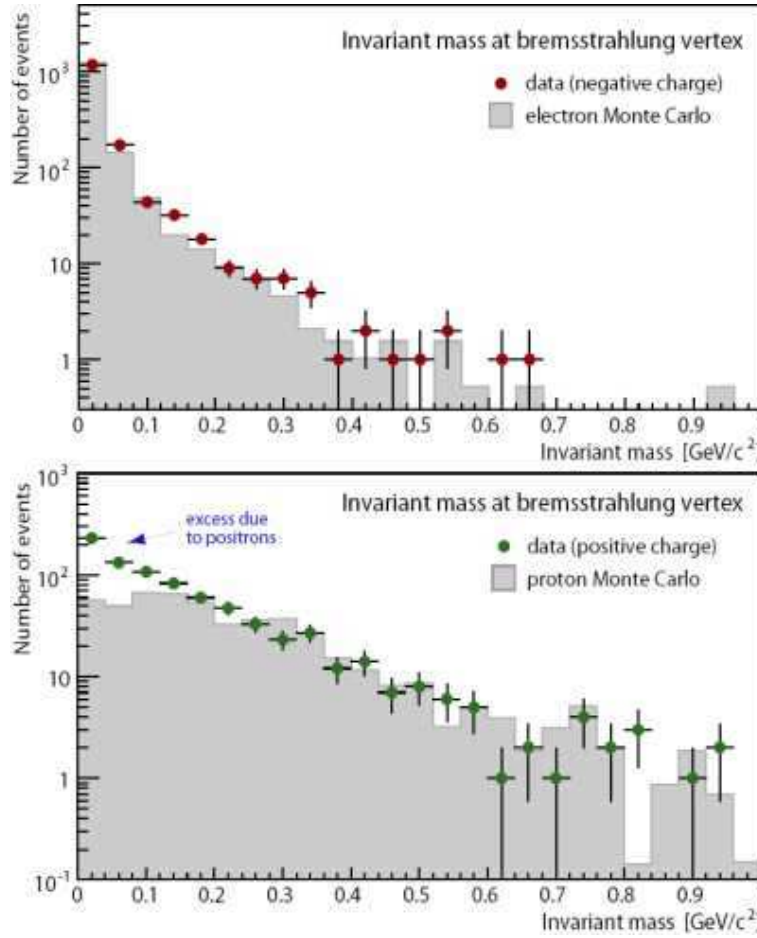


**Fig. 6.11:** The distribution of the invariant mass at the bremsstrahlung vertex for data (dots) and electron and proton Monte Carlo (shaded histograms): data events with negative total charge compared to electron Monte Carlo (top) and data events with positive total charge compared to proton Monte Carlo (bottom). The Monte Carlo distributions are scaled to the data by integral.

The distributions of invariant mass at the conversion and bremsstrahlung vertex are shown for data and electron and proton Monte Carlo in Figures 6.10 and 6.11. For events with negative total charge, which represent a largely clean electron sample, they reveal a narrow shape with a peak at zero. This is in agreement with Monte Carlo results. In case of events with positive total charge, consisting of positrons and background, the distributions also show a peak at zero, but have a long tail towards higher invariant masses which is largely caused by the proton background. The excess due to the positrons is clearly visible near zero invariant mass.

Figure 6.12 shows the distributions for data and for Monte Carlo proton and electron events in the invariant mass plane. In agreement with Monte Carlo, data events with negative total charge (electrons) accumulate around zero invariant masses. Caused by the positrons, such an accumulation is also observed in the distribution of positively charged events, where the uniformly distributed proton background indicated by the corresponding



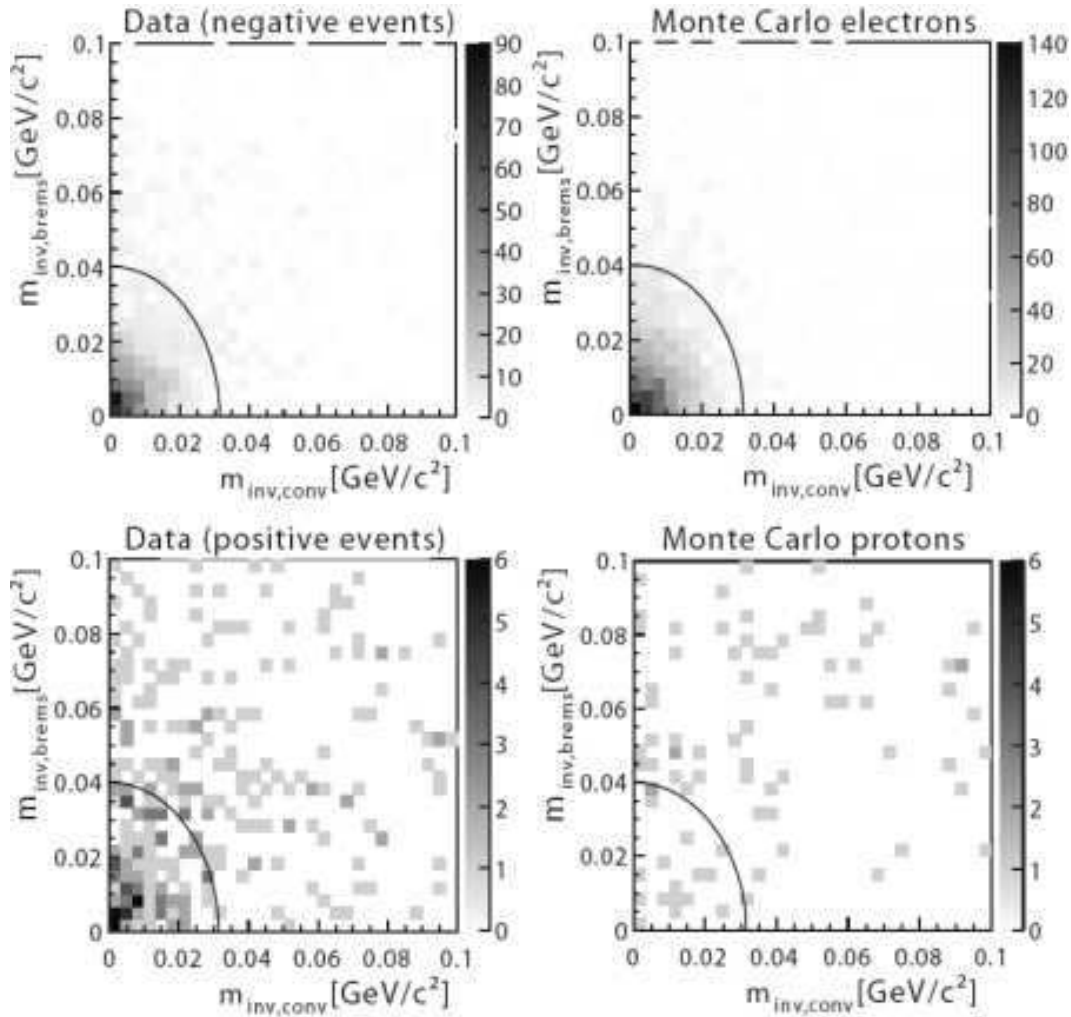


**Fig. 6.12:** Distributions in the invariant mass plane for data events with negative (*top left*) and positive (*bottom left*) total charge and for Monte Carlo electron (*top right*) and proton (*bottom right*) events.

Monte Carlo events is also seen. In order to discriminate against background events, restrictions are applied on the invariant masses. These cuts are parameterized as ellipses in the invariant mass plane, centered at zero and with half axes in units of the standard deviation of the respective distribution in the electron data sample. Events outside the ellipses are rejected. In order to keep the positron selection efficiency high, both cut values have been set to  $2\sigma$ .

### 6.4.3 Effect of the Mir Space Station

As stated in § 5.3, parts of the Mir space station were within the AMS-01 field of view during the four day Mir docking phase of the flight. Cosmic rays interacting with the Mir generated secondary particles [145], some of which may also have traversed the AMS-01 detector. Not being of cosmic origin, these secondaries must be rejected in the analysis.

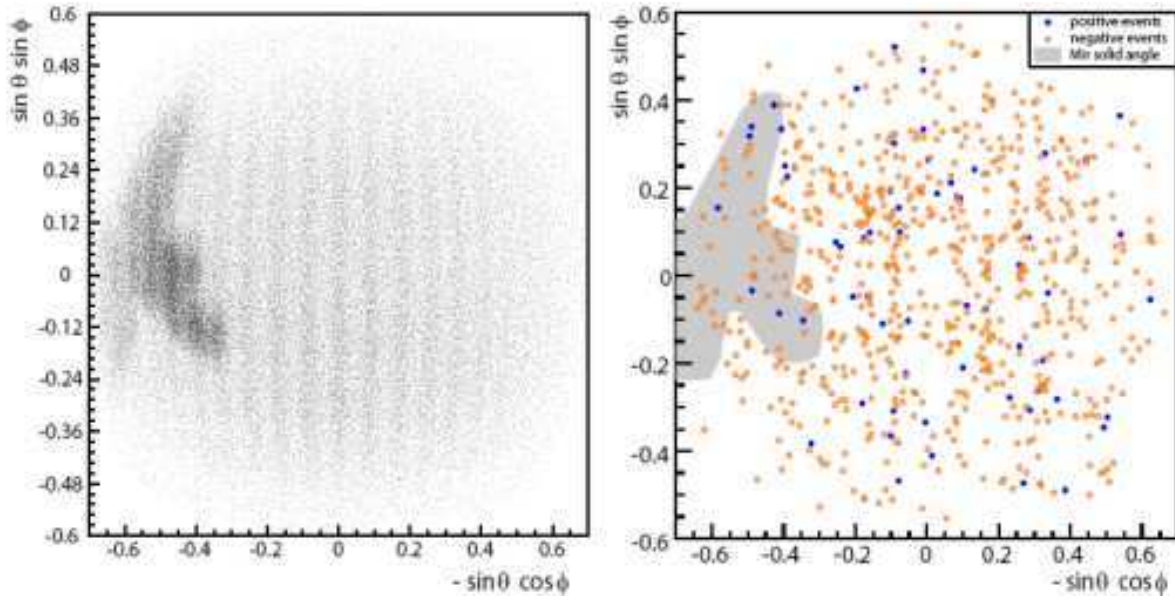


**Fig. 6.13:** Incoming directions projected on a x-y plane above the detector for downward going particles with  $Z = -1$  recorded during the Mir docking phase. The vertical stripes are due to reconstruction artifacts (*left*) [145]; the same display for downward going electron and positron candidates from this analysis; also indicated is the solid angle obstructed by the Mir (*right*).

Figure 6.13 (*left*) displays the incoming directions of downward going particles with  $Z = -1$ , projected on an x-y-plane above the detector, which were recorded during the Mir docking period [145].  $\theta$  and  $\phi$  denote the polar and azimuthal angles of the incoming particles. There is an apparent excess of particles in a clearly defined area on the left side of the plot. It has been shown [145] that these excess particles originated in the Mir and were mostly spallation pions and muons from their decay. Hence, since electrons and positrons can also result from pion decay, the Mir must be regarded as a possible background source.

In Figure 6.13 (*right*), the same display is shown for downward going electron and positron candidates from this analysis, together with the solid angle obstructed by the Mir. No significant excess of particles is observed in the affected solid angle. However, particles in the Mir solid angle that were recorded during the docking phase were not considered in this analysis.

#### 6.4.4 Geomagnetic Cutoff

Energy spectra of cosmic rays are modulated by the geomagnetic field (see § 4.3). Depending on the direction of incidence and the geomagnetic coordinates of the entry point into the magnetosphere, particles with momenta below a certain cutoff are deflected by the magnetic field and cannot reach the Earth's proximity. Hence, below geomagnetic cutoff the particles detected by AMS-01 must originate from within the magnetosphere.

They were mostly produced as secondaries through hadronic interactions and trapped inside the Earth's radiation belts.

To discriminate against these secondaries, particle trajectories were individually traced back from their measured point of incidence, angle and momentum through the geomagnetic field by numerical integration of the equation of motion using an enhanced Runge-Kutta iteration procedure [166]. For this purpose, a reference model of the Earth's external field [167] was used in combination with the IGRF-6 coefficients [168] of the internal field according to eq. (4.6).

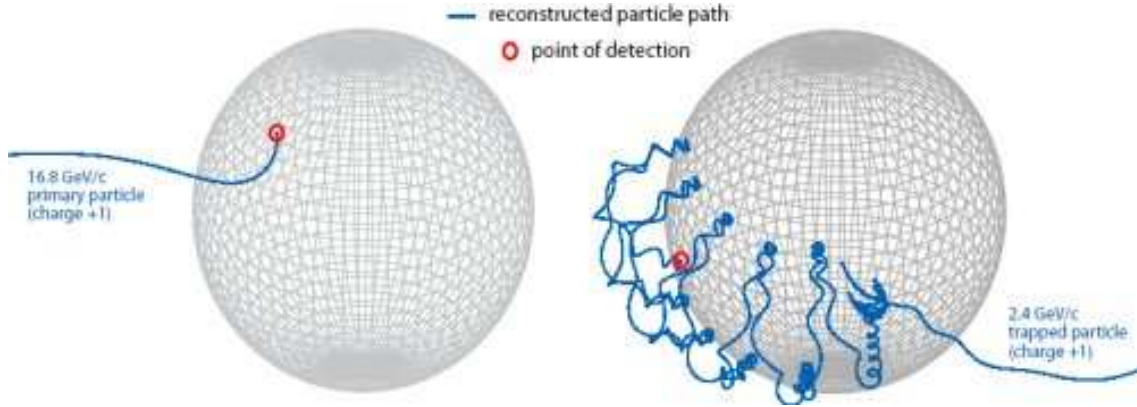


**Fig. 6.14:** Reconstructed paths of positron candidates in the Earth's magnetic field. The left display shows a 16.8 GeV/c primary particle, the right one a 2.4 GeV/c trapped particle which is rejected as being of secondary origin.

Figure 6.14 illustrates the flight paths of particles with charge  $+1e$  by means of two examples. The left display shows the reconstructed path of a particle with a momentum of 16.8 GeV/c, as it approached the Earth from outside the magnetosphere and was detected by the AMS-01 experiment over central Northern America. Apparently, this particle is of extraterrestrial origin and thus accepted for further analysis. On the right side of Figure 6.14, the path of a trapped secondary particle with 2.4 GeV/c momentum is shown which exhibits the typical superposition of a helix trajectory with hemisphere bouncing and westward drift. It is certain that this particle stems from an interaction with the atmosphere near one of the numerous turning points of its trajectory, thus the early part of the displayed path is purely hypothetical. Consequently, the particle is not considered in the analysis. In general, particles are rejected as secondaries if their trajectory touched the surface of the Earth at least once. Particles always staying within a distance of 25 Earth radii or not crossing the magnetopause are considered as trapped and are also rejected.

## 6.5 Correction for Irreducible Background

As seen in Figure 6.12, the distribution of protons in the invariant mass space does not vanish in the signal region around zero invariant mass. The same applies to the background from wrongly reconstructed electrons. Consequently, a small fraction of back-

ground events will not be rejected by the cut on the invariant masses. This remaining irreducible background has to be corrected for, which is accomplished by using Monte Carlo data.

In principle the approach is to run the analysis on an adequate number of proton and electron Monte Carlo events as if they were data, determine the amount and momentum distribution of particles that are misidentified as positrons, and subtract these from the raw positron counts obtained from data. However, such an implicit comparison of Monte Carlo and data requires the adjustment of several properties of the simulated events, which have not been affected by the geomagnetic field and whose input spectrum is not exactly equal to the true fluxes.

As discussed in § 6.4, the geomagnetic field shields the Earth's vicinity from low energy particles. However, the geomagnetic cutoff cannot be calculated individually for Monte Carlo particles, since their four vector is not defined with respect to the geomagnetic coordinates. To correct for the shielding effect, the livetime function  $T(p)$ , described in § 7.2 and shown in Figure 7.6, is used. The livetime function gives the effective measurement time as a function of momentum for singly charged particles. After normalization to a maximum value of 1, resulting in the function  $\hat{T}(p)$ , its value at a given momentum denotes the probability for a singly charged particle to penetrate the geomagnetic field. Hence, it serves as a weight for distributions of any event variable in Monte Carlo, particularly for the momentum distribution of Monte Carlo background events. The livetime function must be evaluated using the reconstructed momentum of the incident particle to treat Monte Carlo and real data on an equal footing.

The incident momentum spectrum of the Monte Carlo particles follows a distribution  $\phi_{MC}(p) = p^{-1}$  and therefore differs significantly from the true spectra which have spectral indices between 2.7 and 3.4 and are affected by solar modulation. Therefore, the Monte Carlo event variables have to be reweighted, since they are correlated with the incident momentum. Using the parameterized flux  $\phi_D(p)$  of protons measured by AMS-01 [46], the spectral reweighting function  $w(p)$  is calculated as  $w(p) = \phi_D(p)/\phi_{MC}(p)$ . In contrast to  $\hat{T}(p)$ ,  $w(p)$  must be evaluated using the incident particle's simulated momentum and is not normalized.

The livetime function as well as the spectral reweighting function are then applied as weights in histogramming an event variable  $x$  from the proton Monte Carlo sample, meaning that  $w(p_s) \cdot \hat{T}(p_r) \cdot x$  is histogrammed instead of  $x$ , with the simulated momentum  $p_s$  and the reconstructed momentum  $p_r$ . In particular, the functions correct for the shape of the momentum distribution of background protons calculated from Monte Carlo. Subsequently, since  $w(p)$  is not normalized, the background distribution must be scaled to the data to obtain the total number of background events to be subtracted from the measured number of positrons.

Figure 6.15 illustrates the scaling of the proton Monte Carlo to the positively charged data events using the sidebands of the invariant mass distributions. The sidebands are defined as the ranges of invariant mass above certain thresholds in which the positron contribution to the data is negligible. The thresholds are determined from the electron distribution, which is identical to that of positrons. They are set to 0.16 GeV/c<sup>2</sup> for the conversion vertex and to 0.2 GeV/c<sup>2</sup> for the bremsstrahlung vertex. The excess in the data due to the positron contribution is apparent below threshold. Two scaling factors, one

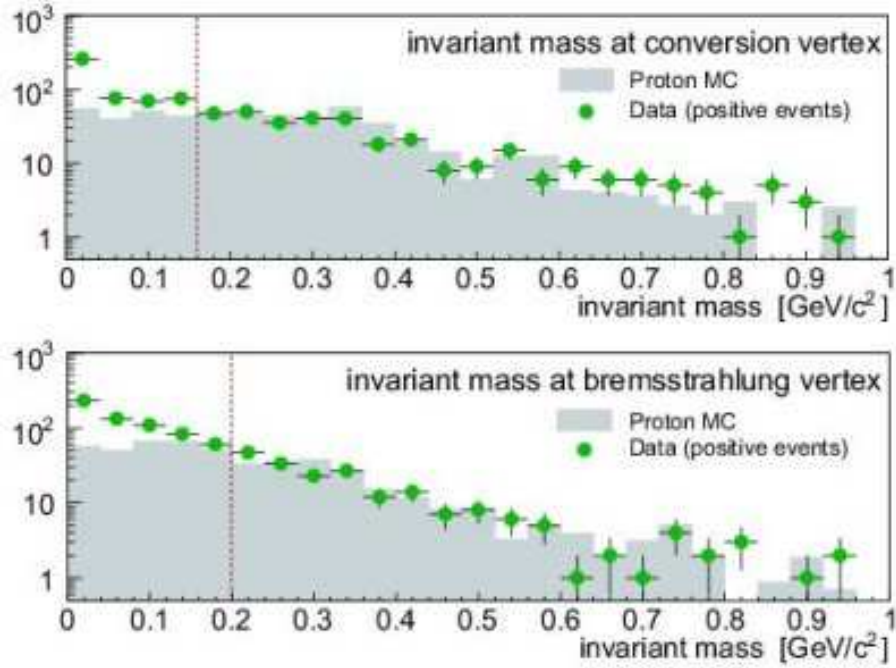


**Fig. 6.15:** Invariant mass distributions at the conversion (*top*) and bremsstrahlung vertex (*bottom*) for positively charged events from data and proton Monte Carlo. The Monte Carlo distributions have been scaled to the data using the sidebands whose borders are indicated by the vertical lines.

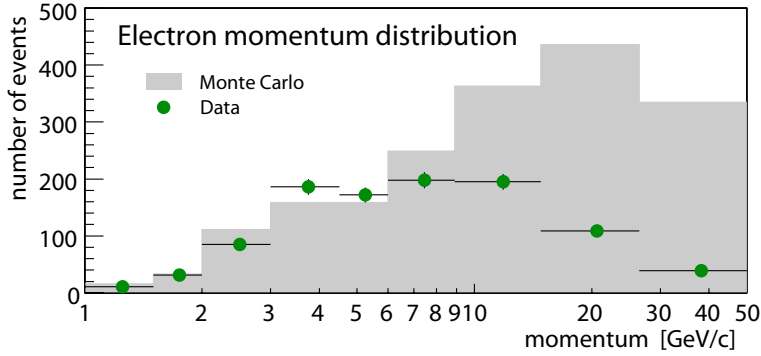


**Fig. 6.16:** Distribution of the reconstructed momentum of electrons from data and Monte Carlo. The latter have been corrected for the livetime  $\hat{T}(p)$  but not for the distribution of momentum.

from each of the distributions at the two vertices, are determined as the sideband ratios of the number of events from data and Monte Carlo. The average of these two factors, which differ less than 8 % from each other, is then applied to the reweighted Monte Carlo proton background distribution, resulting in the final proton background correction.

In contrast to protons, the electron data sample is clean, without contamination from other particles. Therefore, it can be used directly to reweight the spectrum of the electron



Monte Carlo events in order to estimate the background in the positron data resulting from wrongly reconstructed electrons. Figure 6.16 shows the distributions  $D_{e^-,d}(p)$  and  $D_{e^-,mc}(p)$  of the measured momenta of electrons from data and Monte Carlo respectively, where the latter have been weighted with the normalized livetime function  $\hat{T}(p)$ . In a first step, the electrons from Monte Carlo that have been wrongly reconstructed as positrons are grouped in nine bins according to their simulated momentum following the binning in Figure 6.16. For each group, the distribution of measured momenta is separately histogrammed. Finally, each of these histograms is scaled with the ratio  $D_{e^-,d}/D_{e^-,mc}$  in the respective bins. The sum of the nine resulting histograms then gives the amount and distribution of electron background events to be subtracted from the positron sample.

In total, 1026 electrons and 119 positrons have been found prior to the background correction in this analysis. Figure 6.17 shows the momentum distribution of the uncorrected positron sample and the total background correction as a function of momentum, itemized into contributions from protons and wrongly reconstructed electrons, which amount to 24.9 and 6.4 events, respectively.

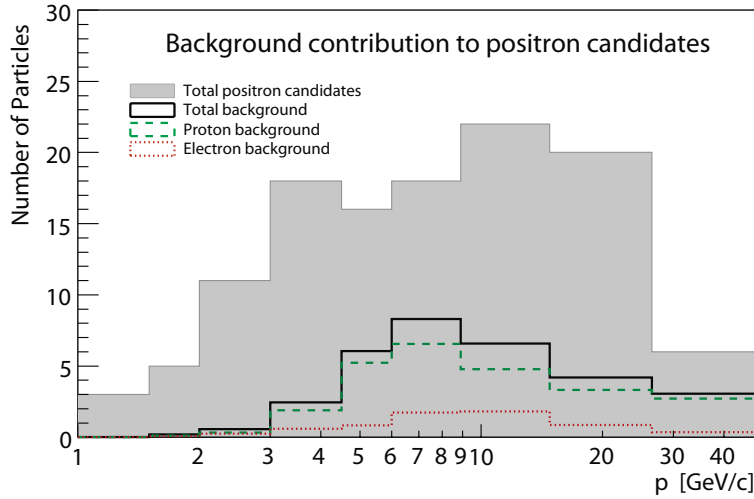


**Fig. 6.17:** Momentum distribution of positron candidates including background, and the background contribution from protons and wrongly reconstructed electrons.



## 7 Results of the Positron Measurement

### 7.1 Positron Fraction

The positron fraction  $e^+/(e^+ + e^-)$  is calculated from the electron and corrected positron counts for each momentum bin. It is shown in Figure 7.1 and compared with earlier results and with a model calculation based on purely secondary positron production. Table 7.1 summarizes the results of this analysis. The contributions to the error on the positron fraction are discussed in the following.

momentum GeV/c	range GeV/c	$n_{e^-}$	$n_{e^+,r}$	$n_{e^+,c}$	positron fraction	$\sigma_{\text{stat}}$	$\sigma_{\text{sys},b}$	$\sigma_{\text{sys},a}$
1.25	1–1.5	11	3	3	0.21	$^{+0.11}_{-0.1}$	$\pm 0$	$\pm 0$
1.75	1.5–2	31	5	4.8	0.133	$^{+0.064}_{-0.051}$	$^{+0.002}_{-0}$	$\pm 0.006$
2.5	2–3	85	11	10.7	0.112	$^{+0.034}_{-0.031}$	$^{+0.001}_{-0.003}$	$\pm 0.004$
3.75	3–4.5	186	18	15.8	0.078	$^{+0.021}_{-0.018}$	$^{+0.001}_{-0.003}$	$\pm 0.004$
5.25	4.5–6	172	16	10	0.055	$^{+0.025}_{-0.022}$	$^{+0.006}_{-0.007}$	$\pm 0.001$
7.45	6–8.9	198	18	9	0.043	$^{+0.029}_{-0.017}$	$^{+0.01}_{-0.004}$	$\pm 0.004$
11.9	8.9–14.8	195	22	14.5	0.069	$^{+0.03}_{-0.014}$	$^{+0.01}_{-0.002}$	$\pm 0.006$
20.6	14.8–26.5	109	20	15.4	0.124	$^{+0.038}_{-0.03}$	$^{+0.009}_{-0.003}$	$\pm 0.007$
38.2	26.5–50	39	6	2.9	0.07	$^{+0.075}_{-0.034}$	$^{+0.01}_{-0.01}$	$\pm 0.007$

**Tab. 7.1:** The positron fraction and its momentum dependence.  $n_{e^-}$ ,  $n_{e^+,r}$  and  $n_{e^+,c}$  denote the number of electrons, raw (uncorrected) and corrected positrons, respectively. The last three columns give the statistical errors  $\sigma_{\text{stat}}$  and the systematic errors  $\sigma_{\text{sys},b}$  and  $\sigma_{\text{sys},a}$  due to background and acceptance correction.

#### 7.1.1 Statistical Errors

Due to the complexity of the positron fraction analysis, having two sources of irreducible background and low statistics, a Bayesian approach based on Monte Carlo simulation has been chosen for the determination of the statistical errors [169, 170]. The aim is to obtain the probability distribution of all possible values of the positron fraction which, together with the background, can lead to the observed number of particle counts. Given this distribution, the confidence intervals are derived by numerical integration. The Monte

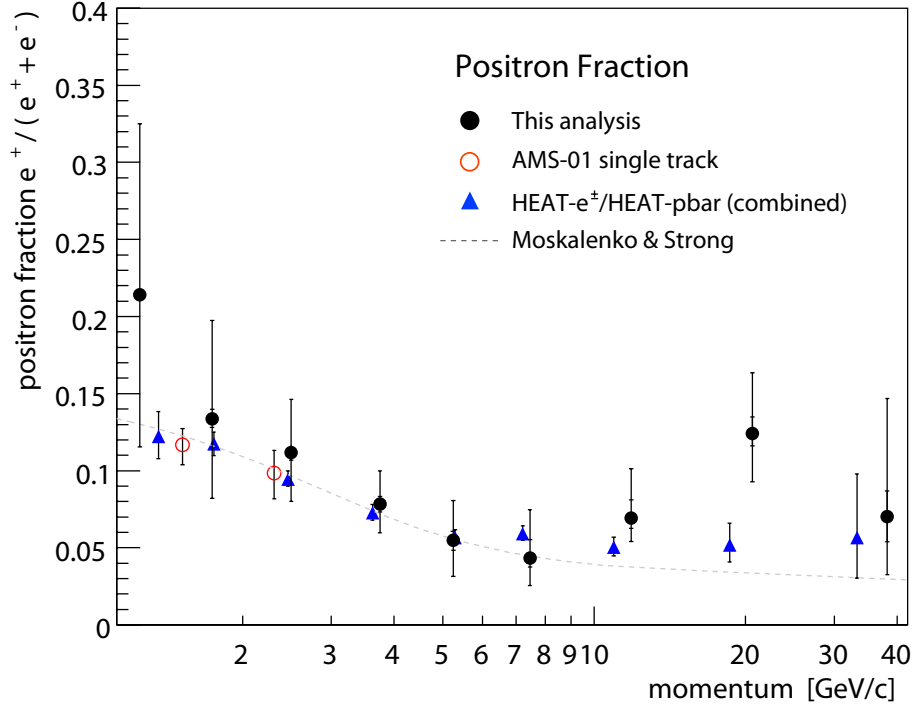


**Fig. 7.1:** The positron fraction  $e^+/(e^+ + e^-)$  measured in this analysis, compared with earlier results from AMS-01 [2], the combined results from HEAT- $e^\pm$  and HEAT-pbar [7] and with a model calculation for purely secondary positron production [111] (dashed line). The overall errors are given by the outer error bars, while the inner bars represent the systematic contributions  $\sigma_{\text{sys}}$  to the error.

Carlo procedure outlined below is carried out separately for each of the momentum bins defined in Table 7.1.

- In a first step, two random floating point numbers  $S_{e^-, \text{true}}$  and  $S_{e^+, \text{true}}$  are generated by sampling a uniform distribution. They represent the expectation values for the probability distributions of “true” numbers of electrons and positrons without background.
- Subsequently, the number of background events are added to  $S_{e^+, \text{true}}$ . The corrected and scaled background counts  $B_p$  and  $B_{e^-}$  from proton and electron Monte Carlo, as displayed in Figure 6.17, are the result of a counting experiment and therefore have statistical uncertainties, which transform into systematic errors when added to the “true” signal. These errors follow Poisson distributions, whose expectation values are, to best knowledge, assumed to be equal to  $B_p$  and  $B_{e^-}$ . Hence, to account for their uncertainty,  $B_p$  and  $B_{e^-}$  are smeared according to the individual distributions before adding them to  $S_{e^+, \text{true}}$ . However, the width of the Poisson distributions is determined by the statistics of the raw number of Monte Carlo background events considered and not by  $B_p$  and  $B_{e^-}$ , which are the result of correcting and scaling the raw counts to the data. As a consequence, the raw Poisson width is altered by the

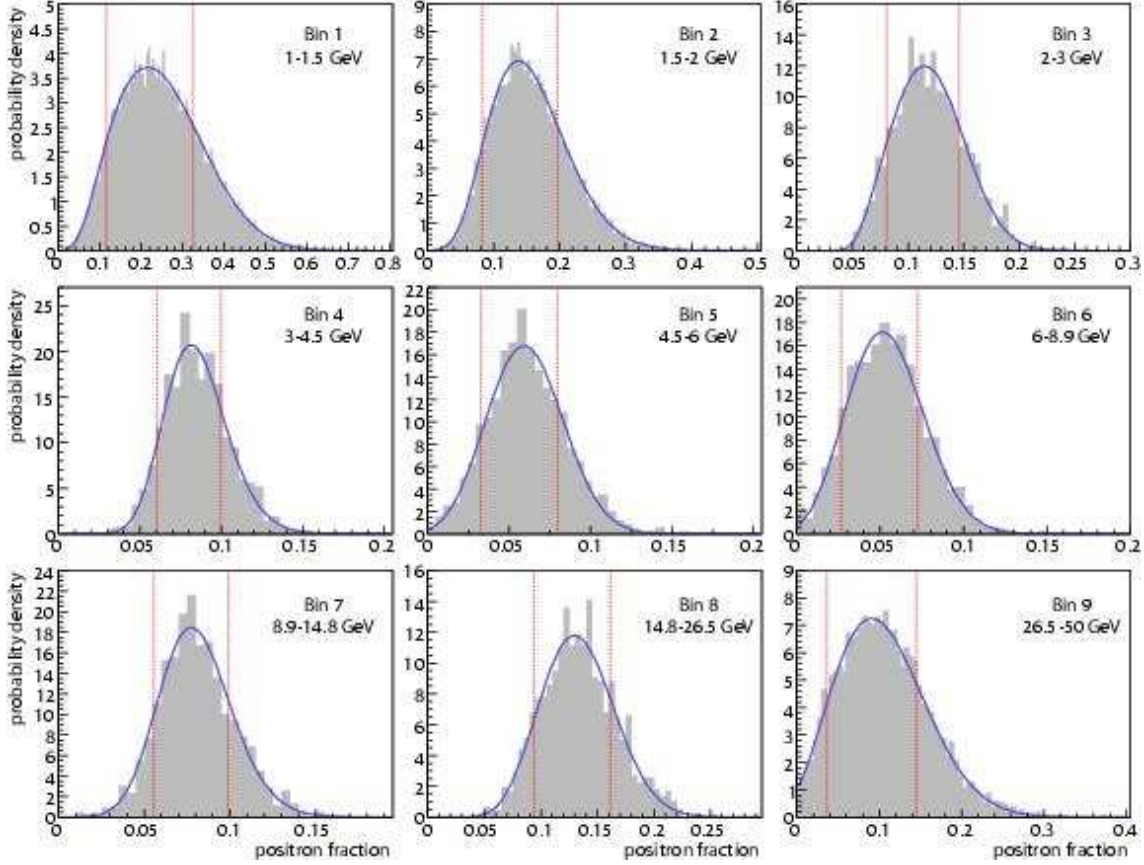


**Fig. 7.2:** The normalized simulated distributions of the positron fraction  $f_{\text{true}}$  (shaded histograms), the fitted functions  $D_f$  (blue solid lines), and the resulting confidence interval limits (red dashed lines) for each of the nine momentum bins.

corresponding scale factor. To account for this effect, the raw background counts are first smeared according to their respective Poisson distribution and then multiplied with the ratio of corrected to raw counts. The resulting numbers of background events are denoted by  $\hat{B}_p$  and  $\hat{B}_{e^-}$ .

- The background counts thus obtained are added to the true number of positrons, resulting in an expectation value  $T_+ = S_{e^+, \text{true}} + \hat{B}_p + \hat{B}_{e^-}$  for the measured total number of positively charged particles. On the other hand, the electron sample is largely background-free and  $T_- = S_{e^-, \text{true}}$ .
- Two integer random numbers  $N_+$  and  $N_-$  are finally generated according to Poisson distributions with expectation values  $T_+$  and  $T_-$ , respectively. These represent one simulated measurement of the number of positron and electron candidates including background. If  $N_+$  and  $N_-$  are exactly equal to the counts actually observed in the experiment, the “true” positron fraction  $f_{\text{true}} = S_{e^+, \text{true}} / (S_{e^+, \text{true}} + S_{e^-, \text{true}})$  is accepted for further analysis, and the whole procedure is repeated.

Figure 7.2 shows the distributions of the simulated positron fraction  $f_{\text{true}}$  for each of the nine momentum bins. Normalized to an integral of 1, they represent the probability density functions of the positron fraction measured in this analysis, taking into consideration the amount of background calculated from Monte Carlo. As apparent in the figure, the distributions are in all cases parameterized well by a function  $D_f = G(f) \cdot L(f)$ , the product of a Gaussian and a Landau distribution function  $G(f)$  and  $L(f)$ , respectively. The slight asymmetries, which become manifest in the tails towards higher values of  $f_{\text{true}}$  and make the Landau function  $L(f)$  necessary, are due to the statistical uncertainty of the background correction.

By numerical integration, the smallest interval is found over which the integral of the function  $D_f$  equals 0.683, yielding the lower and upper limits of the corresponding  $1\sigma$  Gaussian confidence intervals for the appropriate momentum bin. These limits are stated as the statistical errors on the positron fraction and are given in Table 7.1.

### 7.1.2 Systematic Errors

Since the positron fraction is a ratio of particle fluxes, most sources of systematic error such as detector acceptance or trigger efficiency naturally cancel out. The only sources of error that must be considered are those which are asymmetric with respect to the particle charge.

The background correction is applied to the sample of positron candidates only and is therefore a source of systematic error. To a certain degree, the description of the experimental setup may be inaccurately implemented in the Monte Carlo program. Furthermore, in contrast to the production of charged pions, background processes involving neutral pion production imply photoconversion with typically low angles between tracks emerging from the vertices. Hence, the distribution of invariant masses depends on the angular cross sections of charged and neutral pion production. Possible inaccuracies in the implementation of the cross sections in the Monte Carlo program must therefore be considered.

The systematic error  $\sigma_{\text{sys,b}}$  from the background correction can be estimated by evaluating the mean deviation of the scaled Monte Carlo background from the data in the invariant mass plane. Figure 7.3 shows the number density of positively charged particles from data  $n_{\text{data}}$  (*left*) and Monte Carlo protons  $n_{\text{mc}}$  (*middle*) in the region of invariant masses  $m_{\text{inv}} > 0.33 \text{ GeV}/c^2$  at both vertices where the positron signal is negligible. The Monte Carlo proton histogram has been scaled to the data using the ratio  $\sum n_{\text{data}} / \sum n_{\text{mc}}$  in the bins outside the signal region. The histogram in the right panel of Figure 7.3 shows the distribution of relative differences  $\delta_r$  of data and Monte Carlo bin contents given by

$$\delta_r = w \cdot \frac{n_{\text{data}} - n_{\text{mc}}}{n_{\text{mc}}} \quad (7.1)$$

for  $n_{\text{mc}} \neq 0$  with weights  $w$ . Although the binning has been chosen rather coarse to minimize statistical fluctuations, the remaining statistical uncertainty is accounted for by weighting each entry with the inverse of the relative statistical error  $w = n_t / \sigma_t$  with  $w \approx \sqrt{n_t}$  in the Poisson limit and  $n_t = (n_{\text{data}} + n_{\text{mc}})/2$ . Finally, for display purposes,  $\delta_r$  has been scaled to a maximum value of 1. The RMS deviation of  $\delta_r$  leads to a systematic

error estimate of about 20 % of the background events. This value is then propagated to the positron fraction for each momentum bin, resulting in the asymmetric values of  $\sigma_{\text{sys},b}$  as given in Table 7.1. No separate systematic error for the background from wrongly reconstructed electrons is calculated, since their contribution to the total background is small compared to that from protons.

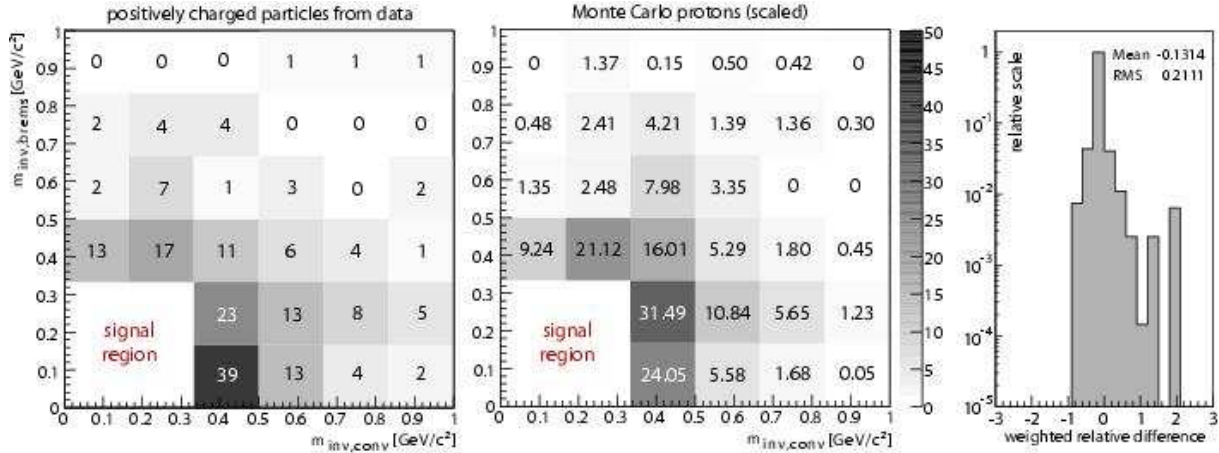


**Fig. 7.3:** The distribution of particles in the invariant mass space outside the positron signal region for positively charged particles from data (*left*) and scaled Monte Carlo protons (*middle*). The numbers in the histograms denote the particle counts in the respective bins; the distribution of the weighted relative difference of the background in data and Monte Carlo (*right*).

As a consequence of the East West Effect [171], in combination with the asymmetric layout of the AMS-01 tracker, the product of the detector acceptance and the livetime as functions of the direction of incidence of a particle may vary for positrons and electrons, though no deviation of their average livetimes is apparent (see section 7.2). This effect is accounted for with a second contribution  $\sigma_{\text{sys},a}$  to the systematic error of the positron fraction. It is estimated from the mean variation of the difference in livetime of positrons and electrons over the detector acceptance. After propagation to the positron fraction, the systematic error due to the East West Effect is well below 10 % for all momentum bins, except for the highest momenta above 26 GeV, where it amounts to approximately 14 % of the positron fraction value.

The total errors  $\sigma_{\text{tot}}$  displayed in Figure 7.1 are calculated according to  $\sigma_{\text{tot}}^2 = \sigma_{\text{stat}}^2 + \sigma_{\text{sys},b}^2 + \sigma_{\text{sys},a}^2$ , separately for the upper and lower ranges. Similarly, the systematic contribution  $\sigma_{\text{sys}}$  to the total error is given by  $\sigma_{\text{sys}}^2 = \sigma_{\text{sys},b}^2 + \sigma_{\text{sys},a}^2$ . Clearly, the accuracy of the positron fraction is statistically limited by the small number of particle counts.

### 7.1.3 Variation of the Positron Fraction with the Value of the Cut

Figure 7.4 shows the average positron fraction and its total error  $\sigma_{\text{tot}}$  as a function of the invariant mass cut parameter (see § 6.4). The fraction is calculated as the weighted mean over the six momentum bins from 3 to 50 GeV/c, which have been corrected for a considerable amount of background, with the total errors  $\sigma_{\text{tot}}$  as weights. For values of the cut

between approximately  $1.5\sigma$  and  $2.5\sigma$ , the mean positron fraction remains largely stable, showing that the background correction procedure compensates well for the additional background events entering the positron sample when the cut is loosened. Beyond  $2.5\sigma$ , the average positron fraction rises constantly, probably due to systematic uncertainties of the background correction. However, the cut of  $2\sigma$  used in this analysis, indicated by the vertical line in Figure 7.4, is well within the region in which the background correction procedure works reliably.

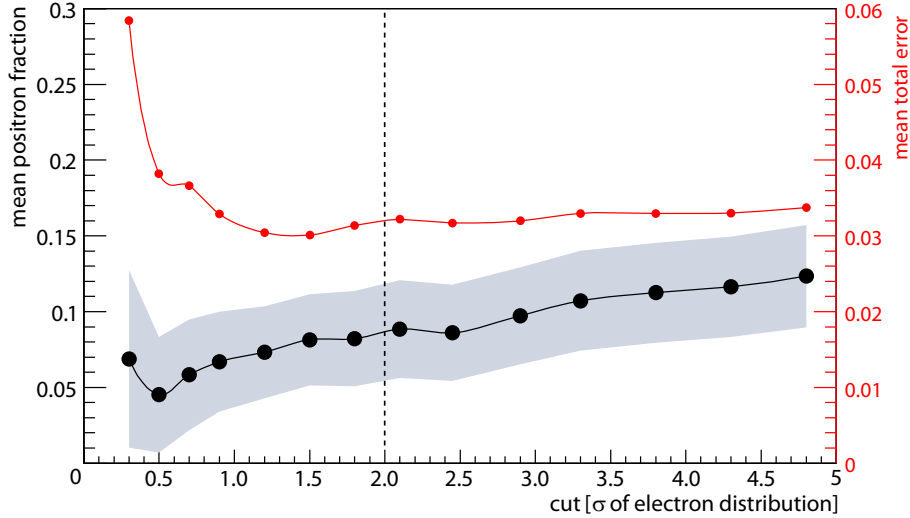


**Fig. 7.4:** Average value of the positron fraction (*large dots*) and its total error (*small dots and shaded area*) as functions of the cut parameter. The actual cut is indicated by the vertical line.

## 7.2 Flux Calculation

As a crosscheck to the measurement of the positron fraction, the absolute incident fluxes of electrons and positrons are calculated. The electron flux is then compared to measurements by other experiments and to the results obtained previously by AMS-01. To calculate the fluxes it is necessary to determine the acceptance as well as the livetime for positrons and electrons in the context of this analysis.

The term *livetime* means the effective amount of time during which cosmic ray particles coming from outer space have the opportunity to reach and trigger the experiment. The livetime may be significantly lower than the total operation time of the experiment, a fact for which four different effects are largely responsible. First, due to a variety of reasons, there were several loss-of-signal periods during the flight with average duration of roughly one hundred seconds and these must be subtracted from the total operating time. Furthermore, the total time during which the trigger system was busy (see § 5.2) must also be considered as dead time.

Besides these rather simple effects, the influence of the Earth and its magnetic field causes the livetime to be reduced even in a momentum dependent way. The body of the



Earth will obstruct particles arriving from the “wrong” side, except if their momentum is low enough so that their trajectories may be bent around the Earth by the geomagnetic field. In addition the geomagnetic field will force the trajectories of incoming particles on a helix and capture or shield the Earth from particles with momentum below the geomagnetic cutoff. These effects depend on the direction of incidence and on the momentum of the particle, as well as on the orientation and position of the Space Shuttle, and therefore on time. In principle, this means that the experiment may be effectively shut down for the measurement of particles in a certain momentum range at a given time.

From the particle count  $N(p, \theta, \phi)$  in a particular momentum bin  $p$  of width  $\Delta p$  and knowing the detector acceptance  $A(p, \theta, \phi)$ , and the livetime  $T(p, \theta, \phi)$ , one can calculate the differential flux as follows:

$$\frac{d\Phi(p, \theta, \phi)}{dp} = \frac{N(p, \theta, \phi)}{A(p, \theta, \phi) \cdot T(p, \theta, \phi) \cdot \Delta p}. \quad (7.2)$$

If – as is the case with the flux of downward going particles in AMS-01 – the livetime is only weakly dependent on direction, the angular distribution of the particle count will follow that of the acceptance. Then, one can approximate eq. (7.2) by

$$\frac{d\Phi(p)}{dp} = \frac{N(p)}{A(p) \cdot T(p) \cdot \Delta p}. \quad (7.3)$$

The determination of the detector acceptance and the calculation of the livetime is described in the following two sections.

### 7.2.1 Detector Acceptance

The detector acceptance for the bremsstrahlung conversion process is calculated from Monte Carlo, separately for downward and upward going electrons and positrons. In the Monte Carlo simulation, particles are emitted above or below the detector from a square surface  $S$  with a side length of 3.9 m. With  $n_t$  the total number of particles emitted from  $S$  into the hemisphere facing the detector with an isotropic angular distribution, and  $n_c$  the number of reconstructed events remaining after all cuts, the acceptance as a function of incident momentum is [172]

$$A(p) = S \cdot \pi \cdot \frac{n_c(p)}{n_t(p)}. \quad (7.4)$$

Figure 7.5 shows  $A(p)$  separately for upward or downward going electrons and positrons. It is of the order of a few  $\text{cm}^2 \cdot \text{sr}$  and reaches a flat maximum at approximately 20 GeV/c. The decline towards higher momenta is caused by the detector resolution. According to the cross section eq. (6.1), high momentum incident positrons or electrons radiate bremsstrahlung photons with higher energy, resulting in higher momentum secondary particles which undergo a smaller deflection in the magnetic field of the AMS-01 tracker. Therefore, their trajectories are closer to each other and the decreasing cluster separation approaches the resolution limit of the silicon strip detectors. By contrast, at low momentum secondary particles may be deflected so that they generate multiple separated

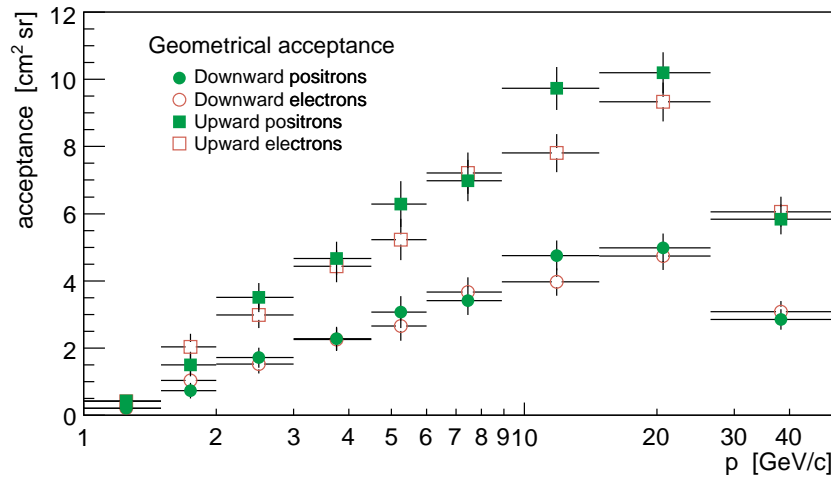


**Fig. 7.5:** The acceptance  $A(p)$  for downward and upward going positrons and electrons, when identified through bremsstrahlung conversion.

hits in single TOF planes. In this case an event is rejected by the level 3 trigger logic of the experiment. Furthermore, for secondary particles with too low momentum, the probability that they will not be properly reconstructed increases, leading to a decrease of the acceptance.

Additional material (the ATC, the Space Shuttle’s payload bay floor and the support structure of AMS-01) is traversed by upward going particles before they enter the detector (see § 5.1.6). Consequently, the acceptance for upward going particles is generally higher than for downward going ones. Except for the ATC, the amount of this additional material can only be estimated, since precise information is not available. Independent of their flight direction, no significant difference in the acceptance for electrons and positrons is observed.

## 7.2.2 Calculation of Livetime

For the calculation of the lifetime  $T$  as a function of momentum and of the direction of the incoming particles a method has been developed which is derived from the determination of the geomagnetic cutoff as described in sec. 6.4.4. The basic principle is to determine the cutoff rigidity in short time steps for the whole duration of the Space Shuttle flight and to count the livetime only for the momentum range above the cutoff.

In a first step, the acceptance region of AMS-01 is divided into nine bins of equal size in  $\cos \theta$  in the interval  $[0.7, 1]$  or  $[-1, -0.7]$  for downward or upward going particles, respectively, and into eight bins in  $\phi$ . Furthermore, the momentum range between 1 GeV/c and 50 GeV/c is divided into eight bins. Then, for every four seconds during the flight of the *Discovery*, her recorded position and attitude are obtained and for each of the 576  $(p, d\Omega)$ -bins, a virtual charged particle is started with the corresponding values inside the aperture of the detector and propagated backward through the geomagnetic field. If the virtual particle fulfills the criteria of a primary cosmic ray particle as described in

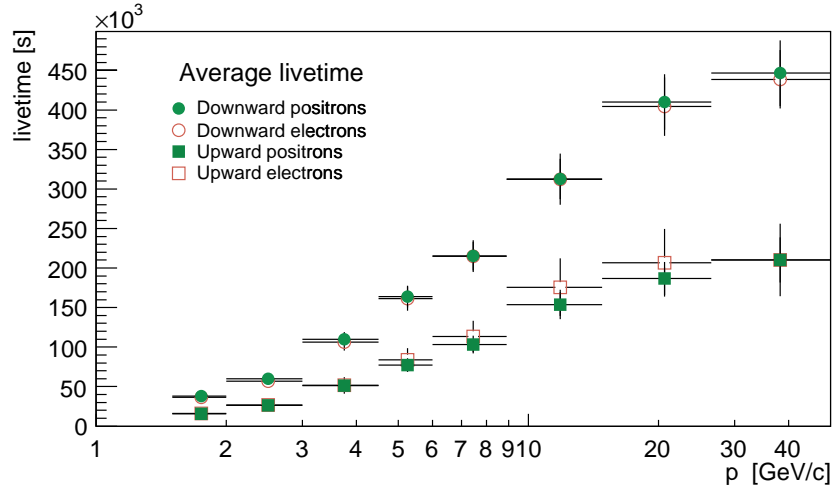


**Fig. 7.6:** The livetime, averaged over the detector acceptance, as a function of momentum for downward and upward going positrons and electrons.

section 6.4, the four-second time interval during which the particle has been detected is added to the total livetime of the corresponding momentum and acceptance bin after subtraction of the trigger dead time. This approach is as accurate as it is CPU-intensive, with a total of approximately 5000 GHz-CPU days spent for the calculations.

The livetime, averaged over the detector acceptance, is displayed in Figure 7.6 for downward and upward going positrons and electrons. As a consequence of the rigidity cutoff, it is a monotonically increasing function of momentum and converges to approximately 140 (55) hours for downward (upward) going particles. These values correspond to 75 % (30 %) of the total data taking time of about 184 hours. Since the Space Shuttle was mostly oriented towards the zenith (see section 5.3), and due to obstruction by the Earth's body, the livetime for downward going particles exceeds that of upward going ones. Concerning the average livetime, no significant difference between positively and negatively charged particles is apparent.

### 7.2.3 Positron and Electron Fluxes

Precise information about the thickness of the Space Shuttle's payload bay floor is not accessible. Hence, the amount of material underneath the detector, which strongly affects the acceptance for upward going particles, cannot be ascertained to a degree which is suitable for flux measurements, but only be estimated. As a consequence, in this analysis particle fluxes are calculated solely for downward going particles.

In Figure 7.7 the fluxes of downward going positrons and electrons, calculated according to eq. (7.3), together with results published earlier by AMS-01 [2], and HEAT- $e^\pm$  [3], are displayed together with their statistical errors. The fluxes are in very good agreement with previous measurements over the full momentum range, except for a slight discrepancy in the electron fluxes between 2 and 3 GeV. Here, at low momenta in combination with low statistics, additional inaccuracies of the backtracing through the geomagnetic field are

expected to become the dominant source of systematic error to the fluxes. However, this effect cancels out in the ratio giving the positron fraction.

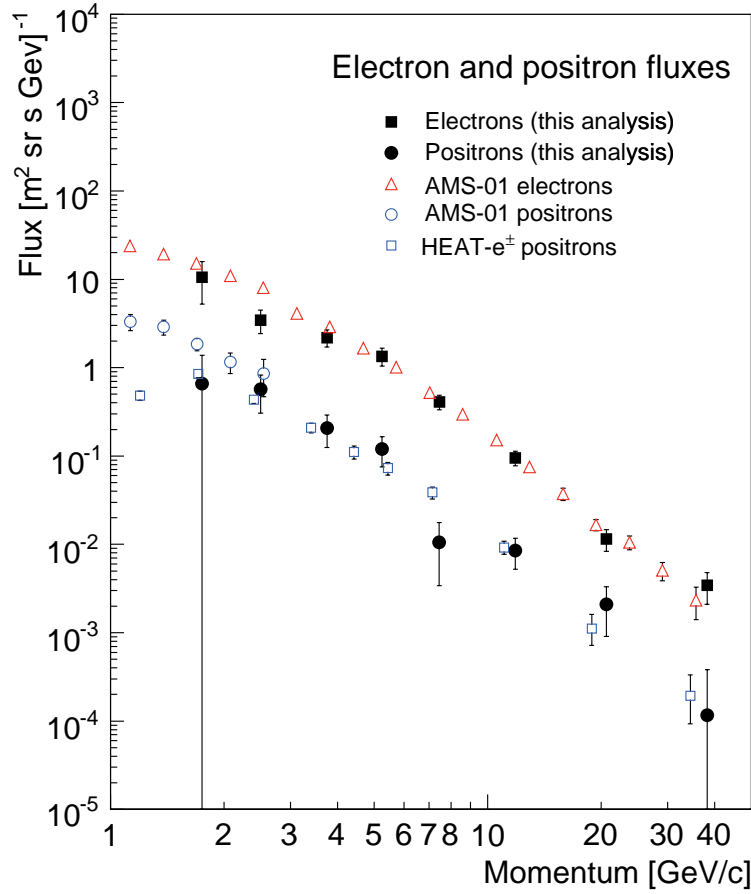


**Fig. 7.7:** The fluxes of downward going positrons and electrons measured in this analysis, compared with earlier results from AMS-01 [2] and HEAT-e<sup>±</sup> [3]. Error bars for results from this analysis denote statistical errors only.

## 8 Conclusions

Over the past decades it has become evident that luminous matter amounts only to a small fraction of the energy density in the universe. More than 75 % is accounted for by what is called the dark energy, and about 20 % must exist in the form of some kind of non-relativistic dark matter. At the same time new physics beyond the Standard Model of particle physics is expected to appear when present experimental limitations are exceeded. Among the many hypotheses anticipating these new phenomena, supersymmetry yields the most promising dark matter candidate, the neutralino. Thus cosmology, astrophysics and particle physics may simultaneously approach the same problem and their synergy could finally lead to a fundamentally new understanding of basic physics.

The general purpose detectors, CMS and ATLAS, at the LHC will be able to detect sparticles over large ranges of the supersymmetric parameters. Measurements of cosmic ray particles, especially of antiparticles such as positrons, can impose strong constraints on the nature of new physics beyond the Standard Model. However, cosmic ray positron measurements are experimentally very challenging due to the vast proton background. While new cosmic ray experiments are under construction or have recently started taking data, existing data from past experiments can be re-analyzed using new analysis techniques. This thesis describes a novel approach of positron identification applied to the data of the AMS-01 experiment, namely through the detection of bremsstrahlung conversion in a silicon microstrip detector. In contrast to earlier single-track analyses, this approach involves the selection and reconstruction of multi-track events. As the discussion of the signal process shows, bremsstrahlung from protons is suppressed by a factor of more than  $3 \cdot 10^6$  with respect to positrons due to the dependence of the cross section on the mass of the radiating particle. The background to the positron sample, which dominantly stems from protons undergoing hadronic interactions and from wrongly reconstructed electrons, can largely be suppressed using the topological and geometrical properties of the events.

In order to obtain the highest positron selection efficiency possible, novel combinatorial track finding algorithms were developed, particularly optimized for the signature of converted bremsstrahlung. These algorithms require no additional highly granular subdetector for the determination of track seeds and their momentum resolution is comparable to that of single-track events for momenta above 10 GeV. By applying restrictions on the invariant mass of particles the background to the positron sample can largely be eliminated. The remaining background contamination was determined from large samples of Monte Carlo data including the effects of the geomagnetic field. It amounted to 26 % of the positron counts and was corrected for. No indication was found for additional background produced in interactions with the Mir space station. Finally, in order to remove atmospheric secondaries from the positron and electron samples, the precise method of trajectory backtracing was applied individually to all positron and electron candidates.

The results of the positron measurement are presented in chapter seven. It is shown that the bremsstrahlung approach extends the sensitivity range of AMS-01 to positron

momenta up to 50 GeV/c, which is far beyond the original scope of the experiment. The precision of the positron fraction measurement is clearly statistically limited by the small number of particle counts. In the momentum range 1 to 8 GeV the fraction is in good agreement with model predictions for background from purely secondary positron production, while at higher momenta there is indication for a positron overabundance as already reported by other experiments [7]. However, the results of the present analysis are subject to different systematic errors, since they were obtained with a different detector and a new method of analysis. Furthermore, in contrast to the earlier balloon-borne experiments, AMS-01 was operated in space well above the Earth's atmosphere. Thus the AMS-01 data lend further weight to the hints of a positron overabundance seen in [7].

In addition to the positron fraction, the absolute fluxes of positrons and electrons were calculated from the event samples of this analysis. For this purpose, a method was developed which allows the determination of the livetime as a function of momentum and direction of incidence with high accuracy. The results of the flux calculation are found to be consistent with earlier data [2, 3]. In particular, the electron flux for momenta above 6 GeV is well in agreement with that obtained from measurements of single-track events in the AMS-01 data, confirming the good performance of particle selection with the bremsstrahlung approach.

The positron fraction results from this analysis have been combined with earlier results from AMS-01 [2], HEAT- $e^\pm$  and HEAT-pbar [7], CAPRICE [5] and TS93 [4] (see Figure 8.1). For this, a procedure for combining data with asymmetric errors was employed [173]. First, all data were grouped in 13 momentum bins. For each data point  $i$  the corresponding likelihood function  $\mathcal{L}_i$  was approximated by a Gaussian function with a variable standard deviation  $\sigma_i$ . The  $\mathcal{L}_i$  were parameterized using the values of the measurements and their upper and lower errors. The combined likelihood function  $\mathcal{L}$ , from which the combined results and errors are finally determined, is then defined by the product of the  $\mathcal{L}_i$  for a particular momentum bin. The central momentum value for each bin is given by the mean momenta of the data in the individual bins.

The combined positron fraction is shown in Figure 8.2 (*top*) and is compared to a model calculation for the background expected from purely secondary positron production (without diffuse reacceleration) [111]. Table 8.1 summarizes the results. The data indicate a positron overabundance for momenta above 6 GeV. The bottom display of Figure 8.2 shows the cumulative significance, i.e. the significance of all data for momenta  $p < p'$  with respect to the background-only prediction. The significance was calculated from the corresponding probability of the  $\chi^2$  per degree of freedom. Because of the possible effect of solar modulation on the positron fraction at low momenta, the data point below 0.3 GeV was not considered in the calculation. Apart from statistical fluctuations on the 2 standard deviation level, the positron fraction is in good agreement with purely secondary positron production for momenta below 6 GeV. However, when the data at higher momenta are considered, the significance of the positron overabundance increases to 5.3 standard deviations, which would be reduced to 4.2 standard deviations without the results of the present analysis. Therefore, a statistical fluctuation causing the positron overabundance in the data with respect to the background-only prediction can now be excluded.



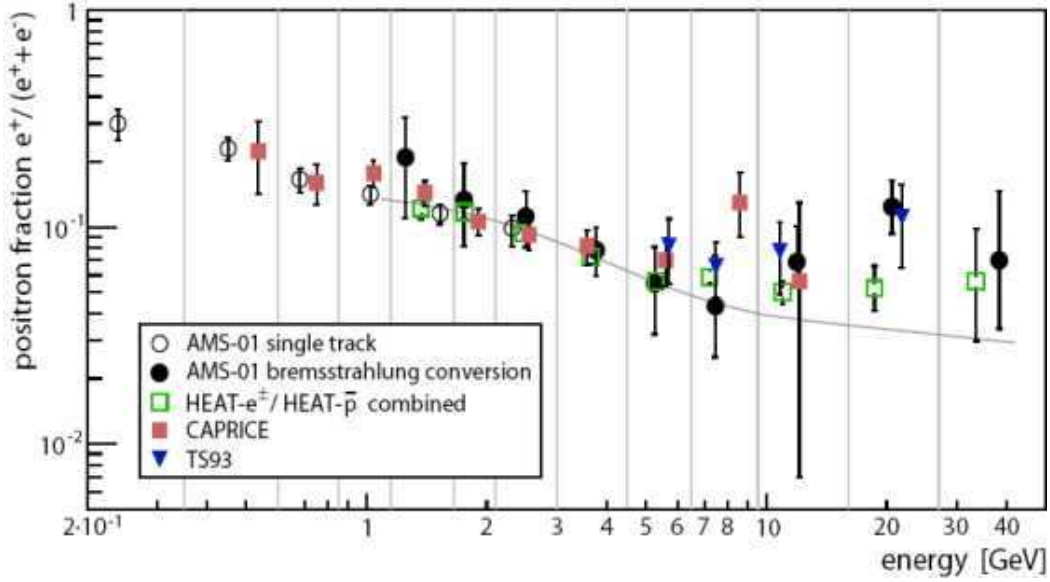


**Fig. 8.1:** The data used for the calculation of the combined positron fraction from: this analysis, AMS-01 (single tracks) [2], HEAT- $e^\pm$  and HEAT- $p$ -bar [7], CAPRICE [5] and TS93 [4]. The data were grouped within intervals which are denoted by vertical lines. The solid curve shows a model prediction for purely secondary positron production [111].

As stated in § 4.4, besides neutralino annihilation other possible contributions to the cosmic ray particle fluxes have been proposed, such as hypothetical Kaluza-Klein particle states or galactic pulsars. In order to establish through the analysis of cosmic ray spectra if annihilations of dark matter neutralinos are in fact responsible for the observed gamma and antiparticle overabundances and to narrow down the parameters of supersymmetry, more precise measurements remain necessary. Especially in the case of the cosmic ray positron fraction, measurements up to about 300 GeV will allow to precisely distinguish possible dark matter positron sources from other contributions.

In June 2006 the PAMELA satellite experiment [174], which is designed to study charged particles in cosmic rays with a particular focus on antiparticles, was launched for an at least three year long mission. PAMELA features, amongst other subdetectors, a silicon microstrip tracker in the 0.43 T field of a permanent magnet, a calorimeter and a neutron detector. However, with its small geometrical acceptance of  $21.5 \text{ cm}^2 \text{ sr}$ , it is unlikely that PAMELA will be able to deliver precise data at highest energies relevant to a possible dark matter signal. The successor to the AMS-01 experiment, AMS-02 [175], is currently under construction and scheduled for operation on the International Space Station (ISS) from 2009 on. Developed on the basis of the AMS-01 design, AMS-02 will feature strongly enhanced particle identification by means of a calorimeter, a ring imaging Čerenkov detector and a transmission radiation detector (TRD), as well as an improved silicon microstrip tracker in the 0.87 T field of a superconducting magnet. With a geometrical acceptance of the tracking system of  $4500 \text{ cm}^2 \text{ sr}$  and  $900 \text{ cm}^2 \text{ sr}$  for the tracker in combination with the TRD and the calorimeter, exceeding that of PAMELA by a factor

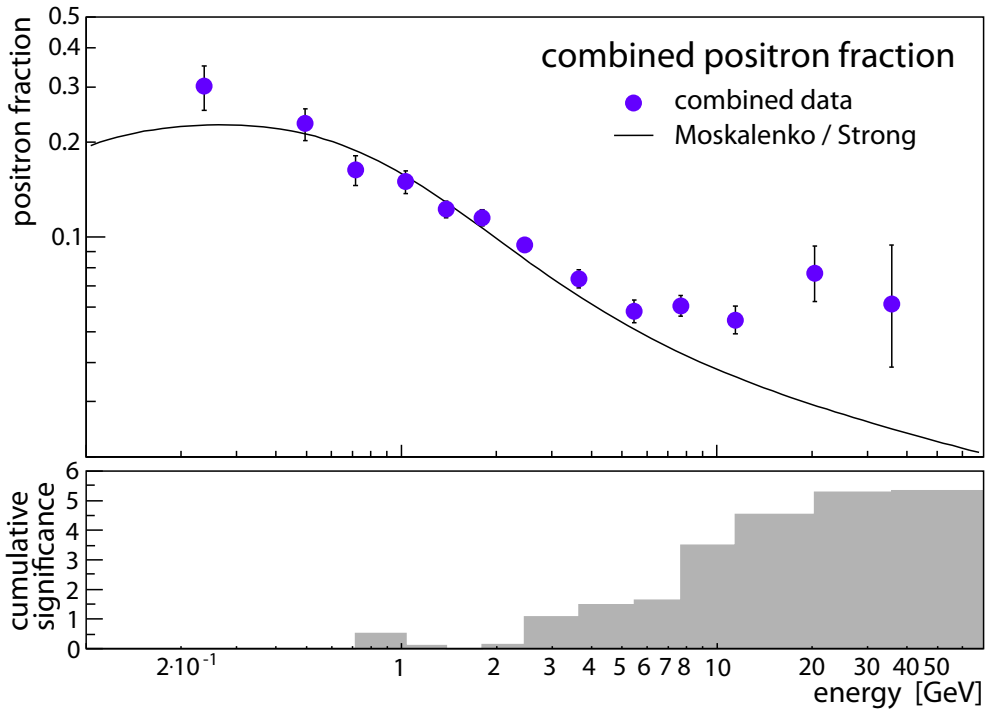


**Fig. 8.2:** The combined positron fraction of the results from this analysis and earlier results. The solid curve shows a model prediction for purely secondary positron production [111] (*top*); the cumulative significance (the significance of all data for momenta  $p < p'$ ) of the positron overabundance in the data with respect to the background-only prediction. The data point below 0.3 GeV was not considered in the calculation (*bottom*).

of more than 40, AMS-02 will conduct cosmic ray spectroscopy with unprecedentedly high precision.

$E$ [GeV]	$\bar{E}$ [GeV]	$e^+$ fraction data					Combined $e^+$ fraction	$\chi^2 / n_{\text{dof}}$ of average
		This work	AMS-01	HEAT	CAPRICE	TS93		
0.20 – 0.35	0.24	—	$0.300^{+0.048}_{-0.049}$	—	—	—	$0.300^{+0.048}_{-0.049}$	— / 1
0.35 – 0.60	0.50	—	$0.230^{+0.028}_{-0.029}$	—	$0.220^{+0.081}_{-0.081}$	—	$0.230^{+0.026}_{-0.027}$	0.01 / 2
0.60 – 0.85	0.71	—	$0.170^{+0.02}_{-0.021}$	—	$0.160^{+0.034}_{-0.034}$	—	$0.160^{+0.017}_{-0.018}$	0.02 / 2
0.85 – 1.10	1.00	—	$0.140^{+0.015}_{-0.015}$	—	$0.180^{+0.025}_{-0.025}$	—	$0.150^{+0.012}_{-0.013}$	1.50 / 2
1.10 – 1.60	1.40	$0.210^{+0.11}_{-0.1}$	$0.120^{+0.01}_{-0.013}$	$0.120^{+0.016}_{-0.014}$	$0.140^{+0.019}_{-0.019}$	—	$0.120^{+0.0071}_{-0.0076}$	2.40 / 4
1.60 – 2.10	1.80	$0.130^{+0.064}_{-0.051}$	—	$0.120^{+0.0077}_{-0.0076}$	$0.110^{+0.015}_{-0.015}$	—	$0.120^{+0.0067}_{-0.0067}$	0.55 / 3
2.10 – 3.00	2.50	$0.110^{+0.034}_{-0.031}$	$0.099^{+0.015}_{-0.017}$	$0.094^{+0.0054}_{-0.0043}$	$0.092^{+0.014}_{-0.014}$	—	$0.094^{+0.0049}_{-0.0041}$	0.41 / 4
3.00 – 4.50	3.60	$0.078^{+0.021}_{-0.019}$	—	$0.072^{+0.0054}_{-0.0049}$	$0.082^{+0.015}_{-0.015}$	—	$0.074^{+0.005}_{-0.0047}$	0.43 / 3
4.50 – 6.50	5.50	$0.055^{+0.026}_{-0.023}$	—	$0.056^{+0.0052}_{-0.0048}$	$0.070^{+0.019}_{-0.017}$	$0.082^{+0.027}_{-0.027}$	$0.058^{+0.0049}_{-0.0046}$	1.40 / 4
6.50 – 9.50	7.70	$0.043^{+0.031}_{-0.018}$	—	$0.059^{+0.0049}_{-0.0044}$	$0.130^{+0.049}_{-0.039}$	$0.066^{+0.019}_{-0.019}$	$0.060^{+0.0049}_{-0.0044}$	4.30 / 4
9.50 – 16.00	11.00	$0.069^{+0.032}_{-0.015}$	—	$0.050^{+0.0065}_{-0.0057}$	$0.056^{+0.073}_{-0.049}$	$0.077^{+0.028}_{-0.028}$	$0.054^{+0.0059}_{-0.0052}$	2.00 / 4
16.00 – 27.00	20.00	$0.120^{+0.04}_{-0.031}$	—	$0.052^{+0.014}_{-0.011}$	—	$0.110^{+0.046}_{-0.046}$	$0.077^{+0.017}_{-0.014}$	5.80 / 3
27.00 – 50.00	36.00	$0.070^{+0.076}_{-0.036}$	—	$0.056^{+0.04}_{-0.026}$	—	—	$0.061^{+0.033}_{-0.022}$	0.06 / 2

**Tab. 8.1:** The combined positron fraction and the data used for its calculation from: this work, AMS-01 (single tracks) [2], HEAT- $e^\pm$  and HEAT-pbar [7], CAPRICE [5] and TS93 [4]. Also given is the average energy  $\bar{E}$  of the measurements and the energy interval  $E$  that was used in grouping them. The last column gives the  $\chi^2$  and the number of degrees of freedom  $n_{\text{dof}}$  of the combined values.



# Acknowledgment

First, I want to thank my supervisor Prof. St. Schael for the opportunity to work on this fascinating subject and his advice, encouragement and thoroughgoing support I could always count on. I also want to thank Prof. L. Baudis for her help and expert opinion.

The positron analysis would not have been successful without the collaboration of H. Gast who contributed very much valuable work and countless excellent ideas for solving the many problems we were encountering. It was really a marvelous and fruitful team work. Besides, many other of my colleagues from the I. Physikalisches Institut B have a part in the success of my work through their help, advice, and the discussions I had with them: R. Adolphi, C. Berger, W. Braunschweig, C. H. Chung, L. Feld, S. König, K. Lübelmeyer, A. Ostapchouk, D. Pandoulas, A. Schultz v. Dratzig, G. Schwering, T. Siedenbueg, W. Wallraff and B. Wittmer, only to name a few. Furthermore, I enjoyed working with the members of the ARC group of the III. Physikalisches Institut B, namely M. Axer, F. Beißel, T. Franke, T. Hermanns, S. Kassermann, J. Mnich, J. Niehusman and M. Pöttgens. Thank you for the excellent and straightforward collaboration.

I benefited much from the aid and knowledge of many kind individuals of the AMS and CMS collaborations, such as from J. Alcaraz, W. Beaumont, H. Breuker, M. Buénerd, M. Capell, C. Goy-Henningsen, F. Hartmann, G. Kim, J. Shin, H.-J. Simonis, V. Zhukov and P. Zucco. Very special thanks go to V. Choutko for his encouragement and vital help and advice in many aspects of the positron analysis.

The smooth and powerful performance of the computing services of AMS and especially here in Aachen were crucial for this work. I would like to thank all the individuals who kept the machines running, and in particular A. Eline, A. Klimentov, T. Kreß and C. Kukulies for their kind support and advice. Many thanks to the staff of the mechanical and electronics workshops in Aachen, particularly to W. Karpinski, G. Kirchhoff, R. Siedling<sup>†</sup> and M. Wlochal for their help and guidance in the technical aspects of my work.

R. Adolphi, H. Gast, K. Klein and especially D. Pandoulas have read the manuscript of this thesis very carefully, and I owe them many substantial improvements. Thank you very much for this.

One good reason for spending more time at work rather than at home is sharing the office with R. Adolphi, G. Anagnostou, H. Gast, K. Klein and A. Ostapchouk. Thank you my colleagues and friends for the great time we had during the past few years, and of course for all those legendary *Büroabende*. Besides the abovementioned, a lot of people from the Aachen physics institutes were responsible for the amicable and comfortable atmosphere at work, such as R. Brauer, T. Bruch, P. v. Doetinchem, M. Fernandez Garcia, A. Fischer, S. Fopp, S. Funk, T. Krynicki, J. Hattenbach, A. Heister, T. Hennig, S. Hermann, T. Kirn, M. Kosbow, J. Orboeck, F. Raupach, G. Roper, M. Thomas, M. Weber, M. Zöller, and many more.

Finally, I want to thank my family for making all this possible.





# Bibliography

- [1] R. Beckwith et al., *Astron. J.* **132** (2006) 1729
- [2] J. Alcaraz et al., *Phys. Lett. B* **484** (2000) 10
- [3] M. A. DuVernois et al., *ApJ* **559** (2001) 296
- [4] R. L. Golden et al., *ApJ* **457** (1996) L103
- [5] M. Boezio et al., *ApJ* **532** (2000) 653
- [6] J. Alcaraz et al., *Phys. Lett. B* **472** (2000) 215
- [7] J. J. Beatty et al., *Phys. Rev. Lett.* **93** (2004) 241102
- [8] A. Friedman, *Z. Phys.* **10** (1922) 377
- [9] E. Hubble, *Proc. Nat. Acad.* **15** (1929) 168
- [10] G. Gamow, *Phys. Rev.* **70** (1946) 572
- [11] G. Gamow, *Phys. Rev.* **74** (1948) 505
- [12] A. A. Penzias, R. W. Wilson, *ApJ* **142** (1965) 419
- [13] R. A. Alpher, R. C. Herman, *Phys. Rev.* **75** (1949) 1089
- [14] D. N. Spergel et al., *ApJS* **148** (2003) 175
- [15] V. de Lapparent, M. J. Geller, J. P. Huchra, *ApJ* **302** (1986) L1
- [16] J. L. Tonry et al., *ApJ* **594** (2003) 1
- [17] D. N. Spergel et al., submitted article, [astro-ph/0603449](#) (2006)
- [18] J. R. Gott et al., *ApJ* **624** (2005) 463
- [19] A. H. Guth, D. I. Kaiser, *Science* **307** (2005) 884
- [20] M. S. Turner, J. A. Tyson, *Rev. Mod. Phys.* **71** (1999) S145
- [21] A. D. Sakharov, *J. Exp. Theor. Phys. Lett.* **5** (1967) 24
- [22] J. A. Tyson, G. P. Kochanski, I. P. Dell’Antonio, *ApJ* **498** (1998) L107
- [23] K. G. Begeman, A. H. Broeils, R. H. Sanders,  
*Mon. Not. R. Astron. Soc.* **249** (1991) 523
- [24] F. Zwicky, *Helv. Phys. Acta* **6** (1933) 110
- [25] G. Bertone, D. Hooper, J. Silk, *Phys. Rep.* **405** (2004) 279
- [26] R. G. Carlberg et al., *ApJ* **516** (1998) 552
- [27] Y. Sofue, V. Rubin, *Annu. Rev. Astron. Astrophys.* **39** (2001) 137
- [28] G. Hinshaw et al., submitted article, [astro-ph/0603451](#) (2006)
- [29] W. Hu, *Ann. Phys.* **303** (2003) 203
- [30] S. Cole et al., *Mon. Not. R. Astr. Soc.* **362** (2005) 505
- [31] M. Tegmark et al., *ApJ* **606** (2004) 702
- [32] W.-M. Yao et al., *J. Phys. G* **33** (2006) 1, and references therein
- [33] P. W. Higgs, *Phys. Lett.* **12** (1964) 132;  
P. W. Higgs, *Phys. Rev.* **145** (1966) 1156

- [34] N. Cabibbo, Phys. Rev. Lett. **10** (1963) 531
- [35] M. Kobayashi, T. Maskawa, Prog. Theor. Phys. **49** (1973) 652
- [36] J. Overduin, P. Wesson, Phys. Rep. **402** (2004) 267
- [37] B. Paczynski, ApJ **304** (1986) 1
- [38] S. Martin, hep-ph/9709356 (1997)
- [39] U. Amaldi, W. de Boer, H. Fürstenau, Phys. Lett. B **260** (1991) 447
- [40] D. Chung et al., Phys. Rep. **407** (2005) 1
- [41] C. H. Chung, PhD thesis in preparation, RWTH Aachen (2007)
- [42] D. Hooper, J. Silk, Phys. Rev. D **71** (2005) 083503
- [43] G. Jungman, M. Kamionkowski, K. Griest, Phys. Rep. **267** (1996) 195
- [44] H. Baer et al., J. Cosmol. Astropart. Phys. **08** (2004) 005
- [45] R. J. Gaitskell, Annu. Rev. Nucl. Part. Sci. **54** (2004) 315
- [46] M. Aguilar et al., Phys. Rep. **366** (2002) 331
- [47] W. de Boer et al., Phys. Lett. B **636** (2006) 13
- [48] O. Brüning et al. (ed.), CERN Yellow Report 2004-003-V-1 (2004)
- [49] O. Brüning et al. (ed.), CERN Yellow Report 2004-003-V-2 (2004)
- [50] M. Benedikt et al. (ed.), CERN Yellow Report 2004-003-V-3 (2004)
- [51] D. Brandt et al., Rep. Prog. Phys. **63** (2000) 939
- [52] The ALEPH Collaboration et al., Phys. Rep. **427** (2006) 257
- [53] M. Lamont et al., CERN LHC Project Report **949** (2006)
- [54] M. Lamont, CERN LHC Project Note **375** (2005)
- [55] The ATLAS Collaboration, CERN-LHCC-99-014, CERN-LHCC 99-015 (1999)
- [56] M. Della Negra et al., CERN-LHCC-2006-001 (2006)
- [57] M. Della Negra et al., CERN-LHCC-2006-021 (2006)
- [58] The LHCb Collaboration, CERN-LHCC-98-004 (1998)
- [59] R. Antunes-Nobrega et al., CERN-LHCC-2003-030 (2003)
- [60] The ALICE Collaboration, CERN-LHCC-95-071 (1995)
- [61] S. Abdullin et al., J. Phys. G **28** (2002) 469
- [62] A. V. Gladyshev, D. I. Kazakov, hep-ph/0606288 (2006)
- [63] I. Hinchliffe et al., Phys. Rev. D **55** (1997) 5520
- [64] R. Kitano, Y. Nomura, Phys. Rev. D **73** (2006) 095004
- [65] D. Denegri, Nuovo Cim. B **120** (2005) 687
- [66] The CMS Collaboration, CERN-LHCC-94-38 (1994)
- [67] The CMS Collaboration, CERN-LHCC-97-10 (1997)
- [68] The CMS Collaboration, CERN-LHCC-97-32 (1997)
- [69] The CMS Collaboration, CERN-LHCC-97-33 (1997)
- [70] The CMS Collaboration, CERN-LHCC-97-31 (1997)
- [71] The CMS Collaboration, CERN-LHCC-98-6 (1998)
- [72] R. Brauer et al., CERN CMS Note 2005/025 (2005)

- [73] The CMS Collaboration, CERN-LHCC-2000-016 (2000)
- [74] S. Cucciarelli, Nucl. Inst. Meth. A **549** (2005) 49
- [75] T. Franke, PhD Thesis, RWTH Aachen (2005)
- [76] M. J. French et al., Nucl. Inst. Meth. A **466** (2001) 359
- [77] M. Axer, PhD Thesis, RWTH Aachen (2003)
- [78] S. Braibant et al., Nucl. Inst. Meth. A **485** (2002) 343
- [79] F. Scholze et al., Nucl. Inst. Meth. A **439** (2000) 208
- [80] I. Abt et al., Nucl. Inst. Meth. A **423** (1999) 303
- [81] A. Dierlamm, Nucl. Inst. Meth. A **514** (2003) 167
- [82] M. Meschini et al., CMS Internal Note 2004/018 (2004)
- [83] M. Axer et al., Nucl. Inst. Meth. A **485** (2002) 73
- [84] B. Wittmer, PhD Thesis, RWTH Aachen (2002)
- [85] M. Axer et al., Nucl. Inst. Meth. A **518** (2004) 321, and references therein
- [86] V. Hess, Phys. Zeit. **13** (1912) 1084
- [87] C. D. Anderson, Phys. Rev. **43** (1933) 491
- [88] S. H. Neddermeyer, C. D. Anderson, Phys. Rev. **51** (1937) 884
- [89] C. M. G. Lattes et al., Nature **159** (1947) 694;  
C. M. G. Lattes, G. P. S. Occhialini, C. F. Powell, Nature **160** (1947) 453;
- [90] G. D. Rochester, C. C. Butler, Nature **160** (1947) 855
- [91] J. Cronin, T. K. Gaisser, S. P. Swordy, Sci. Amer. **v276** (1997) 44
- [92] J. Alcaraz et al., Phys. Lett. B **490** (2000) 27
- [93] J. Alcaraz et al., Phys. Lett. B **494** (2000) 193
- [94] D. J. Bird et al., ApJ **424** (1994) 491
- [95] J. Cronin, Rev. Mod. Phys. **71** (1999) S165
- [96] J. Alcaraz et al., Phys. Lett. B **461** (1999) 387
- [97] S. Orito et al., Phys. Rev. Lett. **84** (2000) 1078
- [98] J. A. Lezniak, W. R. Webber, ApJ **223** (1978) 676
- [99] E. Fermi, Phys. Rev. **75** (1949) 1169
- [100] T. K. Gaisser, Cosmic Rays and Particle Physics, Camb. Univ. Press (1990)
- [101] R. D. Blandford, J. P. Ostriker, ApJ **221** (1978) L29
- [102] G. Gloeckler, Adv. Space Res. **4** (2–3) (1984) 127
- [103] J. Steinacker, R. Schlickeiser, Astron. Astrophys. **224** (1989) 259
- [104] R. D. Blandford, D. Eichler, Phys. Rep. **154** (1987) 1
- [105] Y. Uchiyama, T. Takahashi, F. Aharonian, Publ. Astron. Soc. Jap. **54** (2002) L73
- [106] F. Aharonian et al., Nature **432** (2004) 75
- [107] I. Moskalenko, Frascati Phys. Ser. **35** (2004) 115
- [108] S. Stephens, R. Streitmatter, ApJ **505** (1998) 266
- [109] D. Maurin et al., ApJ **555** (2001) 585
- [110] J. P. Vallée, ApJ **437** (1994) 179
- [111] I. V. Moskalenko, A. W. Strong, ApJ **493** (1998) 694

- [112] I. Moskalenko, A. Strong, O. Reimer, *Astron. Astrophys.* **338** (1998) L75
- [113] R. Murphy, C. Dermer, R. Ramaty, *ApJS* **63** (1987) 721
- [114] L. Gleeson, W. Axford, *ApJ* **154** (1968) 1011
- [115] J. M. Clem et al., *ApJ* **464** (1996) 507
- [116] I. Usoskin et al., *J. Geophys. Res.* **110** (2005) A12108
- [117] N. Olsen et al., *Geophys. Res. Lett.* **27** (2000) 3607
- [118] C. Russell, *Ann. Rev. Earth Planet Sci.* **19** (1991) 169
- [119] X. Li, M. Temerin, *Space Sci. Rev* **95** (2001) 569
- [120] D. Smart, M. Shea, E. Flückiger, *Proc. 26<sup>th</sup> ICRC* **7** (1999) 337
- [121] G. Kane, L. Wang, T. Wang, *Phys. Lett. B* **536** (2002) 263
- [122] W. de Boer et al., *Astron. Astrophys.* **444** (2005) 51
- [123] S. Coutu et al., *Proc 27<sup>th</sup> ICRC* (2001) 1687
- [124] W. de Boer et al., *Eur. Phys. J. C* **33** (2004) S981
- [125] L. Bergström et al., *J. Cosmol. Astropart. Phys.* **05** (2006) 006
- [126] L. Zhang, K. S. Cheng, *Astron. Astrophys.* **368** (2001) 1063
- [127] NASA – National Aeronautics and Space Administration,  
NASA/TP–1999–209260 (1999)
- [128] H. Suter, AMS Internal Note 98/29 (1998)
- [129] D. Alvisi et al., *Nucl. Inst. Meth. A* **437** (1999) 212
- [130] L. Baldini et al., *Proc. 27<sup>th</sup> ICRC* (2001) 2211
- [131] J. Alcaraz et al., *Nuovo Cim. A* **112** (1999) 1325
- [132] W. J. Burger, *Nucl. Inst. Meth. A* **435** (1999) 202
- [133] V. M. Ghete, *UBPub. EPPG/Phys.* **33** (1996)
- [134] B. Alpat et al., *Nucl. Inst. Meth. A* **439** (2000) 53, and references therein
- [135] M. Ionica, *Nucl. Inst. Meth. A* **513** (2003) 222
- [136] G. Lamanna, PhD Thesis, University of Perugia (2000)
- [137] J. Vandenhirtz, W. Wallraff, M. Weisgerber, *Proc 27<sup>th</sup> ICRC* (2001) 2197
- [138] W. J. Burger et al., *Nucl. Inst. Meth. A* **512** (2003) 517
- [139] D. Barancourt et al., *Nucl. Inst. Meth. A* **465** (2001) 306
- [140] K. Luebelsmeyer, private communication
- [141] R. Henning, PhD Thesis, Massachusetts Institute of Technology (2003)
- [142] NASA – National Aeronautics and Space Administration (2004)  
<http://spaceflight.nasa.gov/shuttle/reference>
- [143] D. Casadei, AMS Bologna Internal Note 2000-03-02, updated (2002)
- [144] V. Choutko, AMS Internal Note 97/95a.
- [145] M. Aguilar et al., *Nucl. Inst. Meth. B* **234** (2005) 321
- [146] H. Suter, AMS Internal Note 2000-07-03 (2000)
- [147] NASA – National Aeronautics and Space Administration (1999)  
<http://spaceflight.nasa.gov/history/shuttle-mir>
- [148] L. Schiff, *Phys. Rev.* **83** (1951) 252

- [149] Y. Tsai, Rev. Mod. Phys. **46** (1974) 815, Rev. Mod. Phys. **49** (1977) 421
- [150] M. Stearns, Phys. Rev. **76** (1949) 836
- [151] P. Capiluppi et al., Nucl. Phys. B **70** (1974) 1
- [152] Y. Nara et al., Phys. Rev. C **61** (1999) 024901, and references therein
- [153] A. S. Carroll et al., Phys. Lett. B **80** (1979) 319
- [154] G. D. Badhwar, S. A. Stephens, R. L. Golden, Phys. Rev. D **15** (1977) 820
- [155] B. Rossi, High-Energy Particles. Prentice-Hall (1965)
- [156] N. A. McCubbin, Rep. Prog. Phys. **44** (1981) 1027
- [157] V. Choutko, Unpublished AMS Note (2003)  
[http://ams.cern.ch/AMS/Analysis/hpl3itp1/ams\\_rec\\_sel.ps](http://ams.cern.ch/AMS/Analysis/hpl3itp1/ams_rec_sel.ps)
- [158] J. C. Hart, D. H. Saxon, Nucl. Inst. Meth. **220** (1984) 309
- [159] V. Choutko, Unpublished AMS Technical Note (1996)  
<http://ams.cern.ch/AMS/Analysis/hpl3itp1/amsnote.ps>
- [160] F. James, M. Roos, Comput. Phys. Commun. **10** (1975) 343
- [161] H. Gast, Diploma Thesis, RWTH Aachen (2004)
- [162] R. Brun et al., CERN DD/EE/84-1 (1987)
- [163] Y.-H. Chang, Nucl. Inst. Meth. A **466** (2001) 282
- [164] U. Fano, Annu. Rev. Nucl. Sci. **13** (1963) 1
- [165] H. Bichsel, Rev. Mod. Phys. **60** (1988) 663
- [166] E. Flückiger, E. Kobel, J. Geomag. Geoelectr. **42** (1990) 1123
- [167] N. A. Tsyganenko, Planet. Space Sci. **37** (1989) 5
- [168] IAGA – International Association of Geomagnetism and Aeronomy (2006)  
<http://www.ngdc.noaa.gov/IAGA/vmod>
- [169] O. Helene, Nucl. Inst. Meth. **212** (1983) 319
- [170] O. Helene, Nucl. Inst. Meth. A **228** (1984) 120
- [171] T. Johnson, Phys. Rev. **45** (1934) 569
- [172] J. D. Sullivan, Nucl. Inst. Meth. **95** (1971) 5
- [173] R. Barlow, physics/0603449 (2004)
- [174] P. Picozza et al., submitted article, astro-ph/0608697 (2006)
- [175] C. Lechanoine-Leluc, Proc 29<sup>th</sup> ICRC **3** (2005) 381